2007

Micro coaxial transmission lines for integrated microwave circuits

Saravana Prakash Natarajan
University of South Florida

Scholar Commons Citation

Natarajan, Saravana Prakash, "Micro coaxial transmission lines for integrated microwave circuits" (2007). *USF Tampa Graduate Theses and Dissertations.*
https://digitalcommons.usf.edu/etd/2298

Micro Coaxial Transmission Lines for Integrated Microwave Circuits

by

Saravana Prakash Natarajan

A dissertation submitted in partial fulfillment
of the requirements for the degree of
Doctor of Philosophy
Department of Electrical Engineering
College of Engineering
University of South Florida

Major Professor: Thomas M. Weller, Ph.D.
Lawrence P. Dunleavy,Ph.D.
Andrew M. Hoff, Ph.D.
Hariharan Srikanth, Ph.D.
Venkat Bhethanabotla, Ph.D.

Date of Approval:
November 1, 2007

Keywords: shielded line, 3-D transmission line, micro coax, air core line, vertical integration

Dedicated to my parents and sister for their unconditional love and support

Table of Contents

List of Tables

List of Figures

Micro Coaxial Transmission Lines for Integrated Microwave Circuits

Saravana Prakash Natarajan

ABSTRACT

The research presented in this doctoral dissertation introduces a developmental path to realize micro coaxial transmission lines for wafer-level microwave and millimeter wave circuits. The micro coax lines conceptualized in this research are three-dimensional, with a uniquely low vertical profile of 20 µm. They are distinguishable from other transmission line topologies due to frequency limitless, cross-talk free performance in high density circuits resulting from the totally shielded construction. Design and optimization was done using equations and electromagnetic simulations. Extensive process development has been carried out to fabricate these devices on CMOS grade silicon wafers using processes amenable to the IC manufacturing industry. Micro coax lines of three different core types including air, semi-dielectric and all-dielectric cores were designed, fabricated and analyzed from 1 - 40 GHz with respect to line impedance and the volume of polyimide (dielectric) in the micro coax cavity. The insertion loss of the lines was found to vary from 2 to 9 dB/cm depending on the width the center conductor, total cross-sectional area and core type.

The versatility of the micro coax technology developed in the earlier part of this research has been successfully integrated with RF MEMS to embed a MEM varactor inside the micro coax cavity capable of achieving a capacitance ratio around 7 with an actuation voltage of 40 - 60V. The vertical integration capability of the micro coax was demonstrated by locating a millimeter wave slot antenna on the top side shield of a rectangular micro coax line, also acting as the electromagnetically coupled feed for the antenna. The antenna was designed to operate in the full range of the unlicensed 57 - 64 GHz spectrum capable of Gbps data rates. A 15 dB bandwidth of 17% and a hemispherical radiation pattern was achieved. Lastly, a diversified application

involving the application of an integrated micro coax probe-microfluidic chamber approach to detect bacteria through impedance measurements has been introduced.

In summary, the development and implementation of micro coax technology on a large scale is bound to create a paradigm shift in the development of high density microwave and millimeter wave circuits for RF MEMS and integrated antennas.

Preface

I would like to thank my major professor, Dr. Thomas M. Weller for giving me a chance to work with him for a Masters and continue on for a Doctorate degree. The confidence he had in me and his words of encouragement in times of crisis kept me going through the years. I have learnt a lot from him both professionally and personally, which has made me a better person in almost everything that I do. The freedom he gave me to think and try out things in the lab, the patience and trust he had in me has brought me to where I am now.

Dr. Larry Dunleavy deserves special thanks for being my dissertation committee and providing the research group with world-class microwave measurement facilities. I can never forget the brainstorming sessions with Dr. Andrew Hoff about developing viable process flows for use in this fabrication intensive research. Thank you, Dr. Hariharan Srikanth and Dr. Venkat Bhethanabotla for serving on my dissertation committee and thoughtful suggestions to improve the manuscript. Special thanks to Dr. Srinivas Katkoori for chairing my dissertation defense.

None of the fabrication in my dissertation would have been possible without the round-the-clock help and support of Robert Tufts and Rich Everly at the Nanomaterials and Nanomanufacturing Research Center. I am also grateful to Dr. Jim Culver for showing me the ropes of microfabrication. The assistance of Dr. Thomas Ketterl in PECVD nitride deposition at the STAR center is greatly appreciated. I would like to acknowledge and thank Doug Heden at HD Microsystems for the polyimide, related chemical samples and all the technical insights. I would also like to thank Dr. Bhansali and members of his group, Shyam, Subbu, Puneet and Praveen for their assistance and shared resources in our fabrication laboratory. Special thanks to Andy Mackley at the Center for Biological Defense, USF for bacteria samples and educating me on the basic aspects of impedance based biological sensing. I would like to express my regards and respect to my good friend and ‘guru’ of microwaves Balaji, who taught me a lot of the concepts that I know and for flying down all the way from San Diego to attend my dissertation presentation and support me. He has been a constant source of motivation ever since my first day at USF. I am grateful to Alberto for teaching me the nuances of microwave measurements. Thanks to Henrry for guiding me through the slot antenna project and assistance with measurements. I wish I could be an ‘angel’ like him. Thanks to my dear friend Suzette for keeping me company and extending my workday well beyond my limits with her friendly force. Bojana, I can never forget, “Oh...look who I found here...” Thank you for your sense of humor and friendship. Sergio, man I love to see you in your spot, right across from me, trying to make me laugh. I wish I could be as cool as you. A big thank you to all the other present and past members of ENB 412 who made me look forward to go back to work everyday and making me feel like, I am in my second home. I am sure I would cherish all the fun, the discussions and arguments we have had over the years. Thank you for everything Aswin, one day I hope to start my own ‘SP circuits’ with the motivation you have given me. Our friend SK will always be by guru for “several” things in life.

All my present, past roommates and close friends have had a great role to play toward the successful completion my degree. I consider all my roommates - Ananth, Sriram, Shyam, Srinath, Venkatesh and Madhan and Sivakumar as my extended family. We have bonded so much over the years that I cannot imagine going back to a home without them. My virtual roommate, Karthik Sriram has created quite an impact on my life in Tampa over the last couple years. Supriya, my colleague and good friend from the fabrication laboratory is an interesting character who never ceases to amaze me. Special mention goes to my dear friend, Sangeetha who is a never ending source of energy and always showered boundless affection on me and truly liked me for what I am. Thank you to my long time friend Ganesh, for being a role model and showing me the importance of tolerance, patience, sincerity and principles in every aspect of life. Sathya, my good friend and office-mate will always be fresh in my mind for the hours of chats and discussions we have had on countless topics. I am grateful to my long time friend Lavi for her support and her parents who treat me like a family member. Thanks to my friends Lalitha and Siva and Subbu for everything.

I would like to conclude by saying that, I am indebted to my mother, father and sister for life for their love, affection and support. If not for them, I would not be what I am today.

Chapter 1

Introduction

1.1 Overview

The most fundamental building block for any microwave circuit is the transmission line. Coaxial lines have been used to transmit telephone and television signals from the early 1900s. The first coaxial transmission line was introduced by Oliver Heaviside in 1880, followed by the demonstration of a waveguide type transmission line in 1894. Ever since, coaxial lines have been undergoing changes. The first commercially viable modern coaxial line design was unveiled in 1929 by AT&T Bell Labs. Coaxial lines found widespread use to carry various types of wireless signals due to their shielded structure, good performance and simple construction. The fact that the cross-sectional area of the coaxial cable could be tailored according to the application and their physical flexibility made them ubiquitous in RF circuits and systems. A coaxial cable is constructed by surrounding a metallic conductor with a dielectric material, which in turn is covered by a metallic outer shielding as shown in Figure 1. This results in a relatively cheap, fully shielded transmitting structure that is capable of carrying medium power microwave and millimeter-wave signals with relatively low line losses.

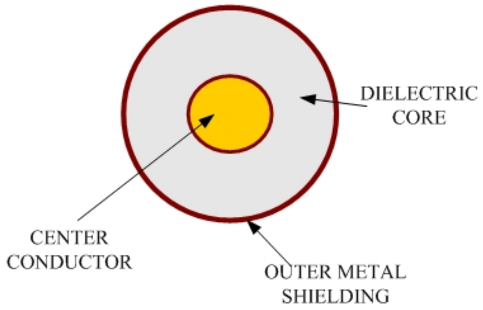

Figure 1.1 Cross-section of a Coaxial Cable

The evolution of technology, shrinking of devices and integrated circuits necessitated the need for more compact and planar transmission lines such as microstrip, stripline and coplanar waveguides. High density on-wafer integration and miniaturization of microwave circuits has been made possible using such planar transmission lines. The choice of transmission line depends on parameters such as substrate, application, frequency range, size, and cost to name a few. The following table reproduced from Pozar [1] compares the characteristics of some common transmission lines.

Table 1.1 Comparison of Common Transmission Lines and Waveguides

Characteristic	Coax	Waveguide	Stripline	Microstrip
Modes: Preferred Other	TEM TM, TE	TE_{10} TM, TE	TEM TM, TE	Quasi-TEM Hybrid TM, TE
Dispersion	None	Medium	None	Low
Bandwidth	High	Low	High	High
Loss	Medium	Low	High	High
Power Capacity	Medium	High	Low	Low
Physical Size	Large	Large	Medium	Small
Ease of Fabrication	Medium	Medium	Easy	Easy
Integration	Hard	Hard	Fair	Easy

It can be noted that the coaxial cable has a high bandwidth and power capacity next only to waveguides. In addition the preferred Transverse Electromagnetic Mode (TEM) mode of propagation ensures dispersion free performance with no cutoff frequency. Based on the above, a coaxial transmission line offers the most desirable performance. The integration issues with other circuitry have confined it to circuit board level and RF system level applications. On the other hand, planar transmission lines such as coplanar waveguides (CPW) and microstrip lines are small in size, easy to fabricate and integrate, which makes them useful for modern on-chip applications. But microstrip and CPW lines are not shielded like coaxial lines, which means they are vulnerable to cross-talk and spurious responses in high density circuits. A waveguide offers a shielded construction, but its preferred TE_{10} mode of propagation restricts its usage to low bandwidth applications. Moreover, constructing a waveguide for on-chip applications is an extremely challenging task. The closest contender to a coaxial line is a stripline, which can be fabricated by stacking layers of dielectric-conductor-dielectric to form a vertically shielded structure that is fairly easy to integrate with on-chip circuitry using transitions. The only disadvantage of stripline is the absence of the shielding on its sides, which could lead to lateral coupling in closely spaced circuitry.

In summary, a coaxial line would be the most suitable candidate for a multitude of RF/microwave applications, if the integration and fabrication issues are addressed. Coaxial lines can also be used in high power applications by suitable modifications to its construction. Power handling capacity of a coaxial line is characterized by the breakdown strength of the dielectric filling the coaxial line and the thermal properties of the inner conductor. So, the power handling can be greatly improved by filling the cavity with higher dielectric strength materials and conductors made of high electrical and thermal conductivities (like copper) that can dissipate heat more effectively to ensure high power operation.

The main motivation behind this work was to explore the feasibility of miniaturizing a coaxial cable suitable for on-wafer applications in terms of design, fabrication and integration with other on-wafer devices. The cross-sectional dimensions of the proposed rectangular coax lines were chosen to be less than 500 µm in width and 20 µm in height to facilitate on-wafer integration. A low height profile is one of the distinguishing features of this work, while a rectangular cross-section was chosen to simplify the fabrication process. This new type of coaxial lines conforming to sub-millimeter dimensions are broadly referred to as ‘Micro Coaxial Transmission Lines’ (also called as ‘micro coax’ in this work). A significant part of the research involved developing processes to fabricate these structures along with standard microwave planar and RF MEMS devices. Process development includes evaluation of materials for structural/sacrificial layers and maintaining process temperatures to suit the IC manufacturing industry.

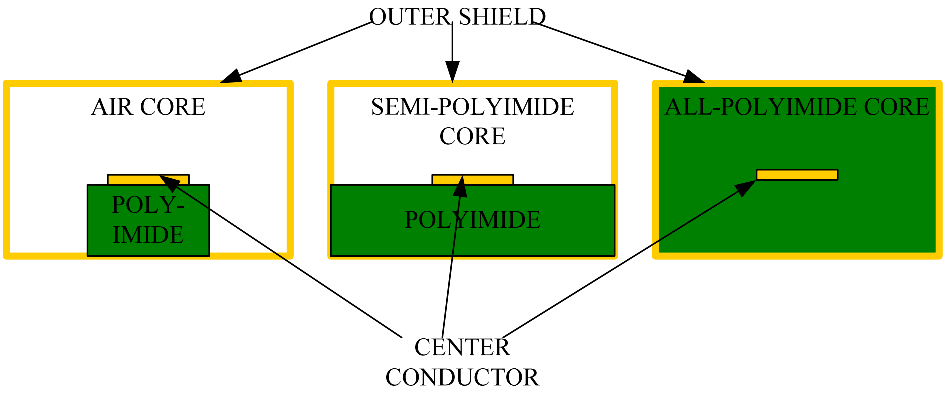

Figure 1.2 Different Types of Micro Coax Cores

The most suitable process steps and materials were used to realize micro coax lines of three different core types, including air, semi-polyimide and all-polyimide cores as shown in Figure, referred to as First, Second and Third generation micro coax lines respectively. This technology was further extended to demonstrate different applications and integration/transition aspects of the micro coax lines.

First Generation Micro Coax Lines-the first generation micro coax lines were designed using an air core by supporting the center conductor on periodically spaced polyimide pedestals, resembling a continuous multi-section fixed-fixed beam. The pedestals and the center conductor are enclosed in a metallic shield on the sides, bottom and the top. The top shield is also suspended in air, supported on the side shields. The conductor width was varied to get lines of different dimensions and characteristic impedance values, operating between 1 and 40 GHz. This design had the lowest loss and was readily amenable to RF MEMS devices. However the lack of mechanical stability in the center conductor and the top shield prompted the development of the next generation design.

Second Generation Micro Coax Lines-Semi-polyimide lines were made of a continuous platform of polyimide instead of pedestals and a suspended top shield. This led to an increase in the signal loss contributed by the additional volume of lossy polyimide dielectric inside the core. The higher losses were considered a trade-off for the reduction of process steps and increased mechanical stability compared to the air core design.

Third Generation Micro Coax Lines-All-polyimide core design with the center conductor sandwiched between two polyimide layers of the same thickness was designed, fabricated and measured. The outer surfaces of the polyimide were metallized to form the external shield for the micro coax line. The signal loss increased further compared to the semi-polyimide lines due to the all-polyimide construction, but the fabrication process was simplified to a great extent due to the absence of suspended members.

Success of the basic micro coax implementation on a silicon wafer prompted the extension of this technology to integrate an RF MEMS device inside the cavity of a semi-polyimide micro coax line. An electrostatically actuated RF MEMS variable capacitor was designed, fabricated, measured and modeled as part of this research. This capacitor was located inside the micro coax cavity, making it completely shielded and integrated within the transmission line. The micro coax line was terminated in planar ground-signal-ground probe pads for measurements. A capacitance ratio of 6.5 was achieved with an actuation voltage of 40-60 volts. It is believed that this is the first implementation of an RF MEMS device in a completely shielded micro coax cavity. The MEM capacitor can be modified to realize an RF MEMS switch, filter, phase shifter, etc depending on the application. A design and process flow to realize an RF MEMS shunt capacitive switch inside a micro coax core has been introduced in this research.

In an attempt to exploit the three dimensional structure of the micro coax design, a miniaturized 'H' shaped slot antenna operating in the 55-65 GHz range was fabricated on the top shield of the micro coax with its center conductor electromagnetically coupled to the slot situated 10 μm above the feed line. The inherent shielding provided by the coax feed could help in reducing the coupling losses typical in electromagnetically coupled feeds. A slot length reduction of 50% was achieved by using an H-shaped slot and integrating it on the shield of the feed line. The antenna exhibited a return loss better than 15 dB, 17% bandwidth and a radiation pattern close to full wave Ansoft HFSS simulations in the design frequency band of 55-65 GHz.

Lastly a diversified application of the micro coax technology has been introduced as part of recommended future work, which involves using an open-ended micro coax line integrated with a microfluidic chamber as a probe for biological impedance measurements. The impending threat and large scale destruction that could be caused by deadly outbreaks such as the recent (2006) E-coli attack on spinach calls for a highly sensitive and rapid detection method to avoid such dangers in future. One of the sensing methodologies that have been researched for the past few decades involves impedance measurements of a biological sample to sense the presence of bacteria. It is believed that each type of bacteria or any living cell has a characteristic impedance fingerprint which is a result of their unique cell capacitance. Impedance is measured using the micro coax probe by immersing the open end of the probe inside a microfluidic chamber containing the fluid under test. The other end is terminated in ground-signal-ground probe pads for measurement. Impedance data was obtained from measured 1-port S-parameters using a vector network analyzer. The difference in impedance between a monitor and the test sample is used to create an impedance fingerprint for the bacteria-under-test. The impedance measurement technique can be further extended to detect other micro organisms too. The micro scale cross-sectional area of the probe allows the use of small volume (5 μl) test samples, which could help in increasing the sensitivity of the detection.

1.2 Contributions

The following contributions have been made to the microwave community through this doctoral research work.

a. Development of an on-wafer micro coax transmission line-a rectangular micro coax transmission line topology to suit standard microfabrication was developed in air, semi-polyimide and all-polyimide core configurations. The work presents significant advances from the introduction of this technology in the 90s in terms of design, fabrication, modeling and applications up to 65 GHz. A low height profile of 20 μm is one of the distinguishing features of this work compared to other micro coax designs.
b. RF MEMS Variable Capacitor-Implementation of a functional RF MEMS variable capacitor inside the micro coax cavity to produce a shielded MEMS device integrated with a transmission line operating up to 40 GHz. A capacitance ratio of 6.5 was obtained with an actuation voltage of 40-60V. To the best of the author’s knowledge this is the first time an RF MEMS device has been implanted inside a shielded micro coax transmission line
c. Micro Coax Fed Slot Antenna-A millimeter-wave slot antenna was integrated on the top side shield of an all-polyimide core micro coax feed line to produce a highly compact and shielded slot antenna-feed network. A bandwidth of 17% and a return loss better than 15 dB was achieved in the 55-65 GHz band. To the best of the author’s knowledge, this is the first implementation of an integrated micro coaxial fed slot antenna operating in the unlicensed 57-64 GHz band

1.3 Organization of Dissertation

Chapter 2 provides a basic introduction to various transmission line types and a brief literature survey of presently available micro coax transmission line designs, fabrication methods and their performance. Design aspects of the three generations of micro coax line topologies-air core, semi-polyimide and all-polyimide types, proposed in this dissertation are discussed followed by fabrication steps and pictures of fabricated devices.

Chapter 3 presents the results and analysis for the three generation micro coax designs. An analysis of design trends including the effect of different characteristic impedances, holes in the center conductor and top shield is presented. The effect of cross-coupling between adjacent micro coax lines and the effect of bends in a micro coax line was studied in the context of using these lines for large scale integration and vertical interconnect applications. An equivalent circuit model has also been proposed to extract the lumped element equivalent circuit of the proposed micro coax lines.

Chapter 4 presents the adaptability of the proposed semi-polyimide micro coax lines to RF MEMS devices. A MEM variable capacitor was located inside the shielded cavity of a semi-polyimide micro coax line proving the adaptability of the new micro coax topology to RF MEMS devices. An improved MEM capacitor with a higher capacitance ratio has also been proposed to be configured as an RF shunt capacitive switch. Measured results of the variable capacitor and the simulation results of the RF switch have been compared and analyzed with respect to the present state-of-the-art in RF MEMS technology.

Chapter 5 demonstrates the vertical integration capabilities of an all-polyimide micro coax line with a 55-65 GHz slot antenna etched on its top shield. The antenna was electromagnetically fed by the center conductor 10 μm below it. The design and optimization of the slot antenna and its feed have been discussed. Measured return loss and radiation pattern results have been presented with analysis and comparison with previously published results for similar antennas.

A comprehensive summary and recommendations for future work are provided in the Chapter 6.

Chapter 2

Micro Coaxial Transmission Lines

2.1 Introduction

Microstrip and coplanar waveguide transmission lines are commonly used for on-wafer applications due to their planarity which allows easy fabrication and integration with other circuitry. The issues of cross-talk and radiation in microstrip and coplanar waveguide transmission lines have always been a topic of research and discussion [2]. However, with the rising frequency needs of today's integrated circuitry, the limitations of microstrip and coplanar waveguides such as cross-talk and radiation losses are gaining significance [3]. The ever increasing demand for wafer real estate has led to the shrinking of chips and denser packing of circuits. This trend calls for a shielded transmission line structure amenable to large scale integration and immune to coupling or radiation effects. Extensive research has been done to modify common planar transmission lines such as microstrip and coplanar waveguides to partially shielded lines using techniques such as suspending the transmission lines on a thin silicon membrane [4], buried microstrip lines [5], shielded microstrip lines [6] and semi-coaxial transmission lines [7] to name a few. The types of transmission lines that offer good shielding are waveguides and coaxial transmission lines. Waveguides are physically bulky even at millimeter-wave frequencies and have a low bandwidth. This makes them unsuitable for wafer level and high bandwidth applications. Coaxial transmission lines on the other hand are relatively small and have a pure TEM mode of propagation, which makes them virtually frequency independent. Implementation of a coax to CPW or microstrip transition is fairly simple compared to a waveguide to planar transition.

This chapter presents a brief history of rectangular micro coax related theory followed by design and fabrication steps used in this research to develop a micro coax transmission line technology for on-wafer applications. Three different physical structures based on the dielectric filling of the micro coax cavity have been analyzed and compared with respect to the characteristic impedance (Z_0) of the lines, perforation density in the center conductor and the top shield. The main use of perforations is to facilitate sacrificial layer removal during the fabrication process, but they also provide a measure of Z_0 control keeping the width constant. The effect of bends in a micro coax line is analyzed by comparing the return and insertion losses of a straight and meandered micro coax line of the same effective lengths. High Isolation between two closely spaced micro coax lines has been demonstrated at millimeter-wave frequencies.

2.2 History of Rectangular Coaxial Transmission Lines

Rectangular coaxial transmission lines have been of interest to researchers from the early 1950s. Research in those days involved analyzing the electromagnetic theory behind these devices to understand their behavior and formulate equations to model them. Cohn was one of the first researchers to propose a non-circular coaxial line in 1954. His work [8] documents equations to compute the characteristic impedance of square coaxial lines. A doctoral thesis [9] from the University of Wisconsin from the same year presented analytical concepts about rectangular coax lines. This was followed by Chen [10] in 1960 with equations to calculate the capacitance, inductance and thereby the characteristic impedance of a rectangular coaxial transmission line. Garver's work [11] published in 1961 presented a simplified equation to calculate the characteristic impedance of a rectangular coax line applying the concepts put forth by Skiles [9] and Chen [10]. Later in 1962, Getsinger [12] compared a set of coupled rectangular bars between parallel plates to a rectangular coaxial line and presented curves showing the even-odd-mode and fringing capacitances formed by the coupled center conductor with the top and bottom shielding. The following years, 1963-64 saw refinements to the square coaxial characteristic impedance equations by Green and Conning respectively [13], [14]. Cruzan and Garver published a wide range of characteristic impedances from corner capacitance values of rectangular lines in 1964 [15]. The 1970s and early 80s saw the emergence of more complex rectangular coax designs with thin and offset center conductors and air dielectric like the one described in [16]. The pioneering work of all the above mentioned researchers paved the way for today's on-wafer rectangular micro coax designs.

The history of rectangular coax lines clearly reveals that the concept was limited to theoretical analysis until the 1970s. After about 21 years, in 1991, a three dimensional rectangular micro coax transmission line was fabricated using a VLSI-friendly fabrication process for high speed interconnect applications [2]. The results presented were mostly confined to the manufacturability and mechanical aspects of the design. The microwave characterization was limited to the determination of the characteristic impedance of the lines. Several other researchers have been working on developing micro coax transmission lines for on-wafer applications since that time. Table 2.1 shows the major milestones in the evolution of micro coax technology from 1991 to 2007. It may be noted that four unique fabrication methods have been adopted by researchers. Except for the first two and this work, the others have utilized specially developed three dimensional fabrication methods based on stereo lithography and prototyping techniques. The corresponding device dimensions are large relative to the present state-of-the-art planar microwave circuitry. Interestingly the designs presented by Bishop *et al.* back in 1991 have the smallest cross-sectional area (with a height of 10 μm) and were fabricated by standard process steps [17]. The low height makes integration possible with other on-wafer microwave circuitry. The small size and the probimide (loss tangent >0.1 at high frequencies) filled cavity are the main contributors of the high insertion loss of 16 dB/cm. Jeong *et al.* introduced a BCB (benzocyclobutene, a type of polymer) filled micro coax design in 2000 and followed by an air-filled coax design in 2002 [18], [19]. The return and insertion loss of the air-filled lines was better than 30 dB and 0.8 dB/cm respectively. Though it was a low loss design, relatively large dimensions makes it difficult to achieve on-wafer integration.

Brown *et al.* revealed a three dimensional micro coax design fabricated by the EFAB™ stereo-lithography process in 2004 [20]. This process involved stacking alternating layers of metal/dielectric and sacrificial polymer followed by chemical mechanical polishing. Finally the polymer is removed leaving the micro coaxial components behind. The micro coax lines fabricated by this technique are about 300 μm in height. Though they exhibit excellent microwave performance up to 40 GHz, they are relatively bulky when compared to a nominal silicon wafer thickness of 250 to 400 μm. Nevertheless this technique has been used to realize micro coaxial couplers, filters, resonators, etc. [21], [22]. Excellent microwave performance was achieved with micro coax lines of similar physical structure and size introduced by Filipovic *et al.* in 2006 [23]. They were fabricated using a patented fabrication technology called PolyStrata™ developed by Rohm and Haas. However, both the EFAB™ and Polystrata™ devices are disadvantageous in terms of large size and a complex fabrication method, which may not be suitable for RF MEMS integration.

All the above mentioned factors were taken into consideration when developing the micro coax lines presented in this research. The designs presented in this work are 470 μm wide and 20 μm tall making them three dimensional, yet not too far away from other planar counterparts. The adaptability of the designs to vertical integration, MEMS devices and transition to planar circuitry has been demonstrated.

Table 2.1 Evolution of Micro Coax Transmission Lines

Research Group And Year	Description	Fabrication Technique	Cross-section $(\mu m)^2$
Jennifer A. Bishop *et al.* (1991)	transmission lines	GaAs substrate, gold plating, probimide filled cavity, gold conductor	(5 to 35) × 10
In-Ho Jeong *et al.* (2000)	transmission lines	gold plating, BCB dielectric spacers, gold conductors	150×60
In-Ho Jeong *et al.* (2002)	transmission lines	gold plating, air dielectric, gold conductors	150×60
E. R. Brown *et al.* (2004)	transmission lines	EFAB Process, stereo lithography	300×300
R. T. Chen *et al.* (2005)	30 GHz coaxial filter	EFAB Process, stereo lithography	-
J. R Reid, E. D. Marsh, R. T. Webster	transmission lines and resonators	EFAB Process, stereo lithography	~ 300×300
D. S. Filipovic *et al.* (2006)	transmission lines, resonators and couplers	Rohm and Haas Polystrata™ process	250×310
This Work (2004-2007)	transmission lines, bends, MEMS device, antenna and micro coax probe	low height profile polyimide, gold electroplating	470×20

2.3 Micro Coax-Substrate Dependence and Wave Propagation

Physical dimensions and the performance of planar transmission lines are heavily dependent on the substrate due to the nature of the electric field distribution. The substrate effects are accounted for by the inclusion of the effective permittivity and loss tangent values in the design. In the case of a coaxial line the electric field emanates from the center conductor and terminates on the outer shield unlike in other planar transmission lines, where the field lines penetrate the substrate before terminating at the shield at the bottom of the substrate as shown in Figure 2.1. So, when a rectangular coax is placed on a substrate, it is not affected by substrate parameters.

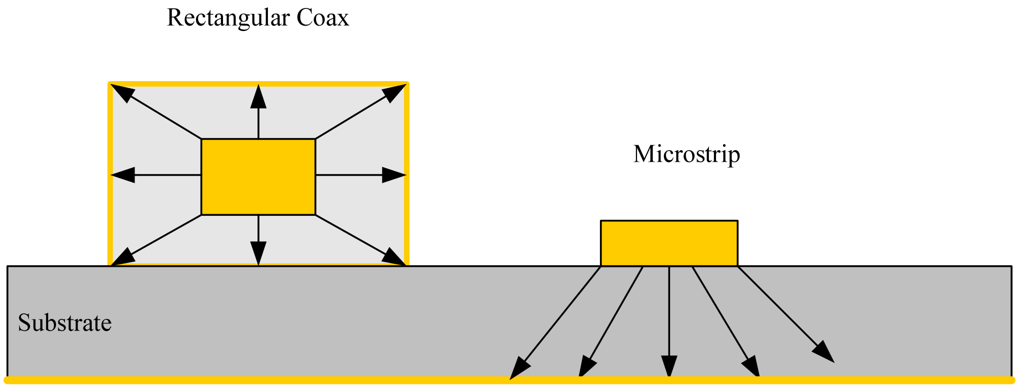

Figure 2.1 Rectangular Coax and Microstrip Field Lines

The electromagnetic wave propagation in a coaxial transmission line is a type of 'Guided Wave' because it is guided through its path by a metal or a dielectric. Simple two-wire transmission lines and waveguides are other examples of guided wave transmission lines. There are two fundamental modes of wave propagation namely, Transverse Electric (TE) and Transverse Magnetic (TM) modes. In Figure 2.2 , 'z' is the direction of wave propagation and 'x', 'y' represent the direction of the Electric (E) or the magnetic (H) field.

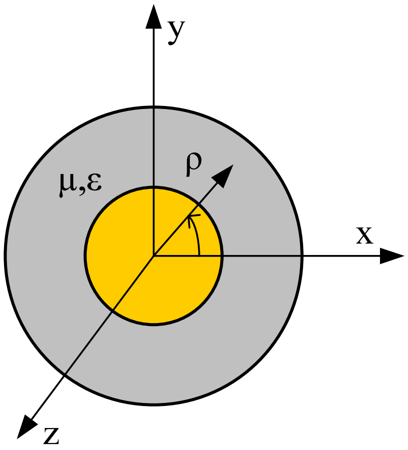

Figure 2.2 Field Orientation in a Coaxial Line

TM waves are those with a non-zero E-field component in the direction of wave propagation ('z' direction) and a zero H-field because the magnetic field is completely transverse. On the other hand, the presence of a non-zero H-field in the 'z' direction with a zero E-field makes it a TE wave. In a special case of TM waves, when both the E and H-fields are zero in the direction of propagation, both the electric and magnetic field is transverse, which gives rise to a Transverse Electromagnetic Wave (TEM). This is the principal mode of wave propagation in a coaxial line. Other modes such as the TE and TM are possible as evanescent modes or cut-off modes. The distinguishing features of TEM waves are-

a. E and H-fields are constant in amplitude along the normal to direction of propagation
b. Lower and upper cut-off frequency for a TEM wave is zero and infinite, respectively
c. TEM mode allows a far smaller separation compared to TE and TM modes (in wavelengths) between the two conductors making the dimensions practical at low MHz frequencies

2.4 Micro Coax-Characteristic Impedance

The physical dimensions and thereby the characteristic impedance (Z_o) of transmission lines such as microstrip, CPW, etc. are a function of the thickness and dielectric constant of the substrate. On the contrary, coaxial line parameters are totally independent of substrate parameters.

The variables that control the Z_o of a rectangular coax transmission line are-

a. Width of the center conductor
b. Distance from the center conductor to the top and bottom ground shields
c. Spacing between the center conductor and the side shields
d. Permittivity of the dielectric filling the cavity

In addition to the above mentioned parameters, the loss tangent of the dielectric filling the cavity, thickness of the center conductor (for thin conductors) and the shield play a role in determining signal loss. These above mentioned losses can be accurately predicted using full wave electromagnetic simulations or analytical techniques such as conformal mapping. A typical micro coax structure used in this research is shown in Figure 2.3.

-The following sections present a detailed description of rectangular coax design using design equations developed through the 70s. A rectangular coax line is in principle, a pure transverse electromagnetic mode (TEM) two-wire transmission line. When conductor, dissipation and dielectric losses are neglected, the characteristic impedance becomes a simple function of line capacitance and the phase velocity.

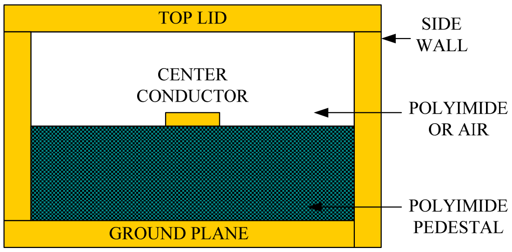

Figure 2.3 Cross-section of a Typical Rectangular Micro Coaxial Transmission Line

A simple expression to calculate Z_o of any lossless transmission line is given by-

$$Z_o = \sqrt{\frac{L}{C}} = \frac{1}{V_m . C} \tag{2.1}$$

$$V_m = \frac{V}{\sqrt{\varepsilon_{eff}}} \tag{2.2}$$

Where,

L - Inductance of the line in H/m

C - Capacitance of the line in F/m

V - Velocity of propagation in free space = 2.998×10^8 m/sec

V_m - Velocity of wave propagation in a medium other than air

ε_{eff} - Effective permittivity of the propagation medium (varies according to volume of dielectric in the micro coax cavity)

It can be observed from (2.1) and (2.2) that the characteristic impedance is a simple function of the dielectric constant of the substrate (or medium) and the line capacitance. In the case of a coax, the permittivity of the dielectric material around the center conductor is considered the propagation medium. The determination of the line capacitance is relatively simple for a micro coax structure with a square or a circular cross-section. A micro coax of circular cross-section was not attempted due to the complexity expected in fabrication. On the other hand, realizing a square cross-section requires the height of the micro coax line to be equal to the width and length, which would necessitate special fabrication steps to planarize thick layers of photoresist and other structural material. As mentioned earlier, a low vertical height profile is one of the unique features of this work. So, a rectangular cross-section was chosen to keep the height constant at 20 µm. The line capacitance of a micro coax line of rectangular cross-section is a combination of the following capacitance values as illustrated in Figure 2.4 where,

a. Capacitance between the center conductor and the top shield
b. Capacitance between the center conductor and the bottom shield
c. Capacitance between the corners/side of the center conductor and the side walls

Determination of the corner capacitance of a rectangular coax line is a challenging task due to the varying electric flux magnitudes at the corner. This flux variation is caused due to inequalities in the vertical and lateral spacing between the center conductor and the shield. Researchers [9], [16] have proposed various methods such as the relaxation method, direct measurement of model method, electrolytic tank measurement method, orthonormal block analysis and the Schwarz-Christoffel or conformal transformation method to evaluate the total capacitance of a rectangular coax line.

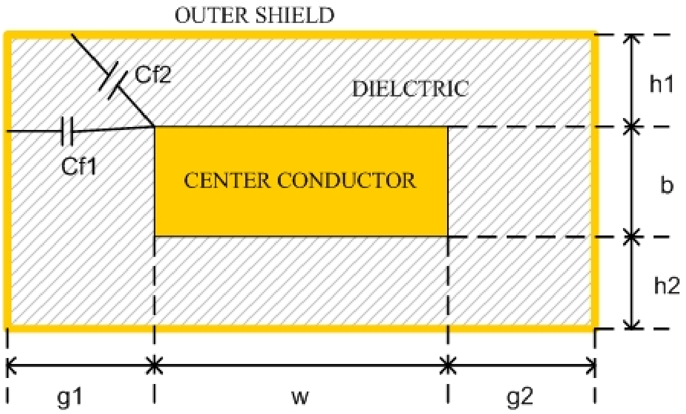

Figure 2.4 Rectangular Coax Dimensions and Corner Capacitances

The complexity involved in corner capacitance computations increase multifold when asymmetry is introduced in the rectangular coax. For example: h1 ≠ h2 or g1 ≠ g2. These variations may be intentionally introduced for special applications or maybe the result of fabrication tolerances or misalignments. Chen's [9] extensive research on the determination of the capacitance, inductance and characteristic impedance of rectangular coax lines using the conformal transformation method was used as the basis for the design of the rectangular coax lines presented in this dissertation. Equations to determine the capacitance and the characteristic impedance of the two most commonly applied designs are presented below.

Case 1-Rectangular coax with a thin inner conductor (thickness of the conductor less than one-third of the total height of the coax or b<d/3)

$$C = \left(\frac{4\varepsilon w}{d-b}\right) + \frac{4\varepsilon}{\pi}\left(\left(\frac{d}{d-b}\right)\times\log\left(\frac{2d-b}{b}\right) + \log\left(\frac{b(2d-b)}{(d-b)^2}\right)\times\log\left(\frac{1+\coth\left(\frac{\pi g}{d}\right)}{\log 2}\right)\right) \qquad (2.3)$$

Where,

C - total line capacitance in Farad/m

d - total height of the coax = b+h1+h2 (as shown in Figure 2.4)

$\varepsilon = \varepsilon_o \varepsilon_r$, where ε_o is the permittivity of free space = 8.8542×10^{-12} (F/m) and ε_r is relative permittivity of the dielectric filling the cavity of the coax (taken as 5 for the HD4010 polyimide used in this research)

Once the capacitance 'C' is known, the characteristic impedance can be calculated using equation (2.1), where ε_{eff} is the effective permittivity of the dielectric material inside the coax cavity, which can be calculated using the ratio of the air to polyimide inside the micro coax core.

Case 2-Rectangular coax with finite thickness inner conductor and lateral/vertical offsets (h1≠h2 and/or g1≠g2) which could be caused by dimensional and alignment variance errors. The capacitance of such a line is given by-

$$C = \varepsilon\left(\frac{b}{g_1} + \frac{b}{g_2} + \frac{w}{h_1} + \frac{w}{h_2}\right) + \sum_{m=1,2}^{n=1,2}\frac{\varepsilon}{\pi}\left(\log\left(\frac{g_n^2+h_m^2}{4h_m^2}\right) + 2\left(\frac{h_m}{g_n}\right)\arctan\frac{g_n}{h_m}\right) +$$

$$\sum_{m=1,2}^{n=1,2}\frac{\varepsilon}{\pi}\left(\log\left(\frac{g_n^2+h_m^2}{4g_n^2}\right) + 2\left(\frac{g_n}{h_m}\right)\arctan\frac{h_m}{g_n}\right) \qquad (2.4)$$

Again the characteristic impedance can be determined using (2.1). The micro coax lines presented in this work do not have asymmetry or an offset center conductor. So, the real utility of Case 2 in this research is to predict and account for the change in Z_o due to fabrication issues.

2.5 Micro Coax-Loss Mechanisms

The losses associated with a dielectric core micro coax line can be attributed to conductor and dielectric loss. Radiation loss which plays a significant role in planar transmission lines does has negligible effect on coax lines due to their outer shielding.

2.5.1 Conductor Loss

The conductor loss (α_c) associated with a transmission line can be estimated using the Wheeler incremental inductance rule as-

$$\alpha_c = \frac{P_{tc}}{2P_o} \tag{2.5}$$

Where, $P_{tc} = I^2 R$ = power loss in the conductor per unit length and $P_o = \frac{V^2}{2Z_o}$ = reference power. The line resistance 'R' can be represented in terms of change in inductance ΔL when the conductor walls are receded by skin depth $\frac{\delta_s}{2}$, permeability μ and conductivity σ of the metal as –

$$\alpha_c = \frac{\Delta L}{\sigma \mu \delta_s^2 Z_o} \tag{2.6}$$

It is known that the inductance is related to the characteristic impedance as

$Z_o = LV_p \Rightarrow \Delta Z_o = \Delta L V_p$. So equation (2.6) can be rewritten as-

$$\alpha_c = \frac{\Delta Z_o}{\sigma \mu \delta_s^2 Z_{o.} V_p} \tag{2.7}$$

This equation can be further enhanced by modifying it to include loss due to the surface roughness of the metal as proposed by Edwards [24].

$$\alpha'_c = \alpha_c \left(1 + \frac{2}{\pi} \arctan \left(1.4 \left(\frac{\Delta}{\delta_s} \right)^2 \right) \right) \tag{2.8}$$

Where Δ is the RMS roughness of the conductor metal.

2.5.2 Dielectric Loss

Dielectric losses play a major role at microwave and millimeter-wave frequencies. Dielectric loss is a function of the loss tangent of the material which in turn is frequency dependent, especially for materials such as polyimide. The main constituent of dielectric loss is the product of line capacitance or susceptance and the loss tangent of the dielectric which causes

a real value of conductance given by $\alpha_d = \dfrac{\pi C\sqrt{\varepsilon_o \varepsilon_r \mu_o \mu_r} \tan\delta}{\lambda_o}$ (Nepers/m) (2.9)

where, λ_o = free space wavelength (m)

$\mu_r = 1$ (since a non-magnetic dielectric is assumed)

$\mu_0 = 4\pi \times 10^{-7}$ (H/m)

$\varepsilon_0 = 8.85 \times 10^{-12}$ (F/m)

C = speed of light = 2.998×10^8 (m/s)

$\tan\delta$ = frequency dependent loss tangent of the dielectric

Equation (2.9) can be rewritten by substituting values for the constants and 1 Neper = 8.686 dB to obtain the loss in dB/m.

$$\alpha_d = \frac{27.287\sqrt{\varepsilon_r}\tan\delta}{\lambda_o} \text{ (dB/m)} \qquad (2.10)$$

Equation (2.10) can be further simplified to obtain the dielectric loss at a particular frequency by substituting $\lambda_o = \dfrac{0.3}{Freq(GHz)\sqrt{\varepsilon_r}}$ which leads to-

$$\alpha_d = 91.021\sqrt{\varepsilon_r}\tan\delta \times Freq(GHz) \text{ (dB/m)} \qquad (2.11)$$

2.5.3 Dispersion

The distortion of a wideband signal at the receiving end of a transmission line due to variation of phase velocity with frequency is called dispersion. This causes complications in high bandwidth circuit design. Phase velocity is given by-

$$V_p = \frac{\omega}{\beta} \tag{2.12}$$

Where, $\omega = 2\pi \times freq$ and β is the phase of the propagation constant (γ).

The propagation constant is given by the equation –

$$\gamma = \sqrt{(R + j\omega L)(G + j\omega C)} = \alpha + j\beta \tag{2.13}$$

This expression for propagation constant is used for a lossy line, where the phase term β is a non-linear function of frequency. This leads to non-linearity in the phase velocity as per (2.12) and causes dispersion in a line. Typically TEM and quasi-TEM transmission lines like coax, microstrip and CPW have a very low to zero dispersion. Prediction of dispersive losses is difficult when dielectric or substrate materials have a dielectric constant and loss tangent that varies with frequency. Even full wave electromagnetic simulators are not equipped to predict dispersion unless the simulator is given a table of frequency dependent loss tangent values. Instead the concept of ‘group velocity’ is used by circuit designers to approximate the phase velocities over a small band of frequencies. However the group velocity approximation is valid only when the dispersion is not severe and the frequency band is small. So, the ideal choice would be to have a dispersion free propagation medium like air. The first generation micro coax lines designed for this research were designed with an air core to achieve dispersion free performance. But an air core design is not always possible due to mechanical design constraints. The next best alternative would be a dielectric material with permittivity closest to air.

2.6 Design and Fabrication of Rectangular Micro Coax Lines

The micro coaxial lines analyzed in this research are divided into three generations of designs.

1. First generation-air core lines with pedestals to support the center conductor and a suspended topside shield
2. Second generation-semi-polyimide core lines with a continuous platform of polyimide to support the center conductor and a suspended topside shield
3. Third generation-all-polyimide core lines where both the center conductor and top shield rest on solid polyimide

Figure 2.5 shows drawings of the three generations of micro coax designs analyzed in this research. The top shield/center conductor holes and the probe pads are not shown in the figure. The type of cross-section is largely based on the application and fabrication constraints. Each generation design has its merits and demerits. The design and fabrication aspects of each type of micro coax is discussed in the following sections.

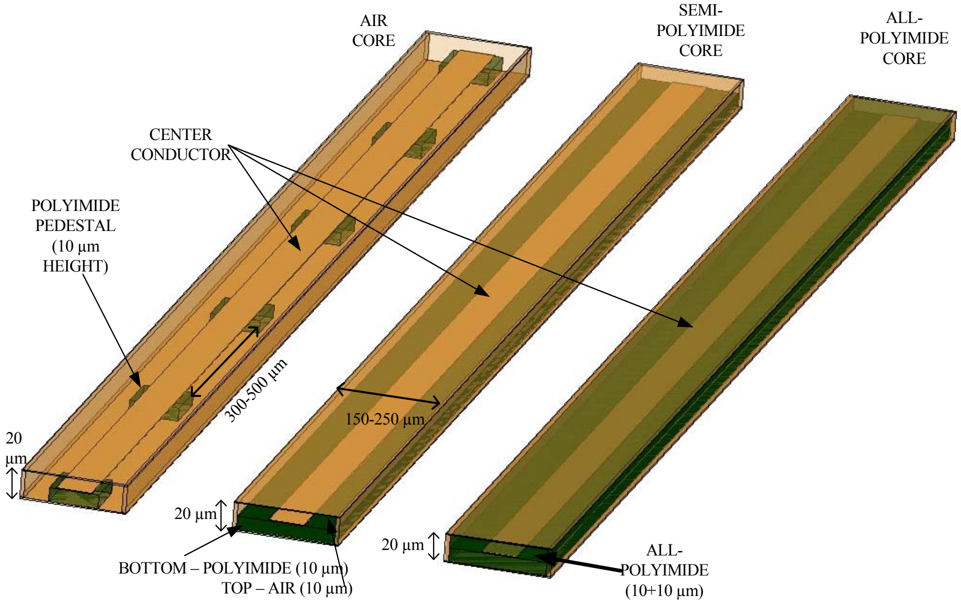

Figure 2.5 Variations in Polyimide Cores

2.6.1 Design of Air Core Lines

Air core micro coax lines represent the first generation devices developed in this research. The center conductor of the air core lines is designed to rest on 10 μm thick polyimide (HD 4010 from HD Microsystems) pedestals periodically placed along the length of the line. This gives it a structure similar to a multi-section fixed-fixed beam. The spacing between the pedestals ranges from 300-500 μm depending on the total length of the line. The total volume of the polyimide inside the micro coax cavity is about 10-12% of the total cavity volume, which can be considered as 'air core'. The micro coax line is terminated by ground-signal-ground probe pads on either ends to facilitate microwave probe measurements. Perforations were made in the center conductor and the top shield to ease the removal of sacrificial layers below the center conductor and the top shield during fabrication. The dimensions and spacing of the holes ranged from 10×10 μm to 25×25 μm depending on the width of the conductor and the top shield. The effect of the holes on the performance of the line was analyzed through HFSS simulations prior to fabrication. A top and cross-sectional view of an air-core micro coax line is shown in Figure 2.6.

The inherent fixed-fixed beam structure in the air core micro coax makes it readily adaptable to a MEM device. A MEM device is basically made of a movable member (or beam) actuated by electrostatic or other mechanisms to create an on/off state or induce tunability in a device. This can be easily achieved in an air core micro coax due its inherent fixed-fixed beam topology by adding a capacitive or a DC contact below one or more of the beam sections. Thus a MEM device can be located inside the micro coax cavity, leading to an integrated and shielded RF MEMS device. The effect of center conductor width and total height of the air core micro coax line on its characteristic impedance is shown in Figure 2.7. The values of characteristic impedance, Z_o were calculated using (2.1)-(2.3) assuming an effective permittivity of 1.6. The center conductor width and the total height were varied between 10-100 μm and 10-40 μm respectively. It can be observed from the plot in Figure 2.7 that Z_o increases with the decrease in center conductor width and/or increase in the total height of the polyimide. This is due to the decrease in the line capacitance, causing an increase in the line impedance. Theoretically, it is possible to continue decreasing the center conductor width or increase the total height to achieve a very high impedance line, but fabrication limitations may render it practically difficult to achieve. Moreover narrower center conductors tend to be lossier. So, an optimum value of Z_0 has to be chosen to suit the application, achieve a reasonable insertion loss within the fabrication constraints.

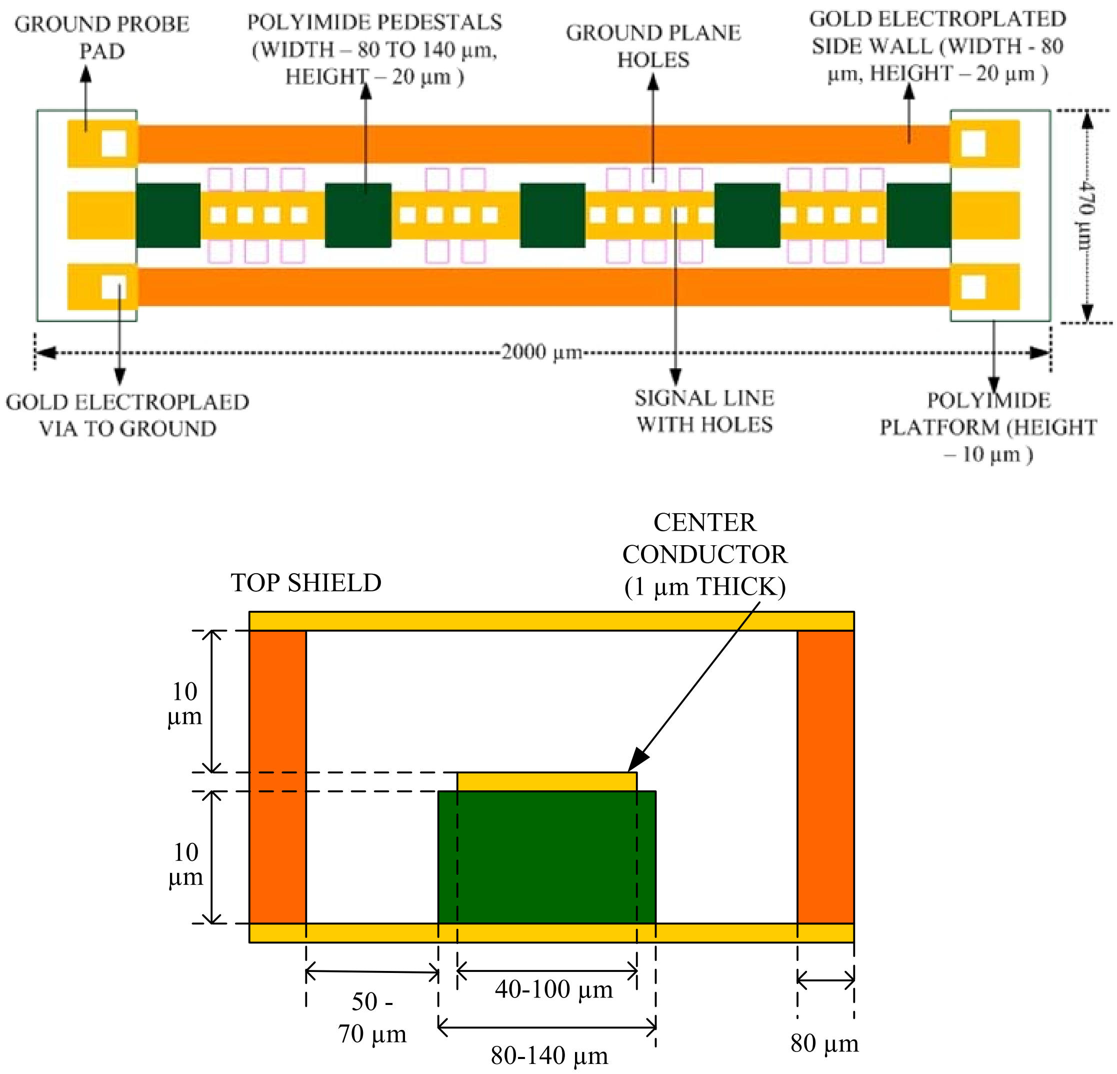

Figure 2.6 Top and Cross-sectional View of an Air Core Micro Coax Line

The effect of the gap between the edge of the center conductor and the side shields was analyzed using (2.4) for an air core line of conductor width 30 µm and total height of 20 µm. Figure 2.8 shows the change in Z_o as the side shields are moved from 10-150 µm away from the edge of the center conductor. It can be seen that the effect of spacing on the characteristic impedance is negligible from 10-30 µm and converges beyond that. This was also confirmed through full wave electromagnetic simulations. This is due to the weak dependence of the spacing in determination of line capacitance as seen in (2.4). Though the spacing of the side shields does not affect the Z_o, their presence is essential to avoid lateral cross-coupling in high density circuits. Moreover side shields are unique to a rectangular coax line that distinguishes it from a conventional stripline. The effect of side shields in reducing the lateral cross-coupling has been demonstrated in Chapter 3.

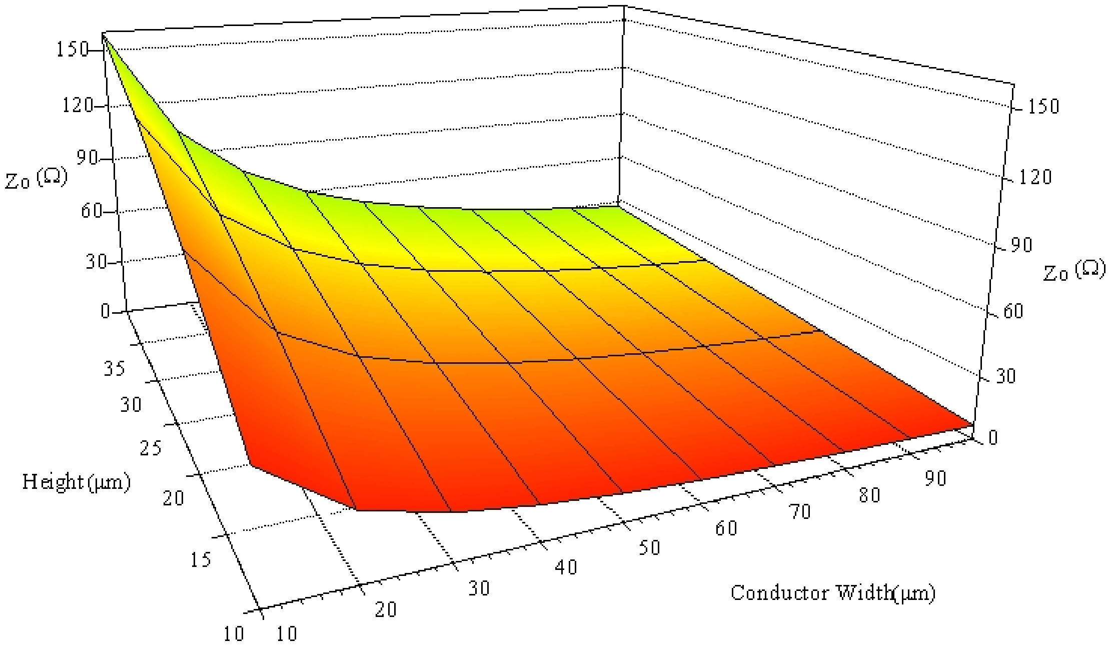

Figure 2.7 Effect of Conductor Width and Total Height on Z_0

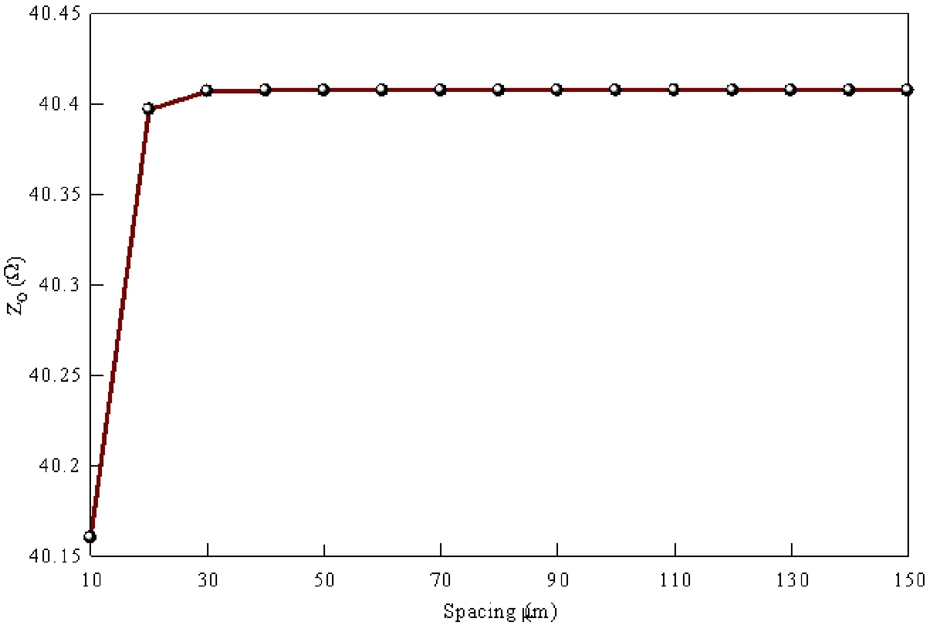

Figure 2.8 Effect of Spacing between Conductor and Side Shields (conductor width-30 μm and total height-20 μm)

Based on the analysis above, air core micro coax lines of the physical dimensions shown in Table 2.2 were fabricated and measured. The height of all the designs was kept constant at 20 μm to simplify the fabrication. Measurement results and analysis are discussed in Chapter 3.

Table 2.2 Fabricated Air Core Micro Coax Designs

Center Conductor Width (μm)	Ground Spacing (μm)	Design Z_o (Ω)
40	50	52
60	50	39
80	60	31
100	70	26

2.6.2 Fabrication of Air Core Lines

The air core lines were fabricated on standard CMOS grade silicon wafers. The substrate independent nature of coax lines makes it possible to implement the same design on any substrate. A process flow developed using standard MEMS processes was used in the fabrication. The fabrication sequence for an air core micro coax line is shown below. The polyimide, photoresist and MEMS processes are explained in detail in Appendix A. Gold electroplating was carried out in a custom made plating setup using a TG25E sulfite based ready to use electrolyte from Technic Inc. Figure 2.9 in the following page shows a step-by-step process flow to fabricate an air core micro coax line.

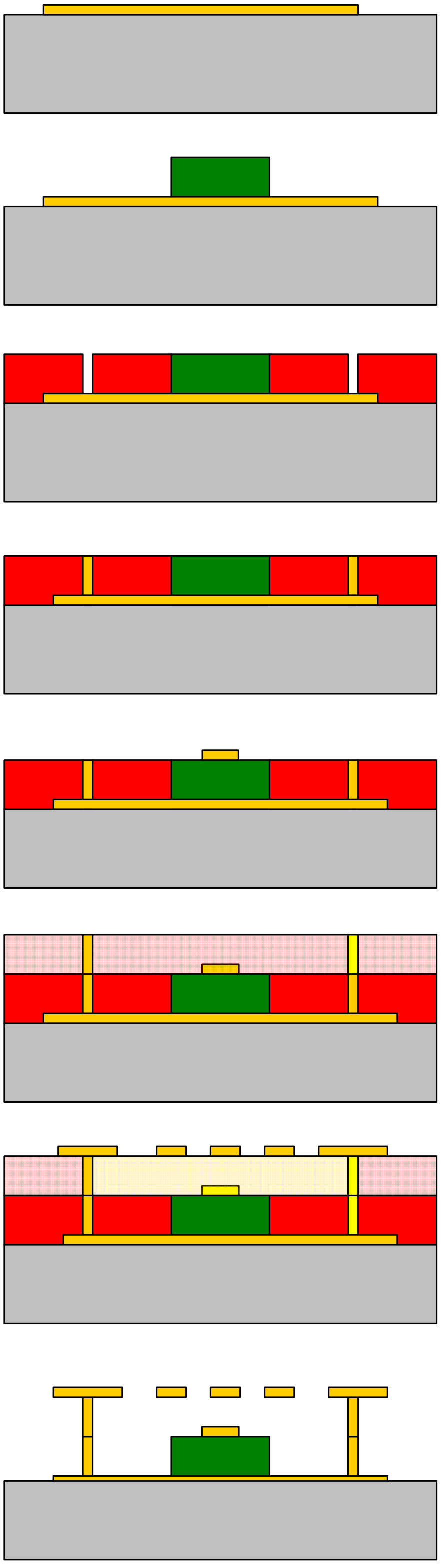

Standard wafer cleaning followed by Bottom ground plane formed by blanket thermal deposition of Cr/Au ~ 4000 A^{o}

Photosensitive polyimide – HD 4010 (10 μm thick) spun and lithographically patterned

10 μm thick AZ 4620 positive resist spun as sacrificial layer and patterned to form plating mould for side wall

Sidewall formed by gold electroplating

Center conductor (made of thermally evaporated Cr/Au ~ 1 μm thick) is formed by lift-off technique using negative photoresist 3000 PY

10 μm thick positive resist - SPR 220-7 spun as top ground plane sacrificial layer and patterned to form plating mould for top half side wall followed by side wall gold plating

Top ground plane formed by thermal evaporation of Cr/Au (~ 1 μm thick), patterned and holes etched using wet etchants

Perform MEM release for the center conductor and the top ground plane using Shipley 1165 remover to remove both the AZ P4620 and the SPR 220-7 followed by critical point dry

Figure 2.9 Process Flow for Air Core Micro Coax Lines

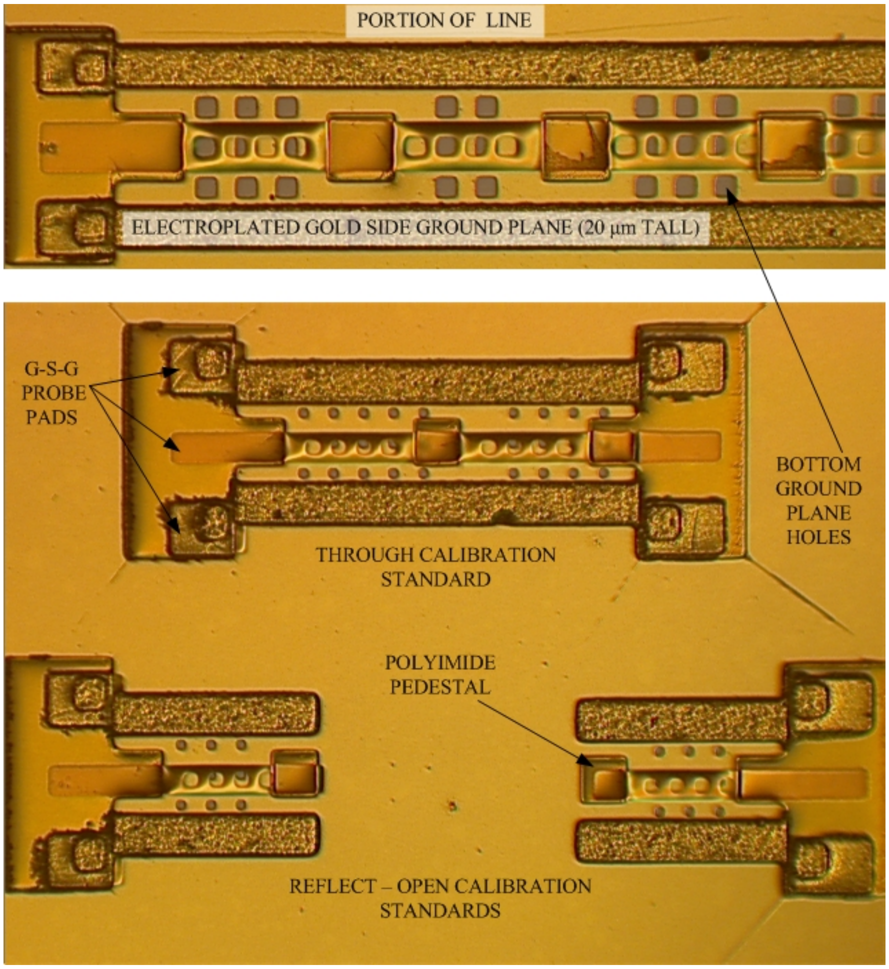

Figure 2.10 Microphotographs of Fabricated Air Core Micro Coax Lines

Figure 2 shows a microphotograph of fabricated air core micro coax lines. The pictures were taken before the top shield fabrication. Fabricated air core lines exposed the mechanical instabilities of the air core design involving a fixed-fixed beam structure. High residual stress in the beam and top shield metal caused multiple sections of the center conductor and parts of the top shield to sag (visible under a microscope) during the release process. Such structural variations had a detrimental effect on the performance and yield of the air core micro coax lines. In view of this, it was decided to simplify the fabrication process by replacing the polyimide pedestals by a continuous block of polyimide, which would ensure the stability of the center conductor.

2.6.3 Design of Semi-Polyimide Micro Coax Lines

The second generation micro coax lines, called semi-polyimide lines were developed to avoid the fabrication issues faced with the air core lines. The center conductor in a semi-polyimide core micro coax line is supported on a continuous platform of polyimide unlike pedestals in the air core design. This led to the increase in the polyimide volume to 50% of the total micro coax cavity volume compared to 10-12% for the air core design. The increased dielectric and dispersion losses due to increase in polyimide volume was a trade-off for the mechanical stability of the center conductor. A top and cross-sectional view drawing of a semi-polyimide micro coax structure is shown in Figure 2.10.

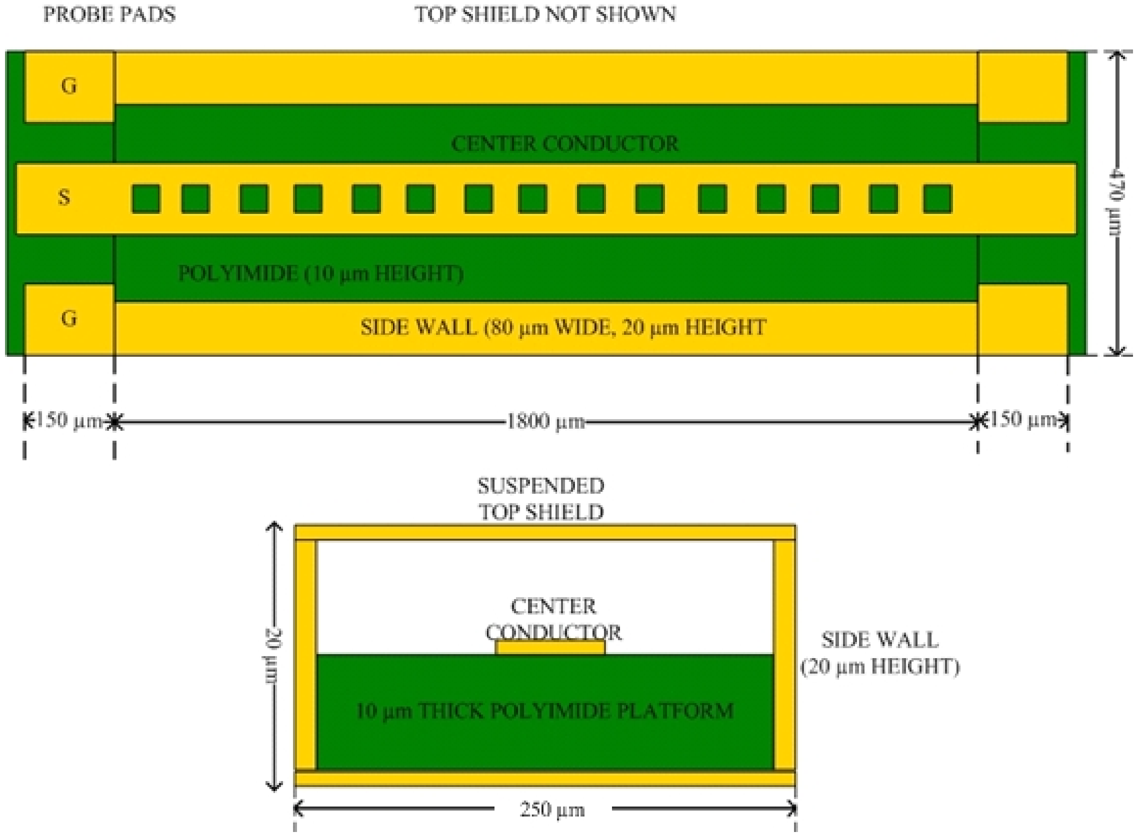

Figure 2.10 Top and Cross-sectional View of a Semi-Polyimide Micro Coax Line

Physical dimensions for conductors, shield spacing and vertical height have been maintained the same as that of the air core design (see Table 2.2). The bottom half of the side shields are buried in the polyimide. The top shield is still a suspended structure supported on the top half of the side shields (see Figure 2.10). The characteristic impedance of semi-polyimide core lines are lower than the air core designs due to higher line capacitance contributed by the continuous platform of polyimide. A 3-D plot showing the effect of conductor width, total height of the micro coax line and the corresponding Z_o values is shown in Figure 2. It can be observed from a plot that a Z_o value ~105 Ω is achievable with a 10 µm wide center conductor and a total micro coax height of 40 µm. However this comes with a steep increase in fabrication complexity. Alternatively, periodic holes were etched in the conductor to reduce the line capacitance (to increase the Z_o), but the maximum porosity that could be achieved was limited to 16.5%, beyond which electromagnetic simulations showed a notable increase in insertion loss. The insertion loss also increases significantly due to the increase in the volume of polyimide inside the micro coax cavity, which increases the dielectric loss. Results and analysis of various semi-polyimide core designs are presented in the following chapter. A comparison of the loss of two micro coax lines of 30 µm center conductor widths and the same length, but one with three pedestals of polyimide and the other one with a continuous block of polyimide is shown in Figure 2.11. The transition from pedestals to a continuous platform of polyimide increased the volume of polyimide from 10-12% to about 50% of the total volume of the cavity. Electromagnetic simulations show that the increased polyimide volume contributes to a 25-30% increase in the insertion loss. The simulations were performed keeping all the other parameters including the loss tangent, permittivity, length of the line, width of the conductor, shield spacing etc are exactly similar for both the designs.

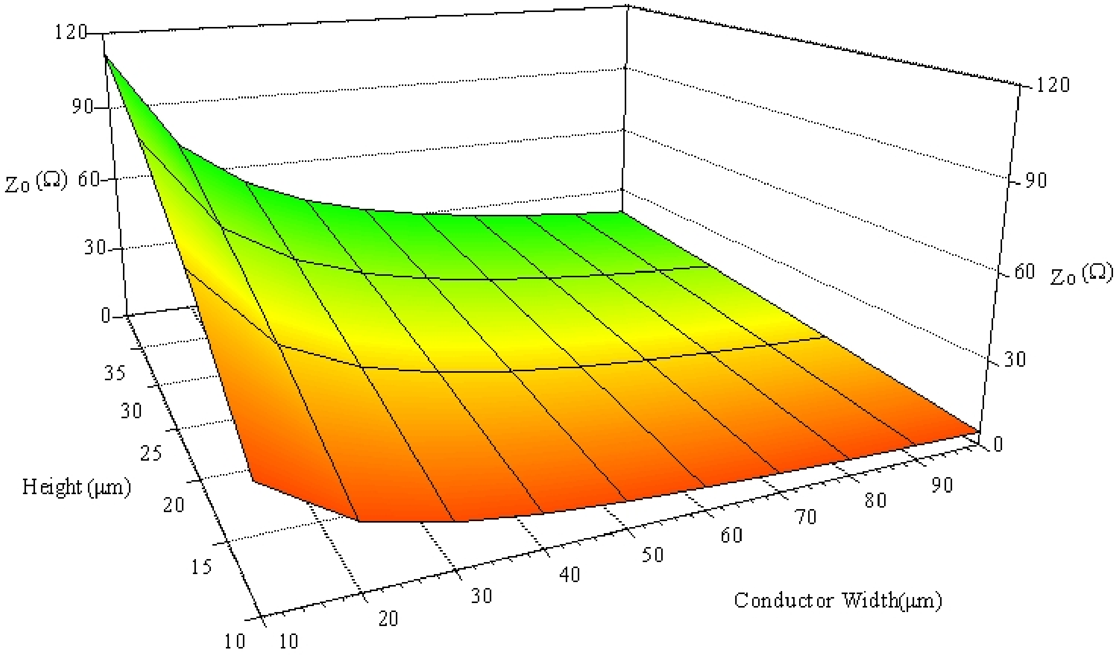

Figure 2.12 Variation of Z_0 with Conductor Width and Height of a Semi-Polyimide Micro Coax Line

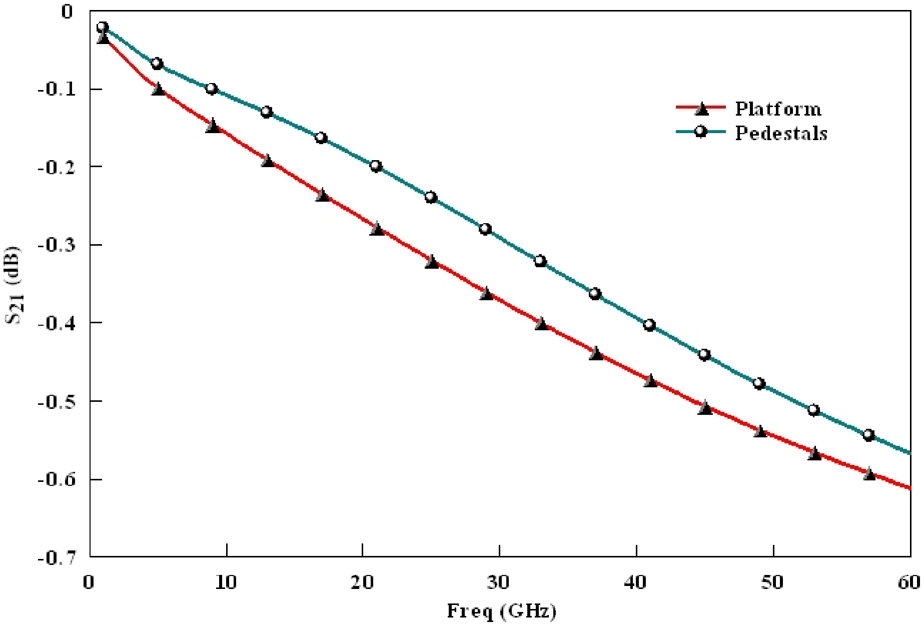

Figure 2.11 Comparison of the S_{21} (dB) of a 1000 µm Long Micro Coax Line with Pedestals and a Platform of Polyimide

2.6.4 Fabrication of Semi-Polyimide Micro Coax Lines

The process flow to fabricate semi-polyimide lines requires fewer process steps than its air core counterparts. The polyimide, photoresist and MEMS release steps are explained in detail in Appendix A. Gold electroplating was carried out in a custom made plating setup using a TG25E sulfite based ready to use electrolyte from Technic Inc.

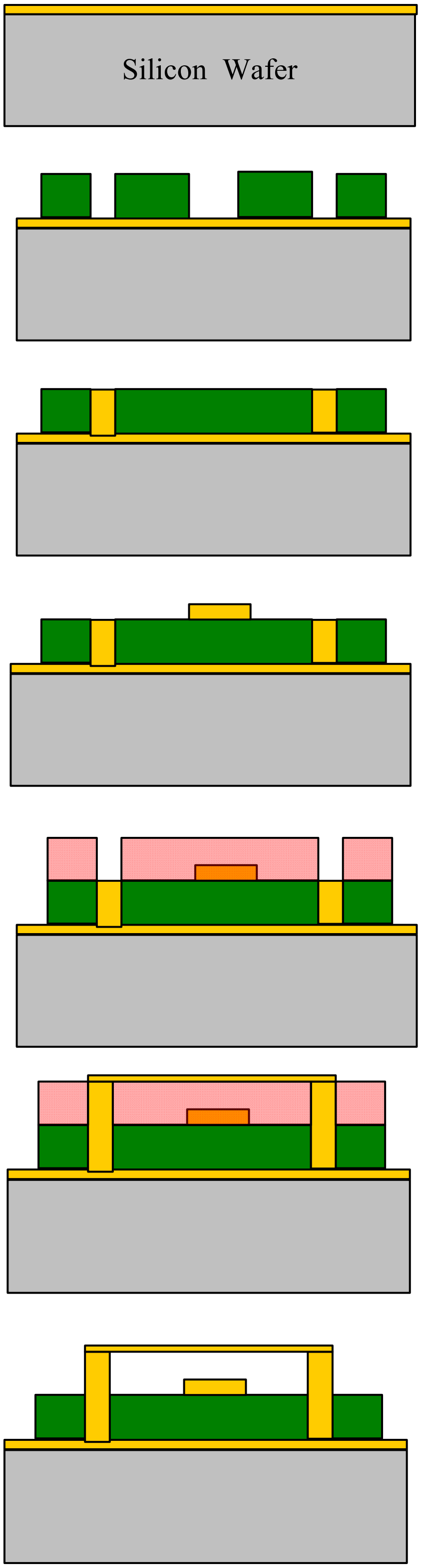

Wafer cleaned and blanket deposited with thermally evaporated Cr/Ag/Au ~ 1 µm thick

10 µm tall platform with a plating mould for the bottom half side wall formed by lithographically patterned polyimide (HD 4010)

10 µm tall side wall formed by gold electroplating

Center conductor formed by Cr/Au lift off using resist – NR1-3000PY

10 µm thick AZ P4620 spun to be used as sacrificial layer for the top ground plane and also as mould for the top half side wall plating

Top half side wall gold plated (10 µm tall)

Sacrificial resist removed using 1165 remover and critical point dry

Figure 2.12 Process Flow for the Semi-Polyimide Micro Coax Lines

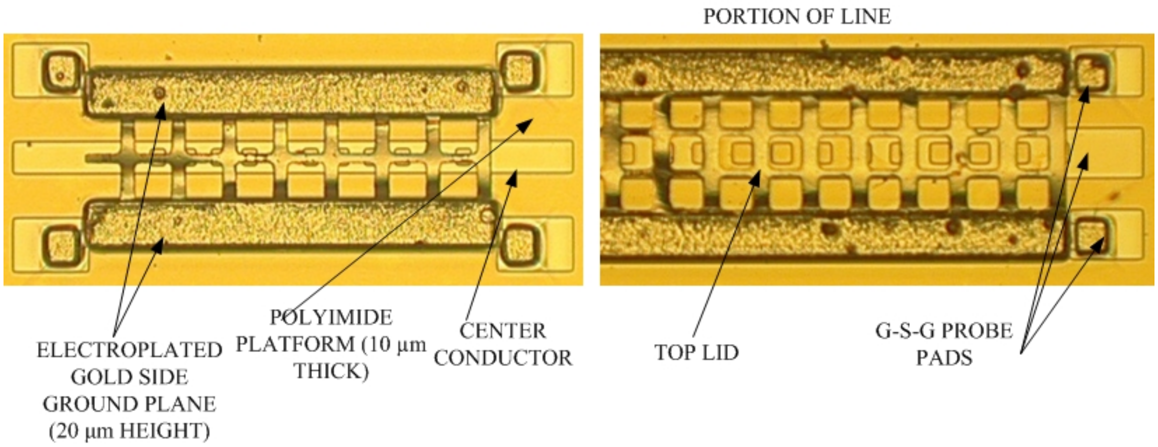

Figure 2.13 Microphotographs of Fabricated Semi Polyimide Micro Coax Lines

Pictures of fabricated devices are shown in Figure 2.13. The picture on the left shows a 1000 µm long ‘Through’ calibration standard. The difference in the hole densities in the top shield and the widths of the center conductor can be observed between the two lines.

2.6.5 Design of All-Polyimide Micro Coax Lines

The all-polyimide type micro coax lines represent the third generation of micro coax designs explored as part of this research. They are made of a solid polyimide filled cavity as shown in Figure 2.14. In principle, an all-polyimide type micro coax line resembles a commercially available macro coaxial line with a Teflon (or similar dielectric) filled core. The signal conductor of the all-polyimide micro coax line is located at the center of the cavity, buried in the polyimide. The external surface of the polyimide core is covered with metal that acts as the outer shield. The primary advantage of the all-polyimide design is the ease of fabrication and high mechanical stability of the center conductor/top shield compared to the other two generations of lines. The conductor width, shield spacing and total height of all-polyimide micro coax lines were maintained constant throughout this research. Electromagnetic simulations predicted a Z_o of 25 Ω for the dimensions indicated in Figure 2.14. Higher impedance designs are theoretically possible as shown in Figure 2.15, but were not attempted because using a narrower center conductor or thicker polyimide layer (to increase the overall height) would lead to fabrication complexity and reliability concerns. As such the all-polyimide lines are expected to have 35% and 70% more signal loss than the semi-polyimide type and the air core type polyimide line respectively at millimeter-wave frequencies. This is due to the higher losses in narrow conductor/ground planes caused by high current densities and the use of lossy polyimide (loss tangent ~ 0.04 to 0.08 at millimeter-wave frequencies) inside the core of the coax lines. The frequency dependent loss tangent of the polyimide was calculated from the S-parameter measurements of a metal-polyimide-metal capacitor structure as explained in Appendix B.

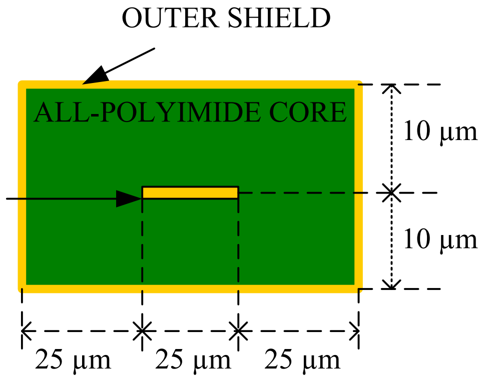

Figure 2.14 Cross-section of an All-Polyimide Core Micro Coax Line

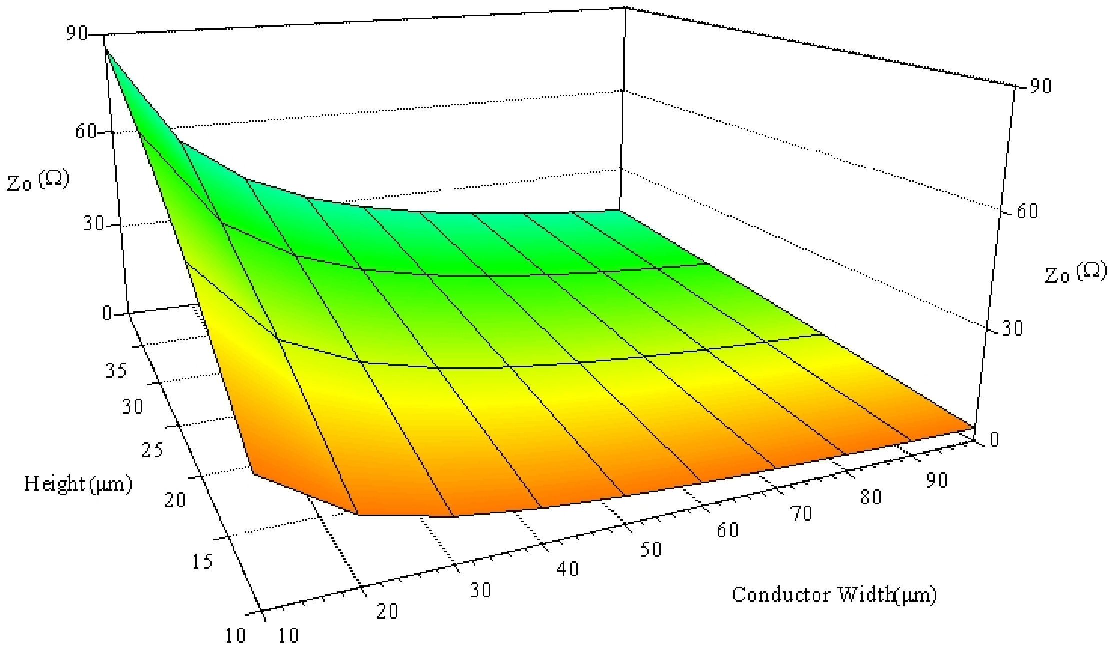

Figure 2.15 Variation of Z_0 with Conductor Width and Height of an All-Polyimide Micro Coax Line

2.6.6 Fabrication of All-Polyimide Micro Coax Lines

The fabrication of all-polyimide type micro coax lines is simpler than for air core or semi-polyimide lines. The main reason for this is the absence of suspended members (center conductor/top shield) as in the case of air core or the semi-polyimide core. In addition, the process of metallizing the outer shield is done by thermal evaporation instead of electroplating side walls (80 µm width and 20 µm height) and the top shield, which saves multiple process steps.

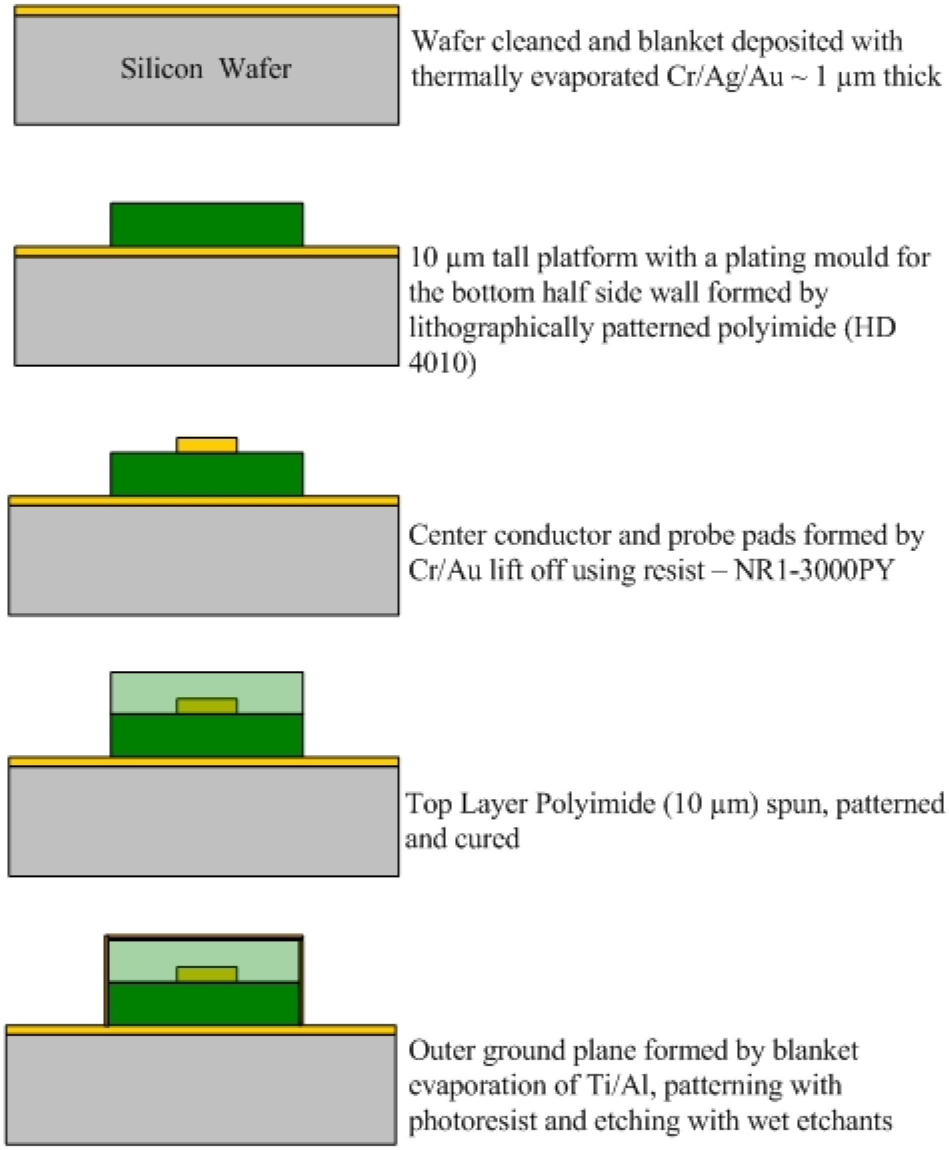

Figure 2.16 Process Flow for All-Polyimide Micro Coax Lines

2.7 Comparison of the Three Generations

In summary, each of the three generations-air core, semi-polyimide core and the all-polyimide core type micro coax lines have their own merits and demerits. The choice of the core type is made depending on the application and one or more of the parameters listed in Table 2.3 below.

Table 2.3 Comparison of the Three Generations of Micro Coax Lines

Core Type	Fabrication	Cond. Width/ Max. Z_o (Ω)	Line Loss (dB/cm) @ 30 GHz	MEMS Device	Vertical Integration	Reliability& Repeatability
air	difficult	40 µm/30	2-5	yes	possible, but difficult	relatively low
semi-polyimide	relatively easy	15 µm/70	3.5-6	yes	possible, but difficult	medium
all-polyimide	very easy	25 µm/25	6-9	no	yes, easy	high

The maximum achievable characteristic impedance (Z_o) is listed for each core is based on a fixed total micro coax height of 20 µm and the listed values of conductor widths. Higher impedance lines can be achieved with vertical scaling, but the fabrication process gets more complex with height. The line losses can be decreased multi-fold by using low loss materials in the polyimide core. An alternate approach to improve the line loss is to widen the center conductor and the overall cross-sectional area of the micro coax line, which helps in distributing the current over a larger area, and reducing the current density. The center conductor of an air core micro coax is constructed based on a suspended fixed-fixed beam topology, which makes it readily amenable to the inclusion of an RF MEM device within the core of the micro coax. In the case of a semi-polyimide structure, a MEM device can be accommodated with slight modifications. This has been demonstrated in Chapter 4 by embedding a MEM varactor inside a semi-polyimide micro coax line. Vertical integration is possible with all three types of micro coax designs, but is a lot easier with the solid all-polyimide type due to the rigid upper polyimide layer on which subsequent layers can be stacked. Stacking is relatively difficult from a fabrication standpoint in the air and semi-polyimide core type designs due to the need for removal of sacrificial layers from the bottom micro coax structures during the release process. Moreover, limited thermal budgets of common sacrificial layers severely constrain the process steps that can be used in the upper layers of the stack. An all-polyimide design was found to the best in terms of mechanical reliability and repeatability from a fabrication perspective. Moving members like the center conductor and/or the top shield in the air core and semi-polyimide designs are prone to structural defects due to residual and thermal stress induced during the fabrication process.

2.8 Conclusions

The chapter gives a historical perspective of microwave transmission lines beginning from the earliest coaxial cables to the very latest micro coaxial transmission lines for on-wafer applications. The advantages of a coaxial transmission line versus other planar line types were discussed in the context of increasing circuit density. A literature survey was presented to document the theories developed for the analysis of rectangular coaxial lines, followed by a comprehensive background on the present state-of-the-art in on-wafer micro coaxial transmission lines. Design aspects of a micro coax line using analytical equations were explained, which was followed by electromagnetic simulations to realize three generations of micro coax lines based on their core type and process flows used to fabricate them. A summary of the merits and demerits of each type of design have been tabulated including line losses, possibility of integration with a MEMS device and vertical integration aspects.

Chapter 3

Measurement, Modeling and Analysis of Micro Coaxial Lines

3.1 Introduction

All the micro coax lines presented in this chapter were measured in the 1 to 40 GHz frequency range with G-S-G microwave probes and an Anritsu Lightning vector network analyzer. A SOLT (Short-Open-Load-Through) calibration was performed using a standard GGB CS-5 calibration substrate to set the measurement reference plane at the probe tips prior to measurement. In addition to conventional return and insertion loss data, the 'Loss Factor' of the lines was also used to analyze their performance. The concept of *loss factor* is used to quantify radiation and other losses in a symmetric network [25]. The loss factor is calculated from the measured S_{11} and S_{21} data using the expression-Loss Factor = $1-|S_{11}|^2 - |S_{21}|^2$.

3.2 Comparison of Air Core Lines of Different Z_0 Values

The results in this section are from air core structures without the top shield. Defects in fabrication caused the top shields to collapse during the release process. The effect of perforations in the center conductor on the insertion loss and loss factor has been presented. Figure 3.1 and Figure 3.2 show the return and insertion loss of three of the several micro coax designs explored in this research. The data is plotted with respect to 50 Ω reference impedance. The length of all the lines is fixed at 2000 μm. The S_{11} response shown in Figure 3.1 is typical of an unmatched transmission line. Figure 3.2 shows an insertion loss of about 3-9 dB/cm at 20 GHz. The main reasons for the high loss in the micro coax line are the impedance mismatch and narrow conductor widths (~40-100 μm) which cause high current densities, leading to higher losses.

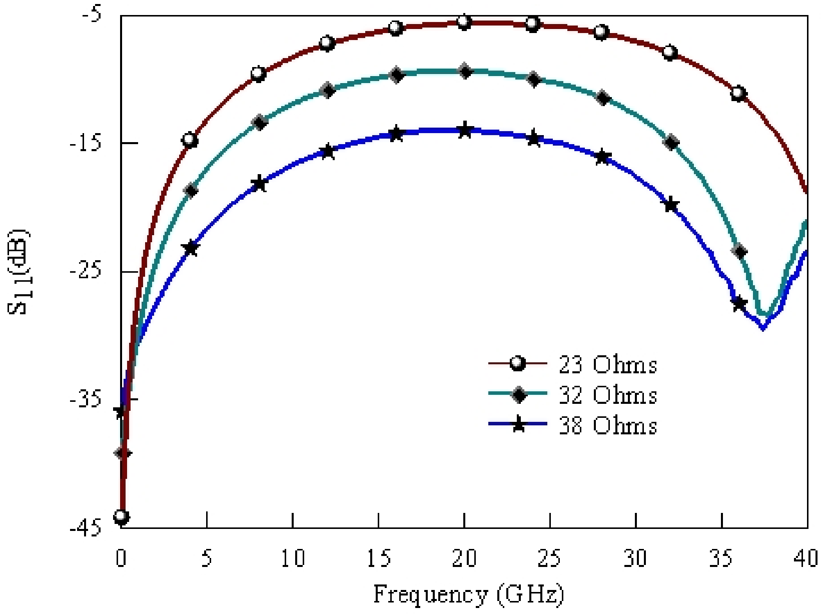

Figure 3.1 Measured S_{11} (dB) of 2000 μm Long Air Core Lines of Different Z_0 Values

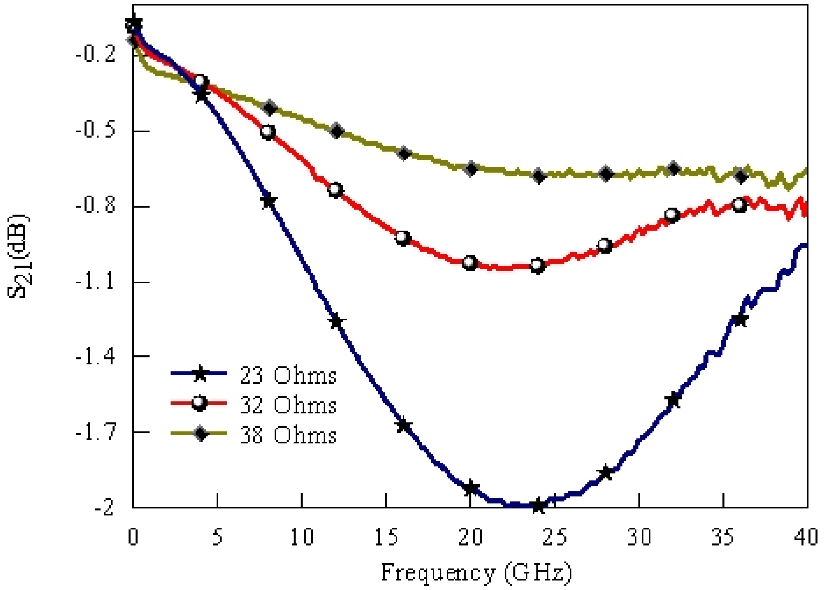

Figure 3.2 Measured S_{21} (dB) of 2000 μm Long Air Core Lines of Different Z_0 Values

Figure 3.3 shows the variation of loss factor with frequency of three of the several designs considered in this research. It can be observed that, the loss factor increases with decreasing conductor width (or increasing Z_0) for in the 1-25 GHz frequency range and decreases with increasing conductor width from 25-40 GHz. This could be attributed to the slight increase in the radiation losses from the bigger holes in the wider conductor to maintain the same porosity at higher frequencies.

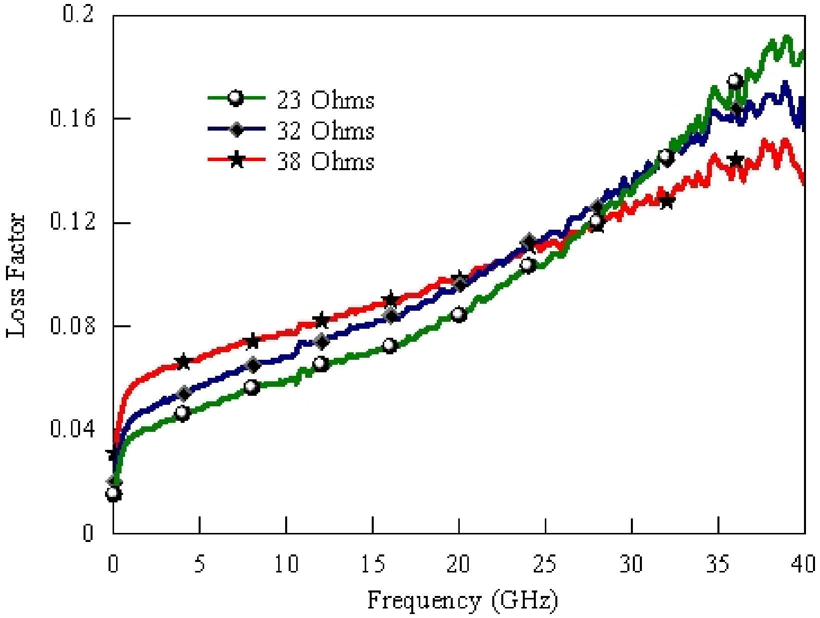

Figure 3.3 Loss Factor of 2000 µm Long Air Core Lines of Different Z_0 Values

The Z_0 can be determined by comparing the S_{21} phase and the return loss of an ideal transmission line with the measured micro coax lines referenced to 50 Ω reference impedance. Agilent ADS software is used tune the values Z_0 of the ideal transmission line to match the S_{21} phase and the return loss of the measured micro coax line. Figure 3.4 shows a comparison of the S_{11} and S_{21} (phase) of a measured micro coax line of conductor width 100 µm after tuning. A Z_0 value of 23 **Ω** was obtained for the measured micro coax line using this method.

An alternative method to calculate Z_0 is to use the design equations ((2.1)-(2.3)) presented in Chapter 2, but the accuracy of the results may be affected by fabrication imperfections. A comparison of the Z_0 values computed using the design equations and from the measured data is tabulated in Table 3.1.

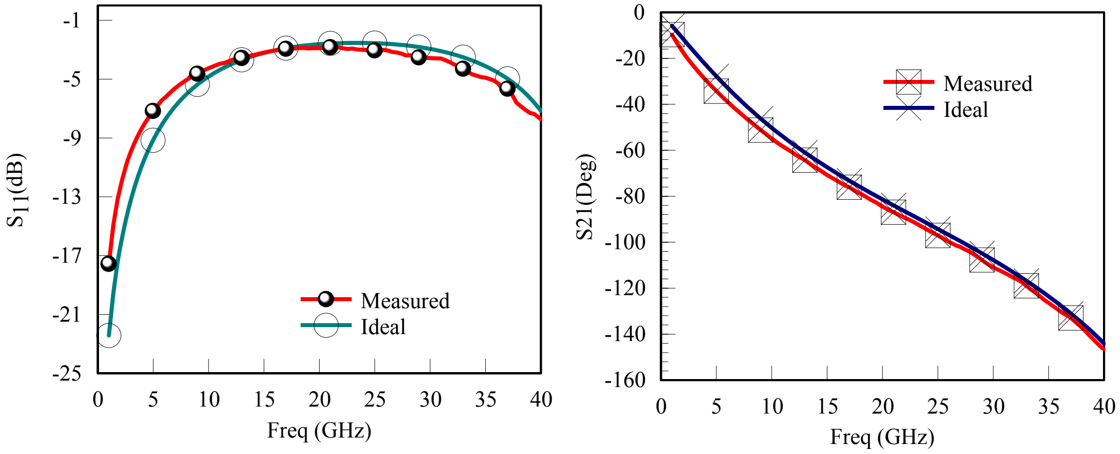

Figure 3.4 Determination of Z_0 from Measured S-parameters

Table 3.1 Calculated and Measured Z_0 Values

Line Width (µm)	40	60	80	100
Calculated Z_0 (Ω)	52	39	31	26
Measured Z_0 (Ω)	52	37-40	27-31	23

3.2.1 Effect of Hole Pattern Variations

Periodic holes are included in the center conductor and the top shield to aid the removal of sacrificial layers and also to control the impedance while the center conductor width is maintained constant. However it may be noted that the top shield was not present in the structures analyzed in this section. The effect of hole pattern variations are analyzed with data from a 32Ω line with hole densities of 0, 13.5 and 16.5% in the conductor and the top shield. Hole density is calculated by taking the ratio of the total area occupied by all the holes to the total area of the conductor. The data is plotted with 50 Ω reference impedance.

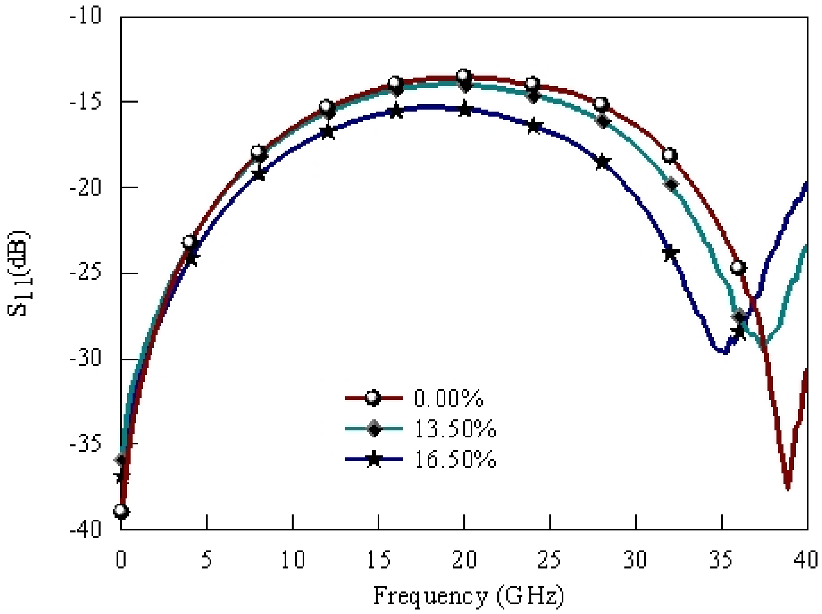

Figure 3.5 Variation of Measured Return Loss with Center Conductor Hole Density

Figure 3.5 shows the variation of return loss of a 32 Ω air core line with varying hole density in the center conductor. It can be observed that the return loss improves marginally with increasing hole density. This is due to the decrease in line capacitance with increasing hole density (as the active capacitance area decreases), which in turn causes a small increase in Z_0 and provides a better match to the 50 Ω reference impedance. It was determined from the measured data that the characteristic impedance increased by about 1 Ω and 3 Ω, respectively, for the 13.5 and 16.5% hole densities relative to the Z_0 based on the design with no holes. Figure 3.6 shows the variation of insertion loss with hole density. The increase in insertion loss between the 0 to 13.5 and 16.5% porosity is very minimal (~ 5% at 20 GHz) because the electrically small holes are located in the center of the conductor and do not disrupt the flow of current, which is usually confined to the edges of a transmission line. A portion of an air core micro coax line with current density contours obtained from electromagnetic simulations shown in Figure 3.7. The contours at both the edges of the conductor represent high current density at the edges which confirms that the current flow in the center conductor is not affected by the porosity in the conductor.

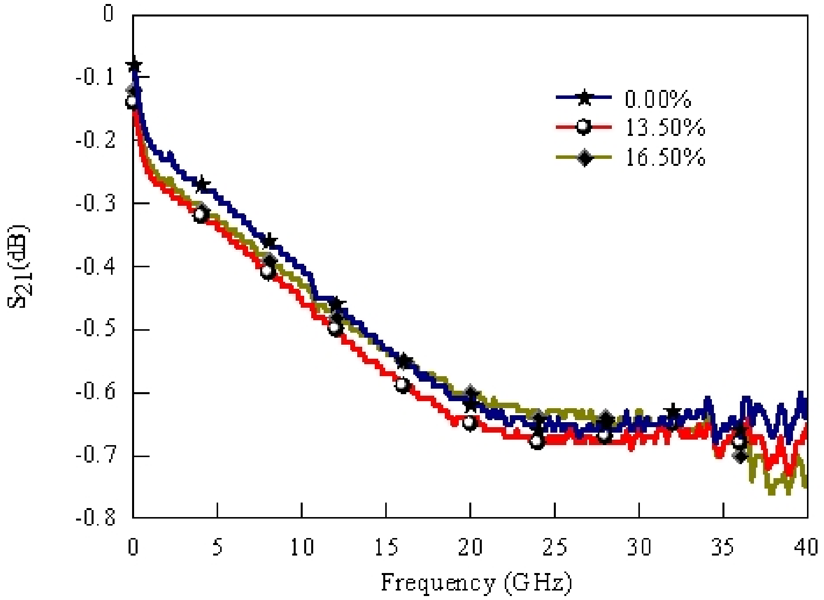

Figure 3.6 Variation of Measured Insertion Loss with Center Conductor Hole Density

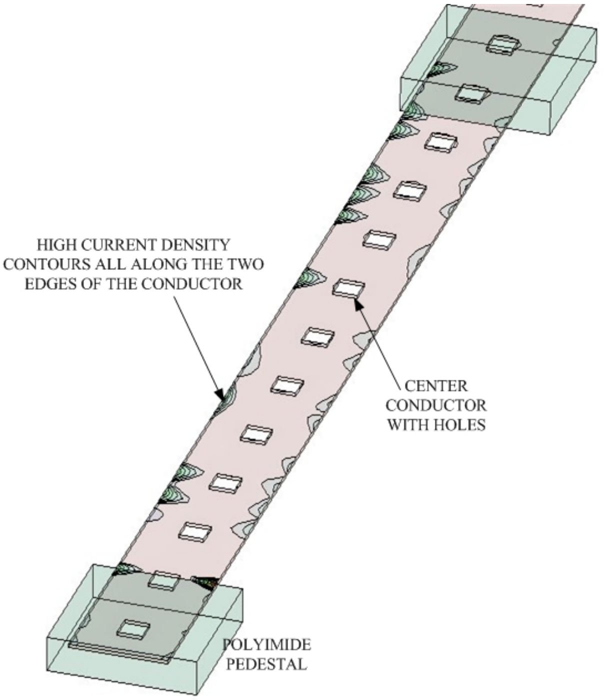

Figure 3.7 Current Density Contours in an Air Core Coax Line

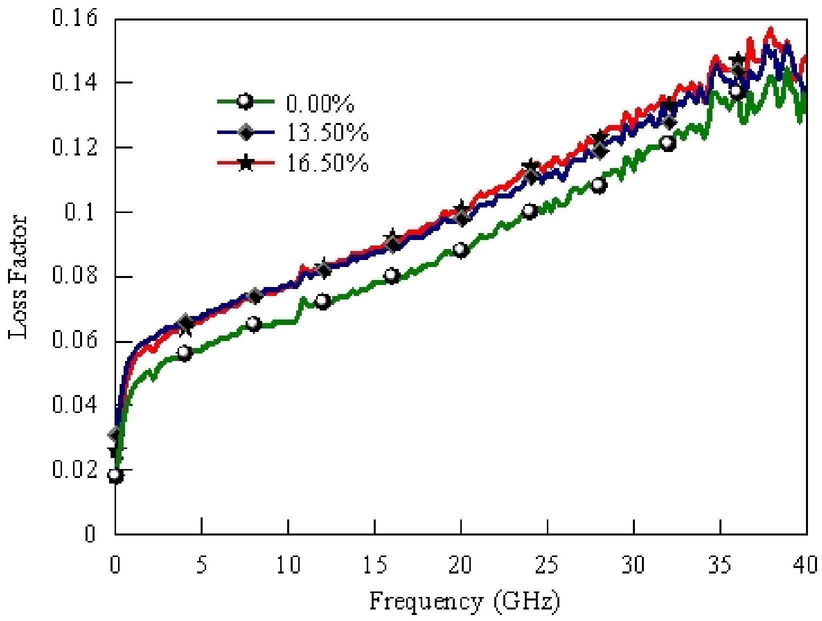

Figure 3.8 Variation of Loss Factor with Center Conductor Hole Density

Figure 3.8 shows the variation of loss factor with hole density. The loss factor increases by about 11% when the hole density increases from 0 to 13.5% and 16.5% when the hole density increases to 16.5% at 20 GHz. This increase in loss factor from the lowest to the highest hole density could be attributed to the increase in radiation losses with the size of the holes which is worsened by the absence of the top shield.

3.3 Equivalent Circuit Modeling of Air Core Lines

A multi-section lumped element equivalent circuit model (see Figure 3.9) of an air core micro coax line was developed using ADS software based on the measured S-parameter data from 1 to 40 GHz. A line length of 2000 μm was considered for the model. The elements were extracted by equating the S-parameters of the model to the measured data using the optimization feature of ADS. A comparison of the measured and modeled S-parameters is shown in Figures 3.10, 3.11 and 3.12 indicate a good fit, which verifies the accuracy of the model.

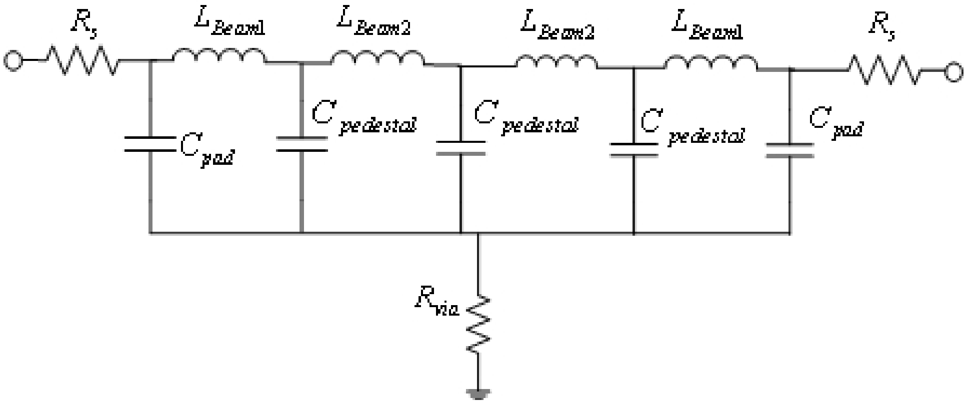

Figure 3.9 Equivalent Circuit Model of an Air Core Micro Coax Line

R_s - series resistance associated with the center conductor

C_{pad} - Capacitance due to the center conductor-probe pads-bottom shield

$C_{pedestal}$ - Capacitance due to the center conductor-polyimide pedestal-bottom shield

L_{beam1} - Inductance of the fixed-fixed beam section including the center conductor extension for probing

L_{beam2} - Inductance of each fixed-fixed beam section

R_{via} - Resistance of the electroplated via to ground

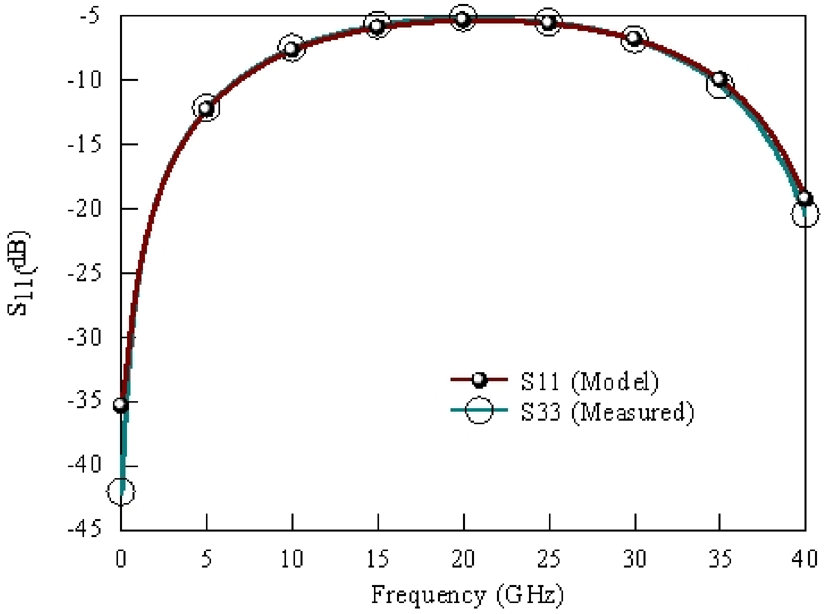

Figure 3.10 Comparison of Measured and Modeled Return Loss

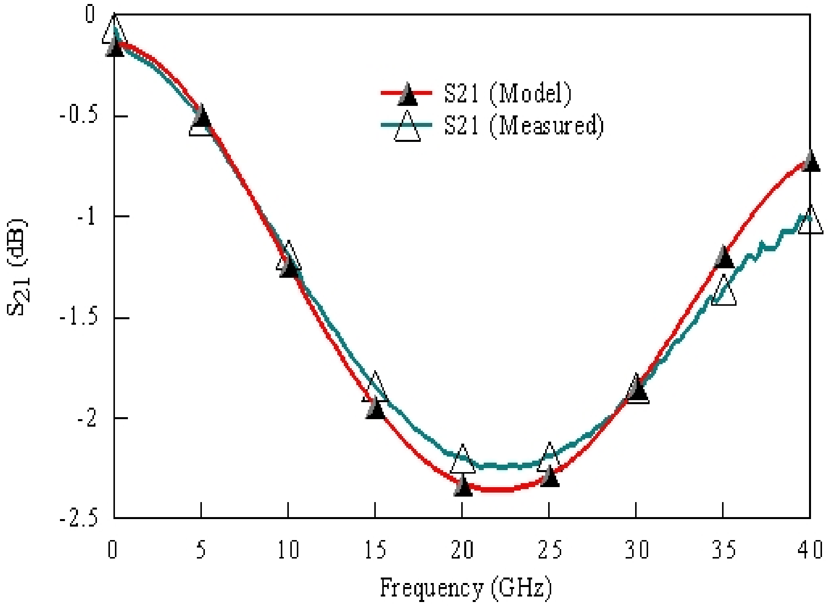

Figure 3.11 Comparison of Measured and Modeled Insertion Loss

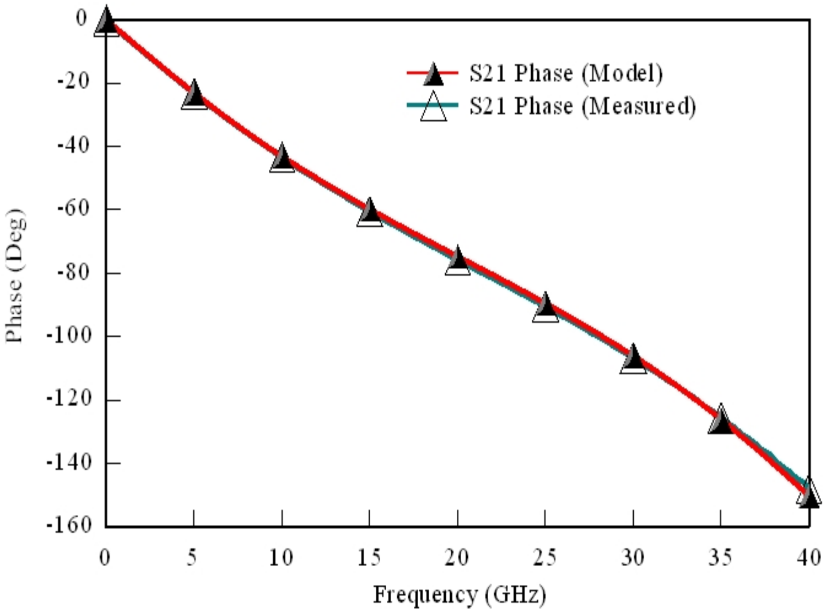

Figure 3.12 Comparison of Measured and Modeled S_{21} Phase

The equivalent circuit element values obtained from the model are given in Table 3.2. The series resistance R_s decreases as the width of the center conductor increases as expected. The value of R_s has a significant effect on the insertion loss. A lower value of series resistance could be achieved by using a thicker metal for the conductor. The beam inductance exhibits a slight variation with Z_0. This could be due to minor deflections in the beam caused due to fabrication imperfections. The values of pad and pedestal capacitance increase as the width of the center conductor increases. The dielectric constant of the polyimide used to form the pedestals extracted from the capacitance values is around 5.3. Though the manufacturer's data sheet quotes a lower dielectric constant value typically measured at lower frequencies (low MHz), it is normal for certain polymers like the HD4010 polyimide used in this research to exhibit a higher dielectric constant and loss tangent at microwave frequencies. The dielectric constant and loss tangent of this polyimide (HD 4010) was extracted by measuring metal-polyimide-metal capacitors in a coplanar waveguide topology. A detailed description of the method and the results of loss tangent and ε_r from 1 to 65 GHz is shown in Appendix B.

The resistance R_{via} refers to the resistance of the electroplated gold via that connects the ground probe pads to the bottom shield. The size of the via is 60×60 μm^2 with a height of 10 μm. The value of R_{via} obtained by modeling is between 1.27-1.39 Ω, which is higher than typical gold plated via resistance of 0.1-0.3 Ω achieved in microwave circuits. The increased via resistance of the air core coax lines can be attributed to the roughness in the electroplated gold, which causes a reduction in contact area with the bottom shield and the ground probe pads. An average value of the polyimide dielectric constant (~ 5.4) can be derived from the extracted capacitance values.

Table 3.2 Equivalent Circuit Values of an Air Core Coax Line

Conductor Width/Z_0	R_s (Ω)	L_{beam1} (nH)	C_{pad} (fF)	L_{beam2} (nH)	$C_{pedestal}$ (fF)	R_{via} (Ω)	Extracted ε_r of polyimide
60 μm / 38 Ω	1.45	0.07	52.86	0.11	43.10	1.27	5.71
80 μm / 32 Ω	0.89	0.06	67.20	0.07	63.20	1.39	5.36
100 μm / 23 Ω	0.86	0.05	88.88	0.07	83.04	1.39	5.16

3.4 Semi Polyimide Lines

The measurement setup and calibration for the semi-polyimide lines is similar to the air core micro coax lines described earlier. Figures 3.13, 3.14 and 3.15 show the S_{11} (dB), S_{21} (dB) and S_{21} (Phase) of 2000 μm long semi-polyimide lines. Measured data shown here has been plotted with respect to the characteristic impedance of the line determined using the techniques described in the previous section about air core lines.

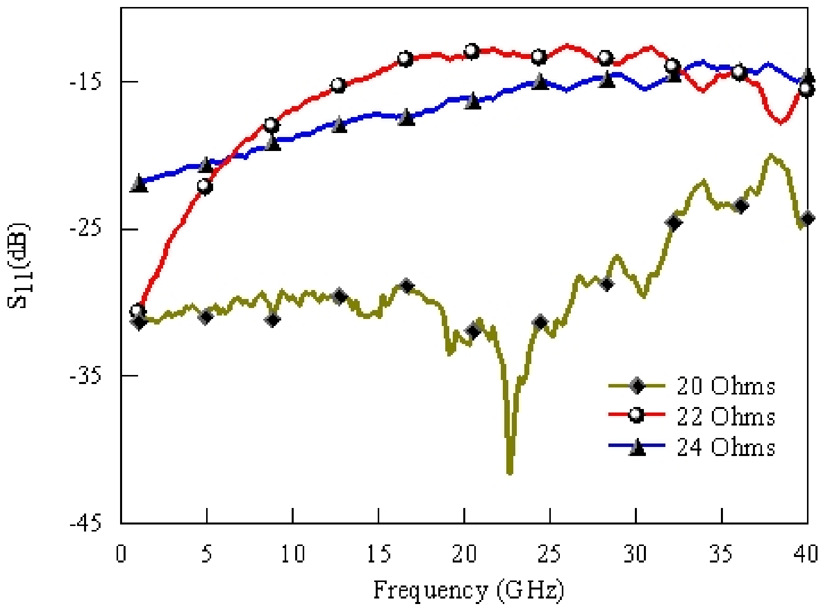

Figure 3.13 S_{11} (in dB) of a 2000 μm Long Semi-Polyimide Line

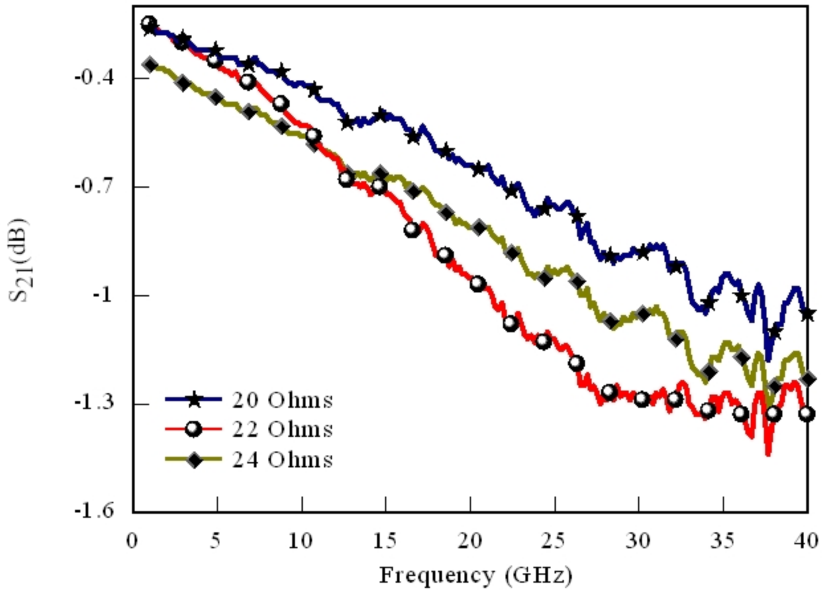

Figure 3.14 S_{21} (in dB) of a 2000 μm Long Semi-Polyimide Line

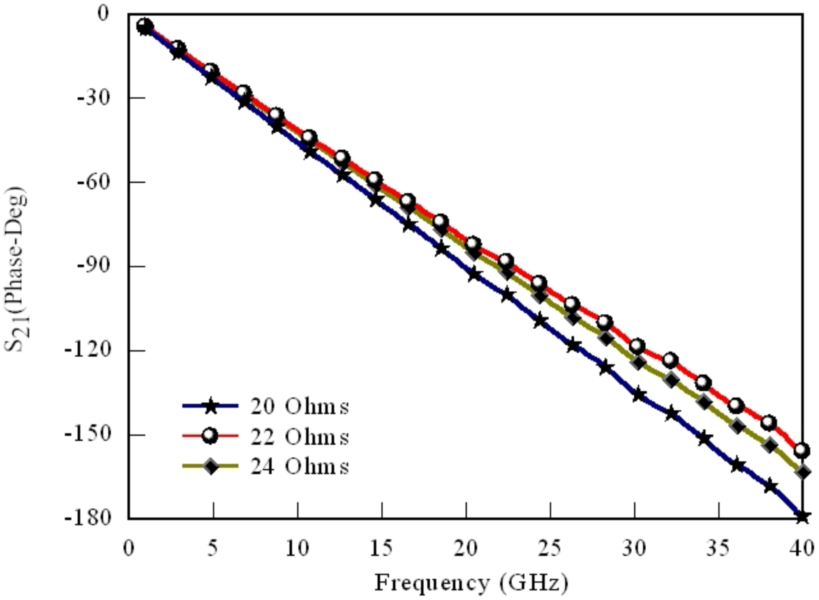

Figure 3.15 S_{21} (phase in deg) of a 2000 µm Long Semi-Polyimide Line

The best case insertion loss of a semi-polyimide core micro coax line is about 4 dB/cm at 20 GHz for a center conductor width of 40 µm. This is about 30% higher than the best air core equivalent. The reason for the higher loss is due to the increased volume of polyimide inside the micro coax cavity as explained in detail in Chapter 2. The Z_0 of the measured semi-polyimide lines is compared with the values obtained from electromagnetic simulations and equations (2.1)-(2.3) (see Table 3.3).

Table 3.3 Comparison of Z_0 Values Obtained from Simulation, Theory and Measured Results

Conductor Width (µm)	HFSS (Ω)	Calculated (Ω)	Measured (Ω)
100	15	16	20
80	16	19	22
60	26	24	24

3.5 All-Polyimide Lines

Ansoft HFSS simulation results for an all-polyimide line with a 25 µm wide center conductor are presented in this section. The effect of bends in a micro coax line was studied by comparing a straight micro coax line with the same length of line meandered to include four bends. The isolation of coax lines has demonstrated by cross-coupling simulations of two all-polyimide micro coax lines spaced 75 µm from each other.

3.5.1 All-Polyimide Lines with Bends

A bend refers to a turn along the path of a transmission line. The performance of planar transmission lines such as the coplanar waveguide and microstrip degrades when a bend is introduced in the transmission line. This is due to the increase in the conductor area at the bend, which causes an increase in line capacitance, leading to a decrease in the line impedance and the electrical length of the line. The effect of bends depends on the width of the conductor and the operating frequency. Several techniques are adopted to counter the effect of a bend in a microstrip or a CPW line [26], [27]. For example, mitered bends are used in microstrip lines to reduce the capacitance while an air bridge is used to equalize the ground potential across the two ground planes in the bent section of a coplanar waveguide line. The excess capacitance caused by this air bridge can be compensated using two high impedance sections at the ends of the air bridge. Micro coax lines on the other hand are known to be unaffected by bends and meanders due to their confined field distribution and a uniform outer shield [21], [22]. This unique characteristic of micro coax lines can be exploited to miniaturize circuits such as couplers which are based on transmission line bends and physical isolation between branches.

Figure 3.16 shows a fabricated 2000 µm long all-polyimide line next to meandered line (with 4 bends) of the same effective length. The simulated S_{21} (dB and Phase) results (referenced to line Z_0 of 25 **Ω**) of the two lines are compared in Figure 3.17. Interestingly the insertion loss of micro coax line with bends is about 16.5% lower than its straight counterpart (of the same overall length) due to the reduction (~6^o) in the electrical length of the meandered line at 30 GHz. This has also been confirmed by a similar analysis by Reid *et al.* [22]. In comparison, a microstrip of the same width on the same 10 µm thick polyimide substrate shows about a 2^o reduction in the electrical length pertaining to an insertion loss improvement of less than 1% at 30 GHz.

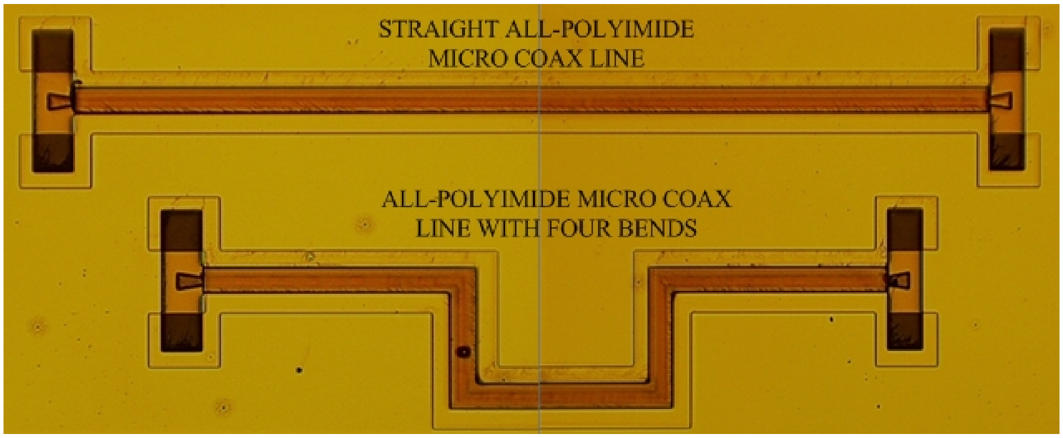

Figure 3.16 Effect of Bends in an All-Polyimide Micro Coax Line

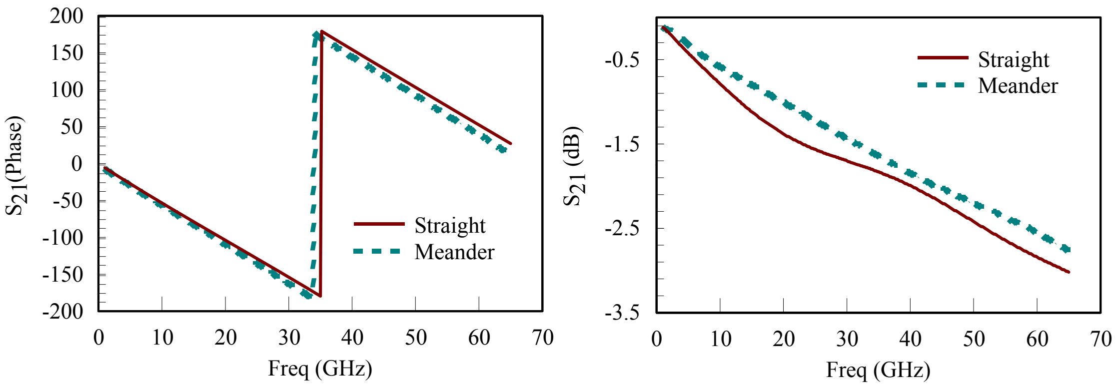

Figure 3.17 S_{21} (Phase and dB) of a Straight and Meandered All-Polyimide Micro Coax Line

The insertion loss of a 2000 µm long straight all-polyimide line is about 1.5 dB at 30 GHz, referenced to its line impedance of 25 Ω, which translates to a loss per unit length of 7.5 dB/cm at 30 GHz. The two main causes for the high loss are the impedance mismatch and the effect of the lossy polyimide (loss tangent ~ 0.08 at 40 GHz) filling the cavity of the micro coax line. Figure 3.18 shows the simulated results of the variation of S_{21} (dB) for a 25 Ω (Z_0), 2000 µm long all-polyimide line. The insertion loss due to a hypothetically lossless polyimide (tan d = 0) is taken as the baseline for comparison with logarithmically increasing loss tangent values from 0 to 0.1. Generally it may be observed that the increase in insertion loss due to an increase in loss tangent is not constant with frequency. For example, the insertion loss at 20 GHz pertaining to a loss tangent of 0 is about 3 dB/cm, which increases to about 6.5 dB/cm for a loss tangent value of 0.1. This difference increases with frequency as seen in the plot. So, it may be concluded that the choice of dielectric material plays a vital role in the performance of an all-polyimide micro coax line. A trade-off has to be made between the simplicity in fabrication versus the loss performance desired.

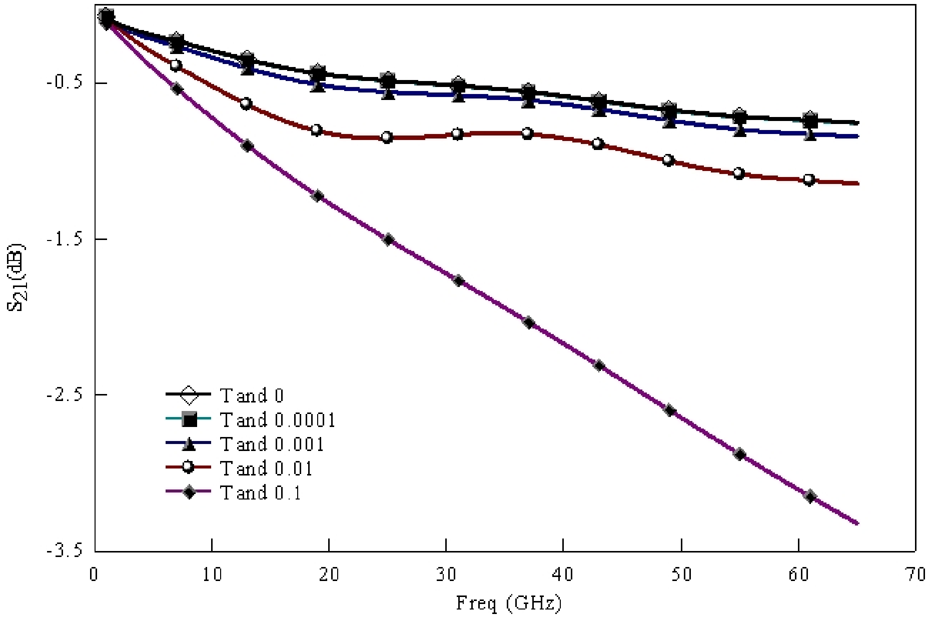

Figure 3.18 Effect of Loss Tangent on the Insertion loss in All-Polyimide Micro Coax Lines

3.5.2 Isolation in All-Polyimide Lines

Line-to-Line coupling is a common problem in closely spaced planar transmission line based circuits especially in lossy substrates such as low resistivity silicon. It has been found that a center-center lateral separation of 600 µm is necessary to achieve a coupling better than -30 dB for frequencies up to 30 GHz [28]. In comparison, micro coax lines on low resistivity silicon exhibit theoretically zero coupling due to their completely shielded nature, which makes them independent of the substrate too. Figure 3.19 shows a microphotograph of two all-polyimide micro coax lines with a 175 µm lateral spacing between the center conductors. The lines are designed in a 4-port configuration to measure the cross-coupling between them. A full 4-port measurement is required to accurately measure the cross-coupling between the two lines. Figure 3.20 shows the Ansoft HFSS simulations of the cross-coupling between two all-polyimide micro coax lines with a lateral spacing of 75 µm between the center conductors of the two lines. Cross-coupling better than 140 dB is observed for frequencies up to 65 GHz. Port numbers used in the plot are indicated in Figure 3.19. This makes micro coax transmission lines the best choice for high density millimeter-wave applications.

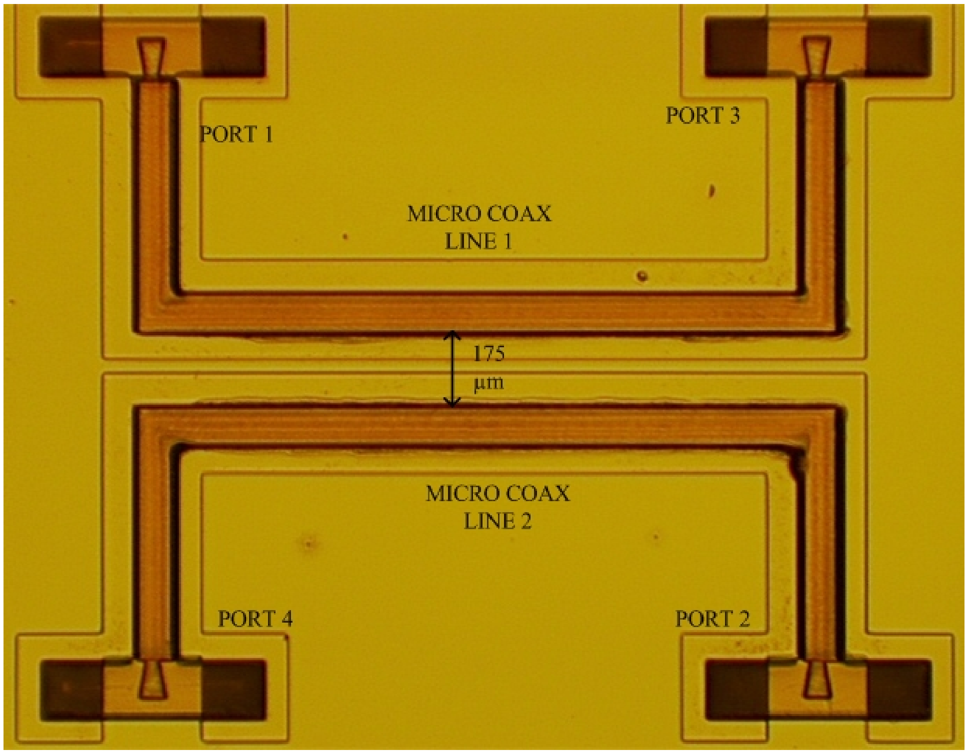

Figure 3.19 Microphotograph of Two All-Polyimide Micro Coax Lines for Cross-Coupling Measurements

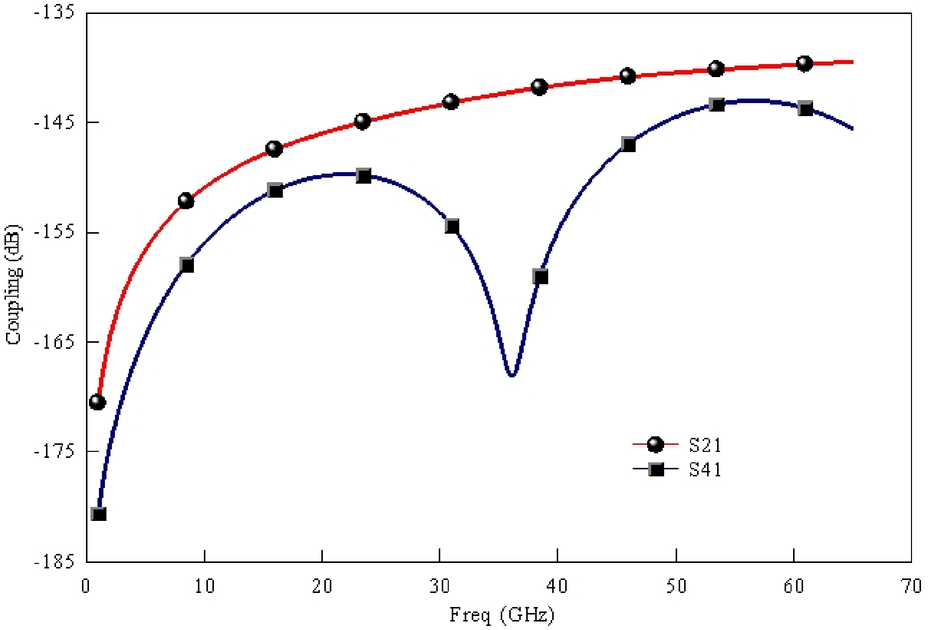

Figure 3.20 Cross-Coupling between Two All-Polyimide Micro Coax Lines

3.6 Conclusions

Results and analysis for the air, semi polyimide and all-polyimide core micro coax lines were presented. The effect of porosity on the center conductor and top ground shield was analyzed for air core micro coax line and concluded that holes do not have a significant effect on the insertion loss. This is very desirable in the context of fabrication, which relies on these holes for the removal of sacrificial layers. An equivalent circuit model was developed to represent an air core micro coax line in its lumped element form. The performance of the semi-polyimide line was studied and compared with the air core lines. All-polyimide micro coax lines were introduced and results of micro coax lines with bends were compared with equivalent lines of the same length to show that presence of bends does not degrade the performance of a micro coax line. The isolation excellent line-to-line isolation characteristics of a micro coax line was demonstrated using HFSS simulations.

Chapter 4

Micro Coax Line with Integrated MEMS Varactor and Capacitive Shunt Switch

4.1 Introduction

The introduction of micro electromechanical systems (MEMS) technology to microwave circuits was pioneered in the latter part of the last century. The application of MEMS technology helps to implement a tunable element to a microwave circuit, typically using a variable capacitor or an inductor, where a suspended structure is actuated using electrostatic, thermal, magnetic or by piezoelectric actuation schemes. Electrostatic actuation is preferred due to its low power consumption and high speed. The suspended member is usually in the form of a fixed-fixed or a cantilever beam supported on pedestals. The tunability, low power consumption (μW), linearity combined with miniature size and the ability to coexist with CMOS circuitry has made MEMS an attractive technology to realize several tunable RF/microwave devices like RF switches, relays, phase shifters, filters etc [29], [30]. From a purely research concept a few years ago, RF MEMS technology has grown out of research labs into companies that commercially produce devices for the mass market today.

The research presented in this chapter aims to integrate the well established RF MEMS varactor technology with micro coax transmission lines to realize a MEM varactor and an RF MEMS shunt switch inside the cavity of a rectangular micro coax line developed in the earlier part of this dissertation. A semi-polyimide type micro coax line was chosen to implement the varactor for 1-40 GHz operation. The RF switch is presently in its fabrication stages and would be implemented in an all-polyimide micro coax line also for 1-40 GHz operation.

4.2 MEMS Varactor Design

One of the most common RF MEMS devices is a variable capacitor or a varactor, which can be configured as a RF switch, phase shifter, filter, impedance tuner etc. Several researchers have proposed RF MEMS variable capacitors in a multitude of configurations to suit various applications. The first parallel-plate MEM capacitor was developed by Young and Boser, achieving a capacitance change of 15% with an array of four fixed-fixed beams and a Q of 60 at 1 GHz [31]. Researchers have also used the standard polysilicon MUMPS process to fabricate variable capacitors and achieve capacitance changes of 0.55 to 1.0 pF and 1.4 to 1.9 pF with actuation voltages in the order of 5V and Q factors around 15-20 at 1 GHz [32], [33]. All the above mentioned MEM capacitors were based on a fixed-fixed beam topology. Cantilever based MEM capacitors have also been developed by several researchers of which a few significant contributions are discussed here. A multi-finger design using cantilevers was proposed by Kannan *et al.* to obtain variable capacitance values as each finger is actuated and increases the contact area. A 10:1 tuning was achieved with an actuation voltage ranging between 30-90V with an unloaded up-state and down-state Q factor of 150 and 90 respectively [34]. A few other types of RF MEMS capacitors include high Q, high tunability and digitally controllable designs [35], [36], [37]. One of the novel RF MEMS capacitor designs includes a hybrid piezoelectric and electrostatic actuation scheme to achieve high speed actuation using a low actuation voltage [38]. All of the above MEMS capacitors were implemented on coplanar waveguide transmission lines.

On the contrary, a semi-polyimide micro coax line developed earlier in this research was considered for embedding the varactor inside its cavity. The semi-polyimide design was chosen to simplify the fabrication and to have a mechanically stable center conductor. In principle, the air core design would have been the easiest to configure a MEMS device within the micro coax cavity due to its inherent fixed-fixed beam structure, but planarity issues with thick (10 μm) sacrificial layers make fabrication difficult. Figure 4.1 shows a three dimensional and top view of a MEM capacitor embedded in a micro coax line. The variable capacitor is formed by an electrostatically actuated fixed-fixed beam. The beam by itself is a part of the center conductor supported on the polyimide platform. A portion of the polyimide is etched using reactive ion etching to form a trench which provides the mechanical isolation for the beam. The depth of the trench is 1.5 μm, while the length depends on the desired length of the beam. When actuated, the suspended portion is designed to make contact with a silicon nitride-topped gold pedestal formed by electroplating from the bottom ground shield. The height of the pedestal and etch depth of the polyimide below the designated beam length define the mechanical isolation for the MEM device. A variable capacitance is achieved when the beam is electrostatically actuated by applying voltages of opposite polarity to the ground plane and the center conductor. The non-actuated state of the beam is referred to as the ‘up-state’ and actuated state as the ‘down-state’ in the context of

RF MEMS devices. The ratio of capacitance between the up and down state is called the ‘Capacitance Ratio’.

The center conductor being supported on the polyimide platform forms a fixed-fixed beam in the suspended region. The total length, width and height of the structures are maintained constant at 2100, 470 and 20 µm across different characteristic impedance designs. The length of the MEM beam was varied as 300, 400 and 500 µm keeping the width constant to study the actuation voltage requirements, sag and other aspects affecting the performance of the device.

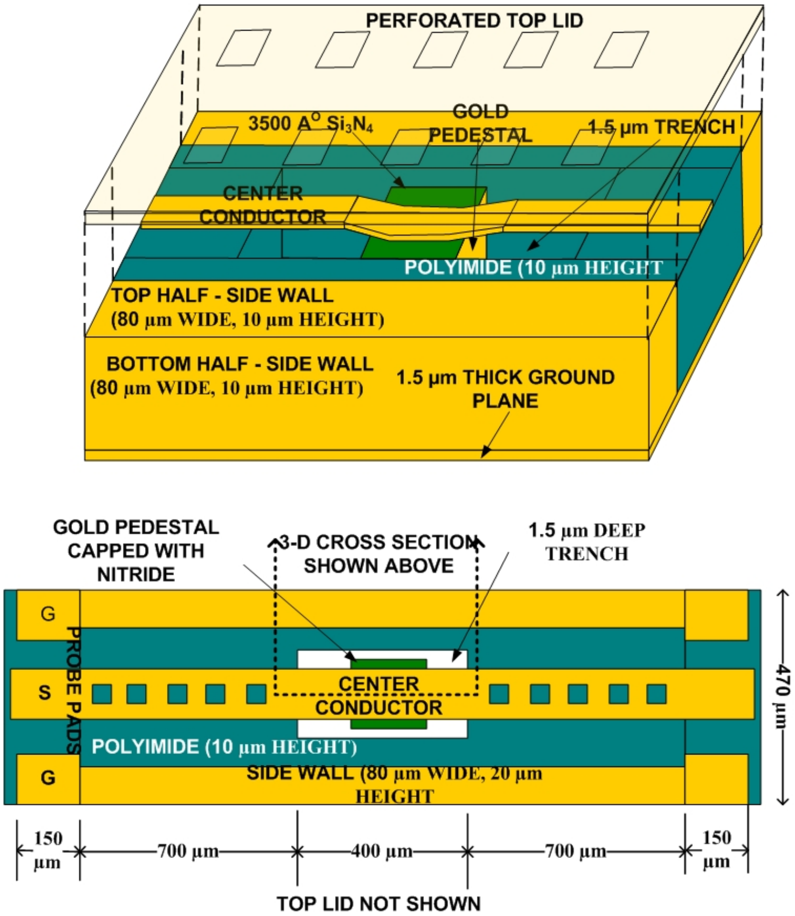

Figure 4.1 Schematic of a MEM Varactor Embedded Micro Coax

Mechanical design aspects and fabrication constraints restricted the minimum width of the center conductor (also the MEM beam) to 60 µm and the polyimide platform thickness to 10 µm, which means that the maximum attainable characteristic impedance (Zo) would be 24 Ω with this design. This is in line with the other semi-polyimide designs discussed in Chapter 2. Higher impedance designs can be realized by using a thicker polyimide layer, which would require chemical mechanical polishing after each lithography and deposition step due to the non-uniformities caused by thick layers of polyimide and photoresist. In order to avoid these problems and keep the fabrication as simple as possible, it was decided to restrict the total vertical height of the devices to 20 µm.

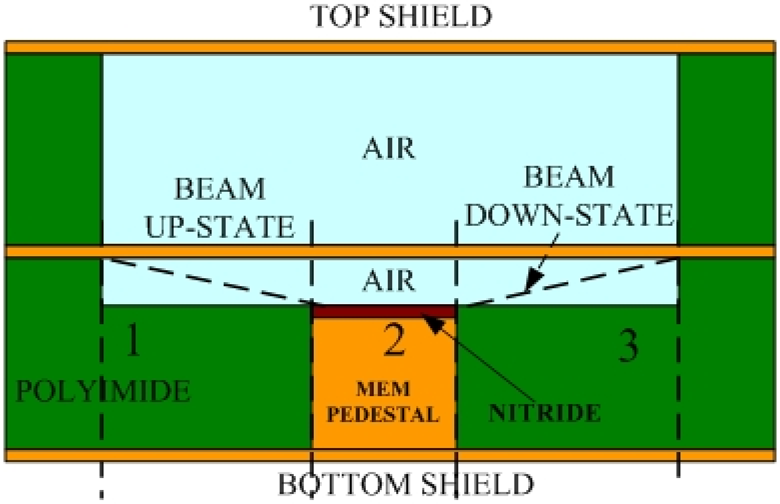

Figure 4.2 Cross-section of a Varactor Embedded in a Micro Coax Line

Standard capacitance and pull in voltage equations [39] were used to predict the capacitance ratio and the voltage required for electrostatic actuation. A cross-sectional view of the variable capacitor portion of a micro coax line is shown in Figure 4.2. The beam is a part of the center conductor of the micro coax line. In the up-state, the capacitance of sections 1 and 3 is calculated based on a composite air and polyimide dielectric. While the thickness of the polyimide is fixed as 10 µm, the air layer can vary in thickness depending on the capacitance ratio required and actuation voltage limits. Capacitance of section 2 is calculated based on a composite air and silicon nitride dielectric. The up-state capacitance is also significantly affected by fringing fields, which increases the overall up state capacitance by 20-40%. A method for determination of the fringing field capacitance is explained in the following section.

Capacitance calculation in the down state is based on the polyimide only for sections 1 and 3 and nitride only for section 2. Fringing effects are negligible in the down state and can be ignored. However, the total down-state capacitance is affected by the deformation of the MEM beam with voltage. The voltage applied across the beam and the gold pedestal pulls down the beam at a voltage called the ‘pull-in’ voltage. At this point, the contact area is equal to the actuation area (neglecting metal roughness, which reduces contact area). As the actuation voltage is further increased, the entire length of the beam starts to deform and bend towards the polyimide. So, the contact area of the MEM beam with the polyimide below cannot be predicted accurately. This could cause a slight increase in the capacitance (from sections 1 and 3) with increasing actuation voltage. In addition the entire length of the beam forms a capacitance with the top metallic shield and the air dielectric in between them, which gets added to both the up and down state capacitances.

Calculation of Capacitance Ratio and Actuation Voltage

Total up-state Capacitance, $C_{UP} = C1_{UP} + C2_{UP} + C3_{UP} + C_{TOP} + C_{ff}$ (4.1)

$$C1_{UP} = \frac{A_{beam} \times \varepsilon_o}{T_{air} + \dfrac{T_{poly}}{\varepsilon_{poly}}} = C3_{UP} \text{ (due to symmetry)} \tag{4.2}$$

$$C2_{UP} = \frac{A_{actuation} \times \varepsilon_o}{T_{air} + \dfrac{T_{nitride}}{\varepsilon_{nitride}}} \tag{4.3}$$

A method to calculate the fringing field capacitance-‘C_{ff}’ is explained in the following section

Total Down-state Capacitance, $C_{DN} = Cbeam_{DN} + Cpoly_{DN} + C_{TOP}$ (4.4)

$$Cbeam_{DN} = \frac{A_{actuation} \times \varepsilon_o \times \varepsilon_{nitride}}{T_{nitride}} \tag{4.5}$$

$$Cpoly_{DN} = \frac{A_{beam} \times \varepsilon_o \times \varepsilon_{poly}}{T_{poly}} \times CF \tag{4.6}$$

‘CF’ refers to ‘Contact Factor’, which is a ratio of the total beam length to the length of the beam in contact with the polyimide (on both sides of the pedestal) due to excessive actuation voltage. Since the varactor is designed for analog capacitance tuning, increase in actuation voltage can be used to achieve higher down-state capacitance by increasing the contact area. However the capacitance contributed by the 10 µm thick polyimide is minuscule relative to the down-state capacitance of the beam due to the nitride dielectric. The capacitance ratio is calculated using the following equation –

Capacitance Ratio-$C_{RATIO} = \dfrac{C_{DN}}{C_{UP}}$ (4.7)

The actuation voltage of a fixed-fixed beam is a function of the beam width, length, material of the beam, mechanical isolation and Young’s modulus of the beam material as shown in the equations below [39].

$$k = 32 \times E \times W \times \left(\frac{T_{beam}}{L_{beam}} \right)^3 \tag{4.8}$$

$$V_{actuation} = \sqrt{\frac{8 \times k}{27 \times \varepsilon_o \times A_{actuation}} \times d^3} \tag{4.9}$$

$C1_{UP}, C2_{UP}, C3_{UP}$ - Up-state capacitances from sections 1, 2 and 3 respectively

C_{TOP} - Capacitance between the center conductor and the top (F)

C_{ff} - Capacitance due to fringing fields (F)

$Cpoly_{DN}$ - Down State capacitance from sections 1 and 3 (F)

$Cbeam_{DN}$ - Down-state capacitance of the MEM beam (F)

$A_{actuation}$ - Active metal-insulator-metal capacitor area (m^2)

$V_{actuation}$ - MEM Actuation voltage (v)

A_{beam} - Area of the MEM beam excluding the actuation area (m^2)

T_{air} - Vertical gap between the center conductor and the nitride dielectric (m)

T_{poly} - Thickness of the polyimide (m)

$T_{nitride}$ - Thickness of the nitride dielectric (m)

$\varepsilon_{nitride}$ - Dielectric constant of the nitride

ε_{poly} - Dielectric constant of the polyimide

ε_o - Permittivity of free space – 8.8542×10^{-12}

k - Spring Constant of the beam (N.m)

T_{beam} - Thickness of the beam (m)

W - Width of the beam (m)

L_{beam} - Total length of the beam (m)

E - Young's Modulus of the beam material (GPa)

d - Mechanical isolation of the beam (m)

Applying equations (4.1) to (4.7) were used to calculate the capacitance ratio of a MEM varactor with a beam length, width and thickness of 400, 60, 1.5 μm respectively, pedestal length of 150 μm, mechanical isolation of 1.5 μm, nitride dielectric constant and thickness of 6.5 and 0.3 μm respectively to obtain-

$C1_{UP} = C3_{UP} = 37.7\,fF$

$C2_{UP} = 51.5\,ff$

$C_{TOP} = 21.2\,fF$

$C_{UP} = 37.7 + 37.7 + 51.5 + 21.2 = 148.1\,fF$ (Using equation (4.1) and neglecting the effect of fringing fields)

In order to accurately determine the increase in up-state capacitance caused by fringing fields, the capacitance geometry described above was simulated using HFSS, a full wave electromagnetic simulation tool to extract the S-parameters of the device. These S-parameters were used to create a lumped element equivalent circuit model to extract the capacitance (C_{MODEL}) of the MEM beam using the optimization feature in Agilent ADS. The capacitance value determined from this model is a composite value of all the capacitance components specified in (4.1). Therefore the fringing field capacitance can be accurately isolated from the composite capacitance since all the other quantities are known. A value of $C_{MODEL} = 143\,fF$ was obtained for the given varactor. The percentage fringing field capacitance can be calculated as-

$$\%C_{ff} = \frac{C_{MODEL} - C_{UP}}{C_{UP}} \times 100 = \frac{143 - 110.4}{110.4} \times 100 \sim 30\% \tag{4.10}$$

So, the total up-state capacitance for a micro coax embedded varactor with similar dimensions can be predicted with reasonable accuracy by including a 30% fringing field capacitance.

The down state capacitance of the above MEM varactor can be calculated using equations (4.4)-(4.6).

$Cpoly_{DN} = C1_{UP} + C3_{UP} = 75.4$, assuming $CF = 0$ or excessive actuation voltage is not applied.

$Cbeam_{DN} = 1727\,fF$, using equation (4.5)

$C_{TOP}= 21.2\, fF$, approximately equal for the up and down states, the small change in capacitance due to the beam deflection in the down state is too small (~ 3-5 fF) and can be ignored.

So, total down state capacitance and capacitance ratio per equation (4.4) and (4.7) respectively is-

$$C_{DN} = Cbeam_{DN} + Cpoly_{DN} + C_{TOP} = 1727 + 75.4 + 21.2 = 1823.6\, fF$$

$$C_{RATIO} = \frac{C_{DN}}{C_{UP}} = \frac{1823.6}{148.1} = 12.31$$

The required actuation voltage for the capacitor described can be calculated using (4.8) and (4.9). The actuation voltage predicted by equation (4.9) is a very rough estimate of the required voltage. Practical voltage values can be 4-10× that predicted by theoretical equations due to the high stress in the beam metal caused by deposition conditions, which increases the Young's modulus and thereby the spring constant and the actuation voltage as per equation (4.8). In addition, these equations do not take into account the metal and dielectric roughness which can decrease the contact or actuation area between the beam and the dielectric and thereby increase the actuation voltage. Further more, roughness in the dielectric layer can cause a build up of charges on the dielectric surface due to the applied actuation voltage. This phenomenon called 'Dielectric Charging' is an important factor that has a direct effect on the reliability of the MEM device. This causes an effective potential difference reduction between the beam and the pedestal, thereby increasing the required actuation voltage and subsequently shorting the capacitor. The effects caused by charging have been dealt in detail by C. Goldsmith *et al.* [40] and several other researchers. Overall, the prediction of accurate actuation voltage requirement is very complex and depends heavily on fabrication parameters.

4.3 Fabrication

The sequence of steps followed to fabricate the MEM varactor embedded micro coax lines on standard silicon wafers is shown in Figure 4.3. The gold plating of the sidewalls and the MEM pedestals was done using a commercially available gold electroplating solution-TG 25E ready to use, sulfite based electrolyte. Microchem PMGI was used a sacrificial layer for the MEM beam. This polymer was chosen because of its self-planarizing ability when annealed and also its resistance to basic solvents. A standard positive photoresist was used as an imaging layer to pattern PMGI rather than attempting an expensive deep UV lithography recommended for PMGI. The detailed procedure used to pattern the PMGI is given in Appendix A. Figure 4.4 shows images of a MEM beam inside the micro coax cavity and the probe pad transition region at one end of a micro coax line.

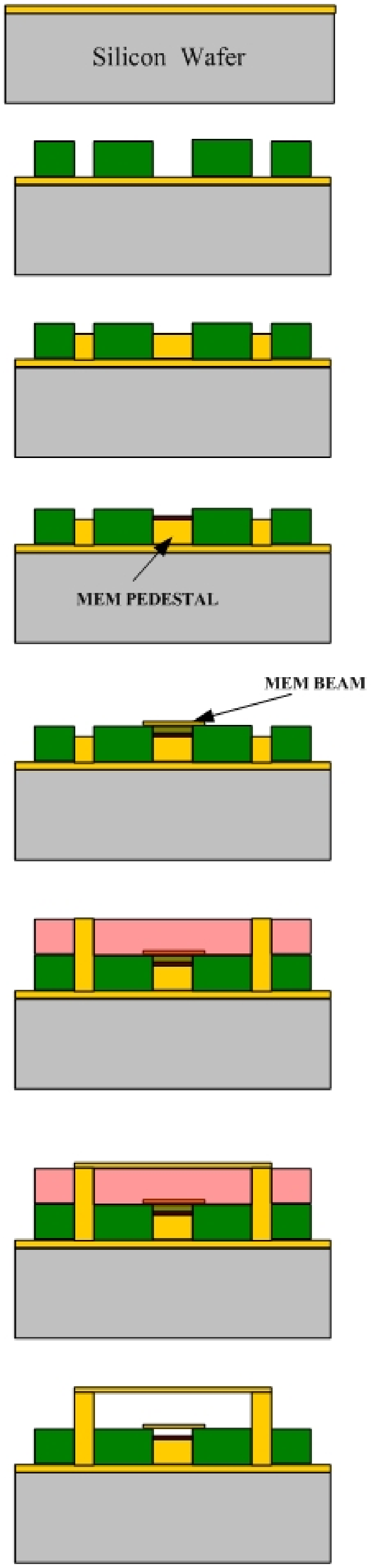

Wafer cleaned and blanket deposited with thermally evaporated Cr/Ag/Au ~ 1 µm thick

10 µm tall platform with a plating mould for the bottom half side wall and MEM pedestal formed by lithographically patterned polyimide (HD 4010)

9 µm tall side wall and MEM pedestal formed by gold electroplating

MEM pedestal coated with 3500 A° silicon nitride by blanket PECVD deposition followed by patterning and RIE etch

Sample spin coated with Microchem PMGI and patterned to fill the 1 µm deep MEM isolation trench. Center conductor patterned on the polyimide platform by thermal evaporation/lithography and wet etching

10 µm thick AZ P4620 spin coated and patterned to form a plating mould for the upper half side wall and sacrificial layer for the top lid

Top ground plane formed on the sacrificial layer by gold electroplating and lithography

MEM beam and top ground plane is released by stripping the sacrificial layers in a two-bath 1165 remover followed by a critical point dry

Figure 4.3 Process Flow for the RF MEMS Varactor Embedded in a Micro Coax Line

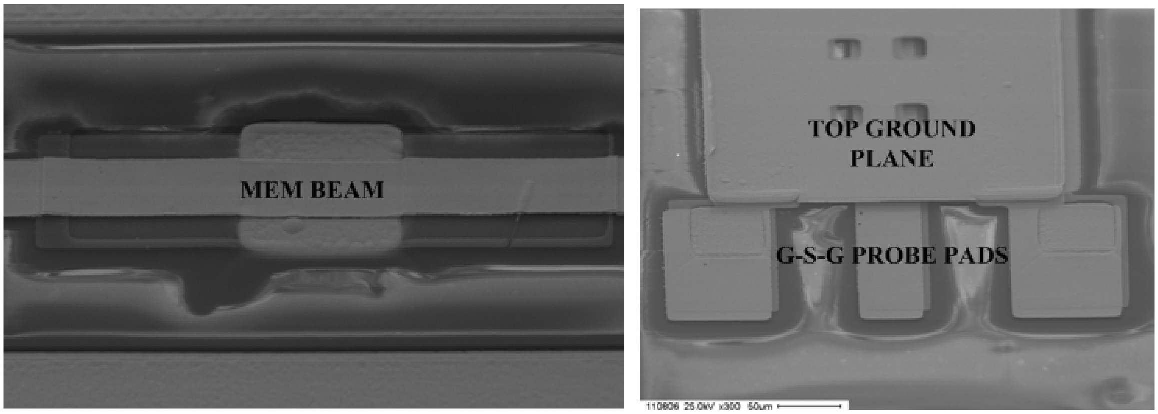

Figure 4.4 SEM Images of the MEM Beam (left) and Probe Pads from a Micro Coax Line (right)

4.4 Results and Analysis

The fabricated structures were measured using an Anritsu Lightning vector network analyzer. A probe tip TRL calibration was performed to set the measurement reference plane at the outer edge of the center conductor (at the probe tips) before measurements. The MEM structures were biased using a superimposed RF+DC signal from a Keithley 4200 Source meter connected to bias tees at the VNA test ports.

Several designs based on the characteristic impedance of the micro coax line and different MEM beam lengths with a capacitance tuning range of 1.2 to 7 were measured. The actuation voltage required for the varactors ranged between 40—60V. Results for a MEM varactor with a 400 µm long and 40 µm wide beam, $80 \times 40\ \mu m^2$ actuation area and embedded in a 30 Ω micro coax line are presented below. The S-parameter results are presented with respect to a 50 Ω system.

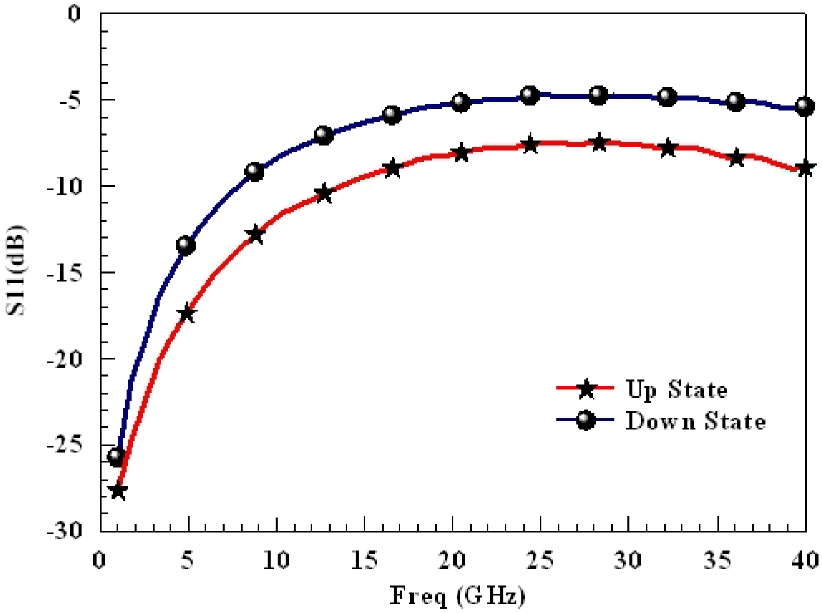

Figure 4.5 Measured Return Loss of a 30 Ω Micro Coax Line with an Embedded MEM Varactor

Figure 4.5 shows the return loss of the entire micro coax line with the embedded MEM varactor in the up and down state. The center conductor of the micro coax line is 40 µm wide 2000 µm long. The MEM varactor is implemented using a 400 µm long fixed-fixed beam suspended above a 150 × 50 µm gold pedestal capped with a 0.3 µm thick silicon nitride dielectric film. The beam as such, is a part of the center conductor (see Figure 4.1). The mechanical isolation was set at 1.5 µm to achieve a capacitance ratio close to 12. An electrostatic actuation scheme was used with actuation voltages in the range of 40 to 60V. Figure 4.6 shows the insertion loss of device in the up and down state of the MEM varactor. A comparison of the up and down state phase of the device (Figure 4.7) with ideal capacitors indicates that the capacitance ratio between the up and down states is close to 6, which is 50% of the theoretically calculated value of 12. However, this result compares well with previously published fixed-fixed beam based RF MEMS varactors in terms of achieved capacitance ratio [31], [32], [33].

One of the main reasons for a reduced capacitance ratio is the reduction in contact area of the MEM beam with the dielectric due to roughness in the dielectric and/or the beam metal which leads to a considerable decrease in the down state capacitance thereby affecting the capacitance ratio. It has been found a surface roughness of 500Å causes a 30-35% reduction in capacitance [39]. Further more, the capacitance ratio is also affected by the increase in up-state capacitance due to sagging of the MEM beam or the top lid due to residual stress. The thickness variations in the polyimide and the dielectric isolation layer also causes a variation in the up-state capacitance, which in turn affects the capacitance ratio as illustrated in the later part of this Chapter.

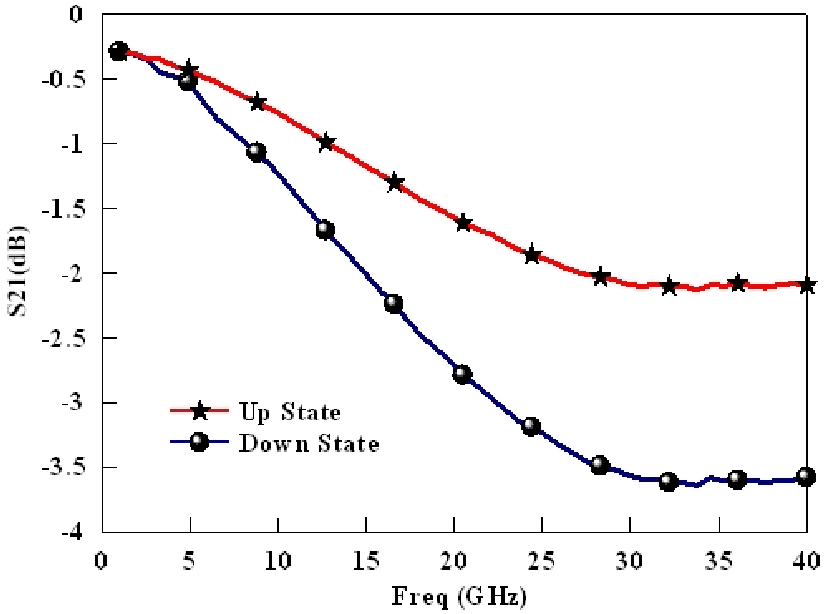

Figure 4.6 Measured Insertion Loss of a 30 Ω Micro Coax Line with an Embedded MEM Varactor

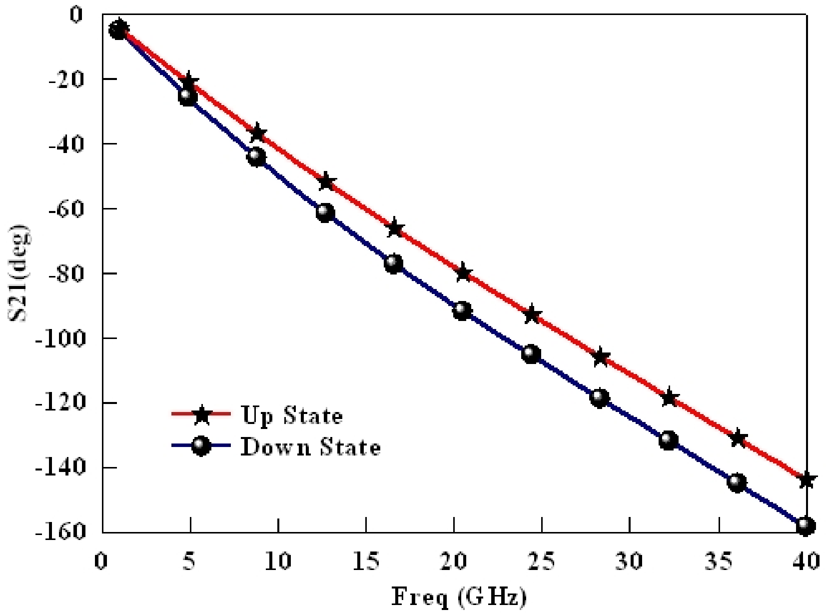

Figure 4.7 Measured S_{21} Phase of a 30 Ω Micro Coax Line with an Embedded MEM Varactor

The unloaded Q of the micro coax embedded varactor can be estimated from the equivalent circuit model or from the measured S-parameters using the equations [39] given below

$$Q_{MODEL} = \omega \times C \times R_P \text{, for a parallel model} \tag{4.10}$$

$$Q_{MEAS} = \frac{2 \times \left\|[\mathrm{Im}(S_{11})]\right\|}{1 - |S_{11}|^2} \text{, based on measurements} \tag{4.11}$$

$\omega = 2 \times \pi \times freq$ (Hz)

C = Capacitance in Farads

Figure 4.8 shows the unloaded Q extracted from S-parameter measurements of a MEM varactor embedded micro coax line using equation (4.10). A Q of 20 and 14 are obtained in the up and down state, respectively, at 10 GHz. The uncertainty in the Q observed at lower frequencies is due to the high sensitivity of the Q to a minute change in the $|S_{11}|^2$ in the denominator of (4.11). Even a 1/100th dB drift in S_{11} measurements can cause a very large change in the extracted Q factor. This makes the S-parameter method unsuitable for high Q measurements [39].

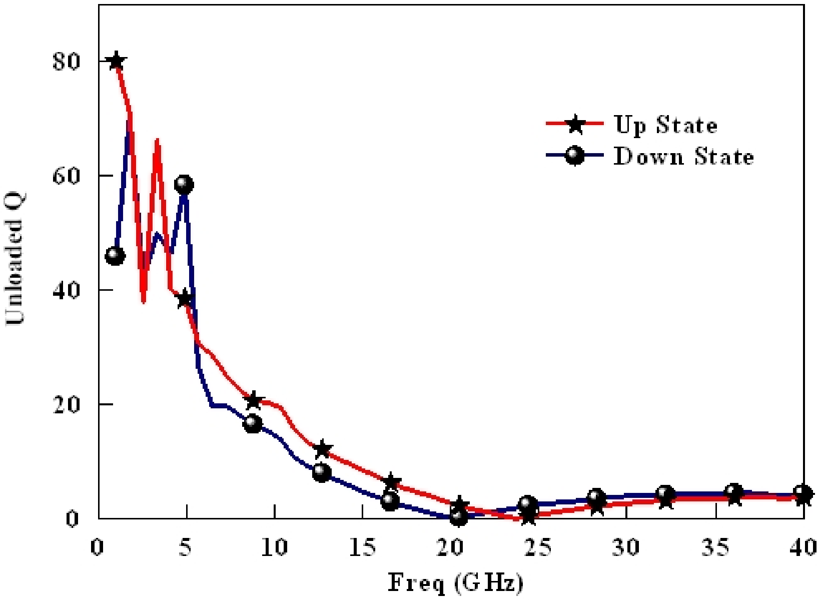

Figure 4.8 Unloaded Q Factor a 30 Ω Micro Coax Line with an Embedded MEM Varactor

4.5 MEMS Varactor Modeling

An equivalent circuit model was created to extract the lumped element equivalent of the MEM varactor embedded in the micro coax line. The length of micro coax line attached to either side of the MEM varactor is divided into five unit cells to improve the accuracy of the model. Each unit cell represents a 140 – 180 µm length of line depending on the total length of 700 – 900 µm long micro coax lines attached on either side. The varactor attached to the MEM beam portion of the model represents the discrete value of the MEM varactor in it's up or down state. The capacitance ratio is based on the capacitance value determined from the model. The model schematic is shown in Figure 4.9.

Each cell called 'TL Cell' is made up of an inductor, capacitor and a frequency dependent effective series resistance (ESR). The ESR (see equation in Figure 4.9) is represented as a 'Z' impedance block, where 'a' is the DC resistance and 'b' a constant determined by optimizing the model parameters to match the measured data. The optimization is performed using the 'Optimization' routine in Agilent Advanced Design System software. Figures 4.10, 4.11 and 4.12 show a comparison of the measured and modeled return, insertion loss and phase for two micro coax MEM varactors embedded in lines of 14 and 24 Ω characteristic impedances (conductor widths of 100 µm and 60 µm, respectively). A good fit observed between the model and measured data verifies the accuracy of the model.

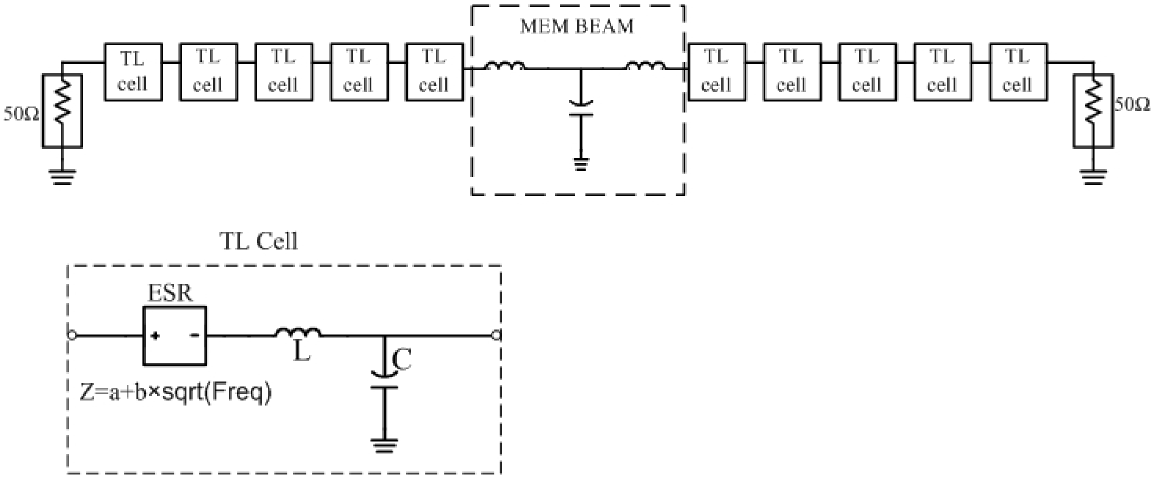

Figure 4.9 Equivalent Circuit Model of a Varactor Embedded Micro Coax Line

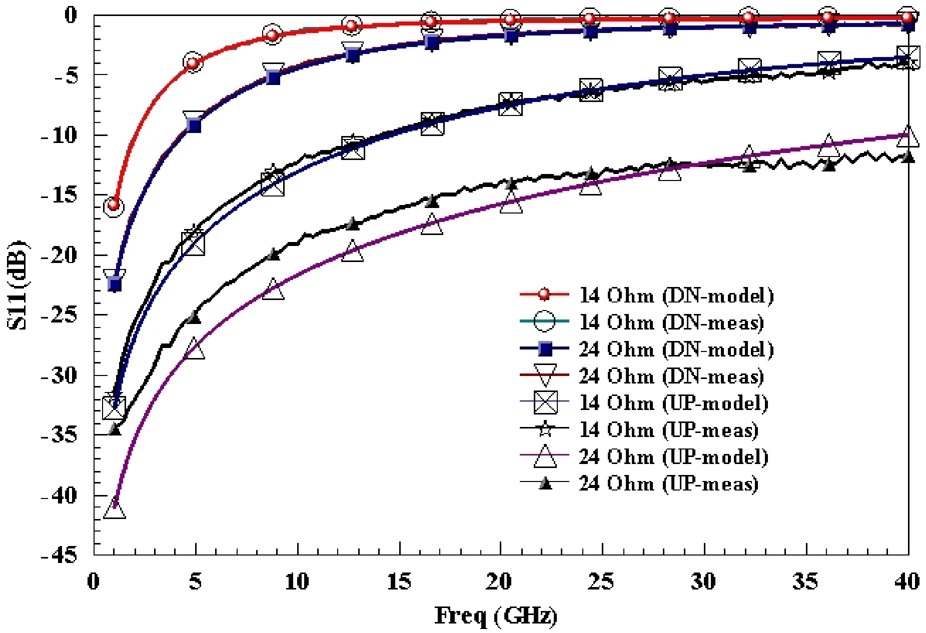

Figure 4.10 Measured and Modeled Return Loss of Micro Coax MEM Varactors

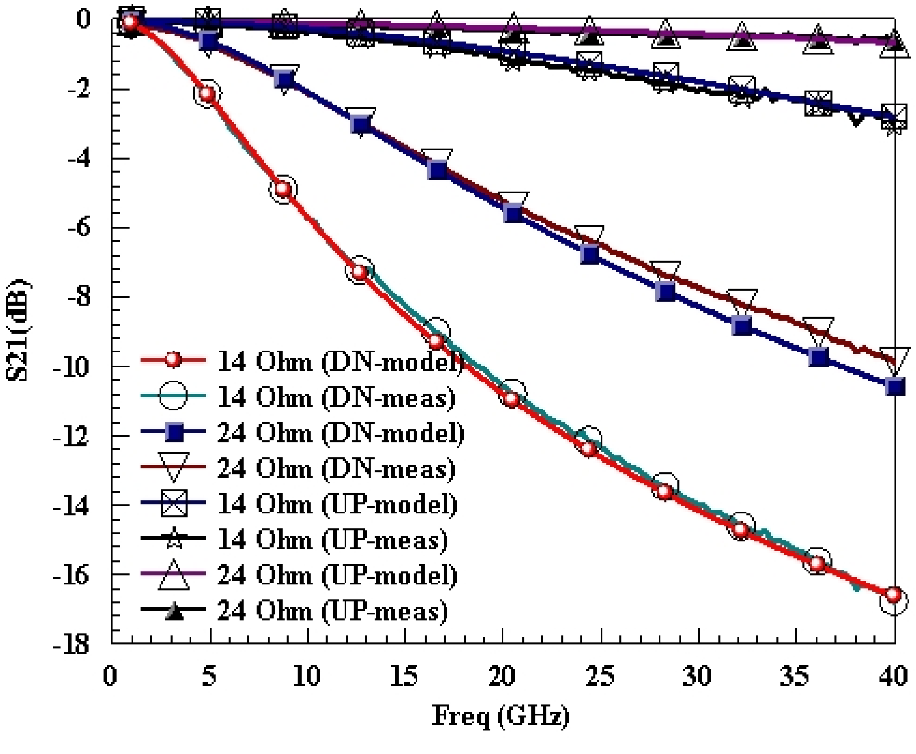

Figure 4.11 Measured and Modeled Insertion Loss of Micro Coax MEM Varactors

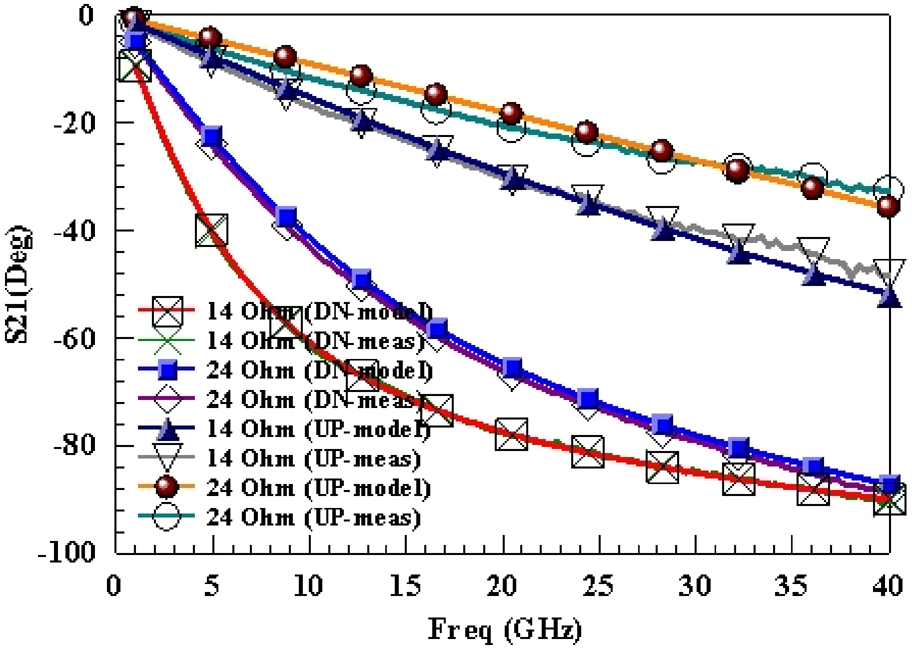

Figure 4.12 Measured and Modeled S_{21} Phase of Two Micro Coax MEM Varactors

The input/output transmission lines connected to the MEM varactor were de-embedded from the composite model of the micro coax feed line embedded with the MEM varactor in order to shift the reference planes to the outer edges of the MEM beam; as such the actuation beam is included with the discrete varactor as part of the overall structure. This was done to extract the lumped element equivalent of the MEM varactor by itself. The equivalent circuit element values obtained from modeling are presented in Table 4.1.

Table 4.1 Equivalent Circuit Element Values

Zo	Area $(\mu m)^2$	Total ESR @ 30 GHz	Cap. (pF)	Total Ind. (nH)	Measured Cap. Ratio	Calculated Cap. Ratio
14 Ω(up)	140 × 100	0.47 Ω	0.16	0.015	6.56	10.85
14 Ω(dn)			1.05	0.014		
24 Ω(dn)	100 × 60	0.82 Ω	0.07	0.026	7.14	12.50
24 Ω(up)			0.50	0.028		

The capacitance ratio values obtained from the model (~ 6.5 and 7) for the 14 Ω and 24 Ω lines, respectively, are in good agreement with the capacitance ratio value of 6 obtained by comparing the phase values from S-parameter measurements to an ideal capacitor response. The slight difference in the inductance values between the up and down states can be attributed to the deflections caused in the beam during actuation. The capacitance ratio/isolation values are about 60% of that predicted by theoretical calculations. The discrepancy is caused due to a decrease in the down state capacitance due to variations in fabrication parameters as explained in the previous section.

4.6 RF MEMS Switches

An RF switch is a device that directs the passage of an RF signal in a circuit and finds wide use in several RF/microwave systems such as transmitter/receivers, antenna arrays, phase shifters, tunable filters etc. Conventionally an RF switch is made of a PIN diode or a FET because of their low voltage operation, high switching speed, reliability and interoperability with other circuitry. The disadvantages of PIN diode or FET switches are high power consumption, non-linear behavior and high signal loss. In 1990-91 Dr. Larry Larson [41] introduced a new type of switch technology to control RF/microwave signals using a movable member integrated with a transmission line to pass or divert the incoming RF signal in a pre-determined direction based on an actuation mechanism to control the switching action. He called it 'micromachined microwave actuator technology', which later on transformed into 'RF Microelectromechanical Systems or RF MEMS'. The micromachined microwave actuator was conceived in an attempt to address the problems of the semiconductor switches mentioned above. True to its claim, the performance of the RF MEMS switch was better than semiconductor switches up to 50 GHz in terms of achieved isolation between the on and off states, very low power consumption in the order of µW, high linearity and very low signal loss (~ 0.2 dB at millimeter-wave frequencies). However it lagged behind semiconductor switches in power handling, reliability, packaging and switching speed. The curiosity and potential in this new technology fueled by the enormous research funding provided by the military in the last 15 years has led to the development of more reliable (>10 billion cycles), high speed switches (~ 250 nS) and packaging schemes for the switches in recent times. In addition to switches, RF MEMS technology has been envisaged to produce tunable inductors, matching networks, resonators etc and is steadily transitioning to a commercially viable solution to actively compete with the semiconductor switches [42], [43]. The latest benchmark in RF MEMS technology is a fully packaged shunt switch with a 0.3 dB insertion loss and isolation better than 54 dB at 20 GHz [44]. Aside from improving on the loss performance, reliability and packaging issues, numerous innovations are also being unveiled every year of which, the latest (as of October 2007) includes a capacitive MEMS switch with a warped beam to enhance its performance by doubling the down state capacitance while halving the up-state capacitance [45]. In summary, several university research groups and companies around the world are trying to exploit the immense market potential for inexpensive, reliable and miniature RF switches.

The two main types of switches used in microwave circuits are shunt and series switches. The choice of switch type depends on implementation and application. A series RF switch passes the RF signals in its on state contrary to a shunt switch, which diverts the signal to the ground in its on state. The shunt and series switches are further classified as DC contact and capacitive contact switches. A metal-to-metal contact allows the RF signal to pass through in its on state and hence the name, DC contact. An RF short is created by forming a capacitive path from the signal conductor to the ground plane in a capacitive contact switch. The value of the capacitance is chosen depending to provide a low impedance path to ground in design frequency band. Switching operation is carried out by a moving member in the switch called the beam. Typically series switches are built with a cantilever beam and shunt switches with a fixed-fixed beam. The movement or ‘actuation’ is by the application of electrostatic, thermal, magnetic or piezoelectric actuation methods, of which the electrostatic method achieves the fastest actuation with the least amount of power. Composite actuation schemes involving a combination of two methods have also been researched. These switches are commonly developed on a CPW platform due to ease of fabrication. Microstrip and waveguide switches have also been developed for specific applications.

The main motivation of this research is to demonstrate the ability of a micro coax transmission line developed earlier to adapt to the RF MEMS switch revolution. A standard capacitive shunt switch using an electroplated gold beam and a silicon nitride dielectric layer was chosen to be embedded inside a micro coax transmission line. The highlight of this implementation would be a fully shielded RF switch amenable to vertical integration. Ansoft HFSS simulations were used to analyze the performance of the switch integrated with the micro coax line in the 1-40 GHz frequency range. The fabrication of the switch is currently in progress. The fabrication sequence and simulation results are presented in the following sections.

4.7 RF MEMS Shunt Switch Design

The main design parameters of a RF shunt capacitive switch are the up-state and down-state capacitance which defines the capacitance ratio, which in turn determines the isolation of the switch in its on state and insertion loss in the off state. Other switch parameters include actuation voltage, switching speed, lifetime, intermodulation distortion and a host of others depending on the application. Figure 4.13 shows the working principle of a MEMS capacitive shunt switch. The illustration on the left (in Figure 4.13) shows the up or off state of the switch where the MEM beam is in its non-actuated state. The vertical distance between the beam and the dielectric layer is called the 'isolation'. The picture on the right in Figure 4.13 shows the down or the on state of the switch where the beam is in contact with the nitride dielectric, when an actuation voltage is applied across the signal line and the ground plane. The width of the beam/center conductor, isolation and the dielectric thickness affect the up and down state capacitance of the switch. Figure 4.14 shows a shunt switch embedded in an all-polyimide type micro coax line. The dimensions of the switch elements are given in Table 4.2.

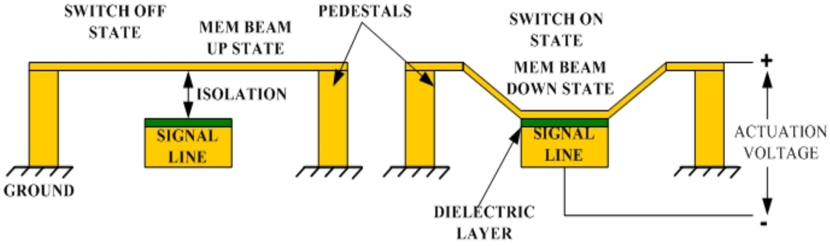

Figure 4.13 Working Principle of an RF MEMS Shunt Capacitive Switch

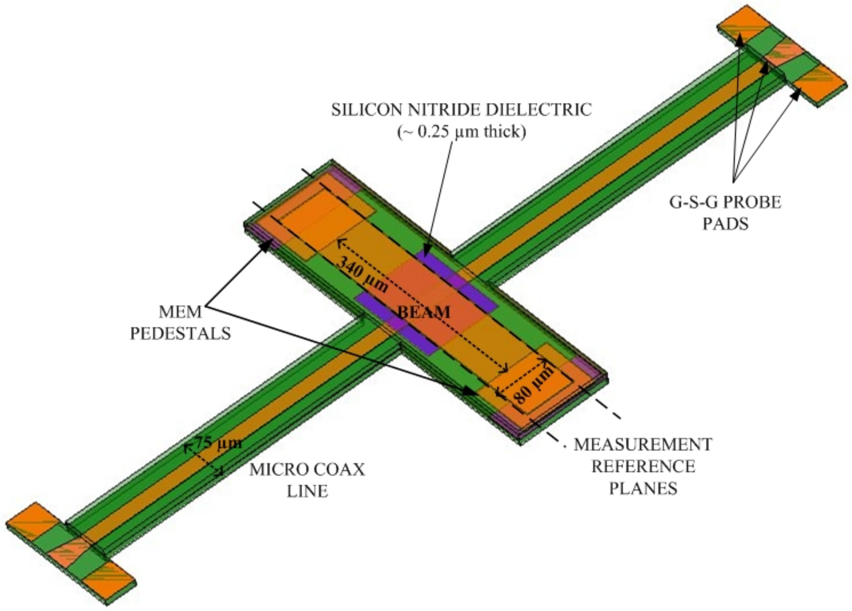

Figure 4.14 RF Shunt Switch Embedded Micro Coax line

Table 4.2 Design Parameters of the Proposed Switch

Parameter	Dimensions
Beam Area	$340 \times 80\ \mu m^2$
Beam Thickness/Metal	1 µm/Electroplated Gold
Beam –Young's Modulus	200 GPa
Actuation Area	$150 \times 80\ \mu m^2$
Silicon Nitride (Dielectric) Thickness	0.25 µm
Isolation	1.5 µm
Pedestal Area	$80 \times 100\ \mu m^2$
Up-state Capacitance	69.6 fF
Down-state Capacitance	2.76 pF
Capacitance Ratio	40
Actuation Voltage	11.07 volts

The up-state, down-state capacitance and capacitance ratio and actuation voltage can be calculated using equations (4.3)-(4.9) given in the earlier part of this chapter. The switch design was simulated as a composite structure (as shown in Figure 4.14) with the micro coax line from 1 to 40 GHz to analyze the insertion loss and isolation using Ansoft HFSS.

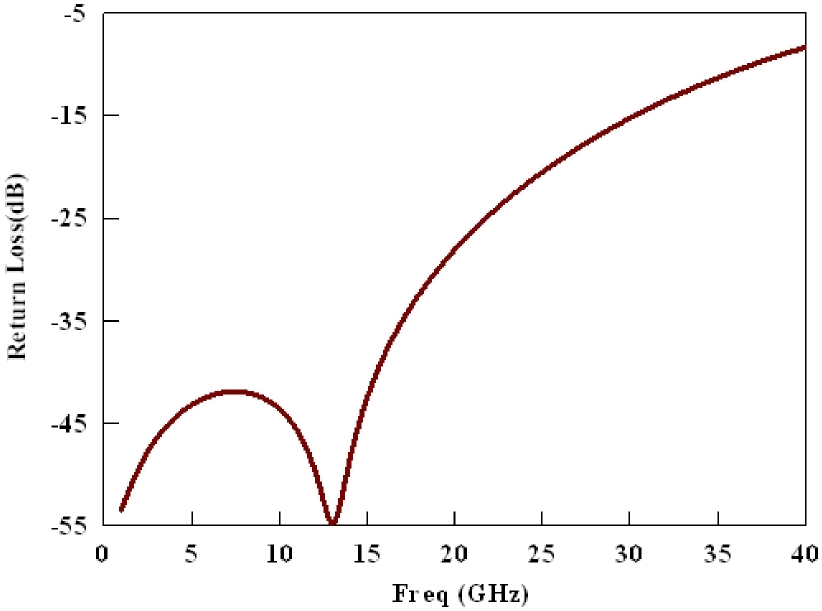

Figure 4.15 Simulated Return Loss of the Proposed Switch in the Up or Off State

Figure 4.15 shows the simulated return loss of the micro coax shunt switch in its off or non-actuated state. The return loss is better than 15 dB up to 30 GHz, which is closely comparable to the response of a near ideal capacitive shunt switch with an up-state capacitance of 70 fF (comparing a calculated value of 69.6 fF shown here) described in the literature [39]

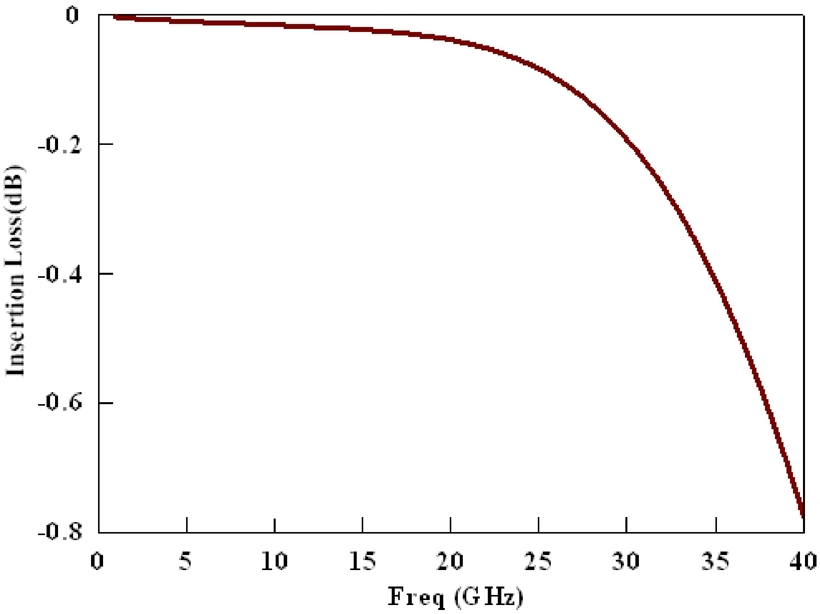

Figure 4.16 Simulated Insertion Loss of the Proposed Switch in the Up or Off State

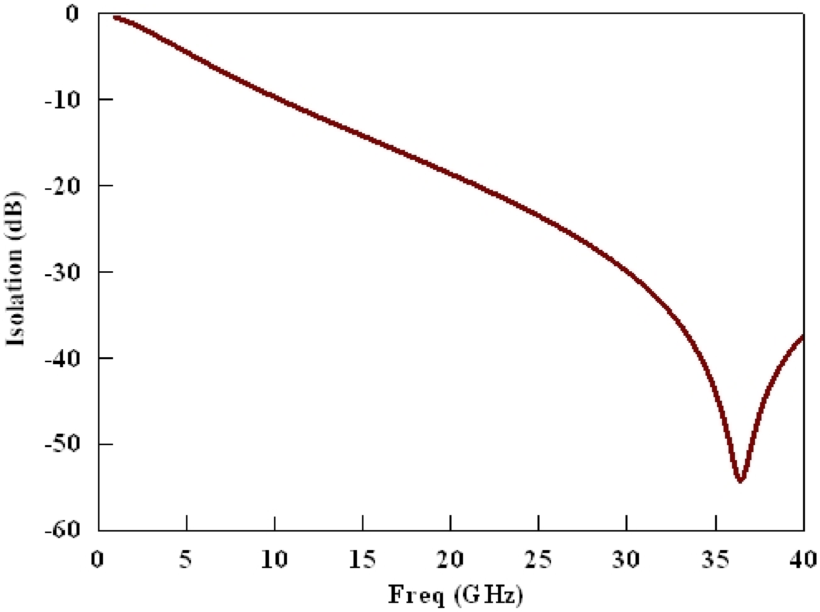

Figure 4.17 Simulated Isolation of the Proposed Switch in the Down or On State

Figure 4.16 shows the simulated insertion loss of the switch in the up-state. The main contributors of up-state loss in a MEMS capacitive shunt switch are transmission line loss beneath the bridge, MEMS bridge loss and the loss of the transmission line included on either side of the switch. In the case of the micro coax polyimide switch, a relatively high insertion loss of around 0.4 dB in the up-state is observed at 30 GHz (see Figure 4.16), when compared with a ideal switch loss of <0.1 dB achievable in RF MEMS shunt switches fabricated on quartz or silicon wafers in a CPW topology. This is primarily because of the high loss (loss tangent of 0.08 at 40 GHz) in the polyimide layer below the conductor compared to quartz or silicon wafers.

The simulated isolation of the switch is shown in Figure 4.17, which shows an isolation of about 35 dB at 30 GHz. This is comparable to the classic MEMS capacitive shunt switches of similar capacitive ratios presented in literature [39]. It has been shown by researchers that the isolation response of a shunt switch is controlled by the capacitance of the beam until $f_o/2$ or 1-20 GHz when a frequency span of 1-40 (f_o) GHz is considered. The inductance of the beam takes starts dominating the response from $f_o/2$ to f_o. The resonant frequency of the switch is also a function of the inductance and capacitance as given by the equation- $f_r = \frac{1}{2\pi\sqrt{LC}}$.

So, it's essential to strike a balance between the capacitance and inductance of the switch to achieve broad band operation and set the resonance of the switch at the desired frequency range [46]. For example, the switch design presented in this work has a good isolation (>20 dB) in the down-state and good return loss (<15 dB) in the up-state between 20-35 GHz.

4.8 Fabrication Process

The fabrication sequence for the proposed RF shunt capacitive switch is shown in Figure 4.18. The MEM beam will me made of electroplated gold – 0.75 to 1.0 µm thick. PMGI will be used as a sacrificial layer to achieve a mechanical isolation of 1.5 µm. The individual process steps are explained in Appendix A.

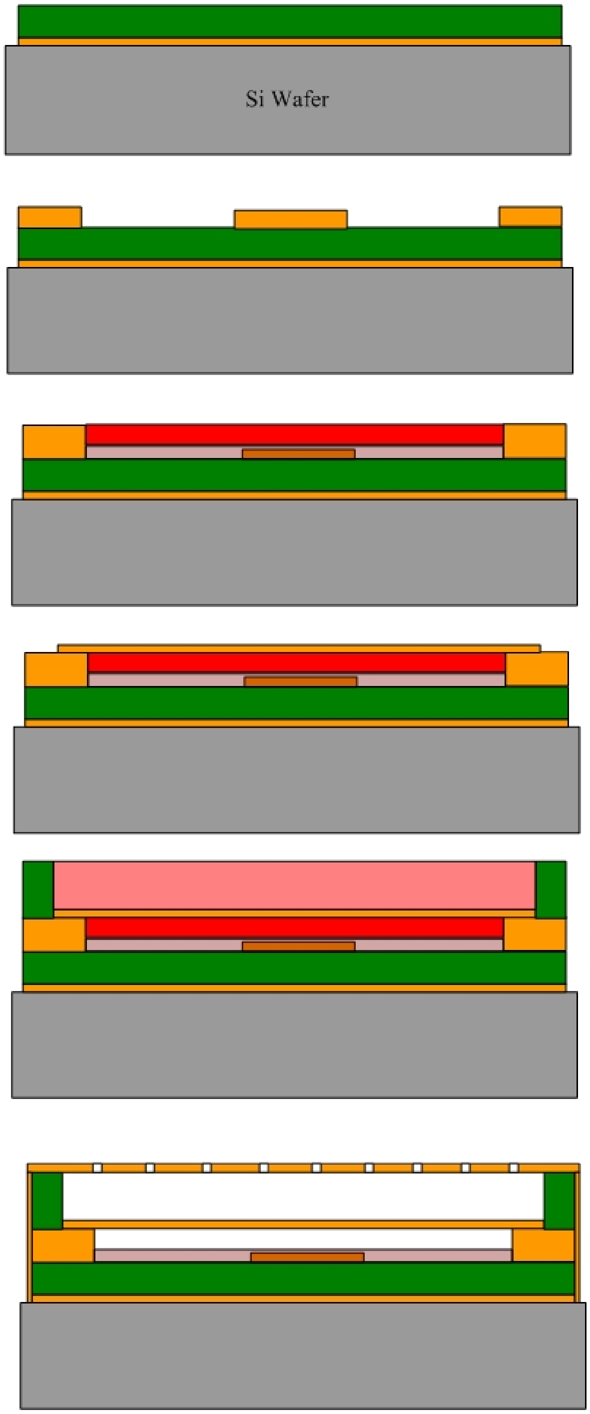

Bottom shield is formed by blanket evaporation of a Cr-Au. Polyimide HD 4010 is spun and patterned to form a 10 µm thick

Thermal evaporation and lift-off – 1 µm thick Cr-Au to form center conductor and MEM pedestals

0.25 µm thick silicon nitride deposited and RIE etched , followed by sacrificial layer for the MEM beam. Pedestal height is increased to 2.75 µm by evaporation and patterning of Cr-Au in the pedestal area

MEM beam formed by gold electroplating (~ 1 µm thick)

Top half polyimide (10 µm thick) spun and patterned around the MEM beam area, followed by filling the cavity with sacrificial AZ P4620 photoresist

Top shield is thermally evaporated, patterned and holes formed by wet etching.
Sample is immersed in Shipley 1165 remover to release the beam and the top shield and CPD is performed

Figure 4.18 Process Flow for the RF Shunt Capacitive Switch Fabrication

4.9 Conclusions

The versatility of the developed micro coax lines have been demonstrated by integrating an RF MEMS varactor inside the cavity of a semi-polyimide micro coax line. Capacitance tuning in the range of 6.5-7 was achieved with an actuation voltage of 40-60V with an unloaded Q of 20 and 14 in the up (low capacitance) and down state (high capacitance) respectively. An equivalent circuit was developed using ADS software to extract the lumped element equivalent of the device and also to deembed the micro coax transmission line from the capacitor. The performance of the varactor is comparable with similar variable capacitors realized using CPW topologies on silicon/quartz substrates.

An improved design with a capacitance ratio of 40 and shunt fixed-fixed beam configuration is being developed to be configured as an RF shunt capacitive switch for 20-35 GHz operation. Ansoft HFSS simulation results are promising with isolation values of around 35 dB and insertion loss of about 0.4 dB at 30 GHz for a calculated actuation voltage is about 11 volts. The successful integration of a MEM varactor inside a micro coax line is the first step to achieving fully shielded and vertically integrated RF MEMS circuits for high density millimeter-wave applications.

Chapter 5

Micro Coax Fed Millimeter-wave Slot Antenna

5.1 Introduction

Slot antennas or aperture antennas are commonly used at microwave and millimeter-wave frequencies where a low profile is desired. An ideal slot antenna is a rectangular aperture of length λ/2 and width ranging from λ/20 to λ/10. The slot is formed on a ground plane of the feed line or the substrate as shown in Figure 5.1. The slot antenna can be fed by different methods depending on the type of the feed line. A coaxial feed can be implemented by connecting the signal conductor and the ground to either edge (shown as F-F in Figure 5.1) of the slot. A microstrip or CPW feed can also be implemented based on the application. The impedance of the slot antenna can be matched to the impedance of the feed line using a matching network, off-center feeding, tuning stub etc.

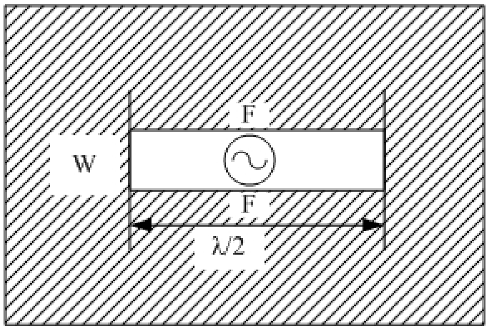

Figure 5.1 Basic Slot Antenna on a Ground Plane

Slot antennas are used for a wide band of frequencies ranging from RF to millimeter-wave. A few applications of millimeter-wave slot antennas include 60 GHz high speed wireless LANs, 77 GHz automotive radar and 94 GHz millimeter-wave sensors. These antennas are designed and fabricated on substrates such as silicon, quartz and glass depending on the application. Millimeter-wave slot antennas are usually fed by coplanar waveguides due to their good performance at millimeter-wave frequencies. The radiating slot is etched in the ground plane of the CPW line, which makes it a highly compact and integrated antenna-feed network. A CPW fed topology is also relatively simple from a fabrication standpoint and avoids coupling losses associated with an electromagnetically coupled feed [47], [48]. A electromagnetically coupled feed is typically used to feed slot antennas fabricated on printed circuit board laminates using a microstrip feed line from the backside of the substrate. One end of the feed line is aligned to the desired point on the antenna situated on the top side of the board, while the other end is terminated in a coaxial connector. The advantage of using an electromagnetically coupled feed is the decoupling of the feed line, matching network power divider/combiner and other circuitry from the antenna to avoid interference with the radiation pattern. The disadvantages of electromagnetic coupling include lateral cross-talk in high density circuits, double-side fabrication and critical alignment requirements of the feed line with the slot. Nevertheless, both CPW and microstrip feed lines are prone to cross-talk at millimeter-wave frequencies and not suitable for vertical integration of the antenna-feed network preferable in high density applications.

Cross-talk effects at millimeter-wave frequencies can be eliminated completely by using a shielded coaxial transmission line for the antenna feed. This would also enable vertical integration in high density applications where the completely shielded coaxial feed line could be placed in proximity to other circuitry on the same chip. However physical size mismatch between a millimeter-wave slot antenna and a commercially available coaxial line operating at the same frequency range poses hurdles in integrating a miniature slot antenna to a coaxial feed. In an attempt to circumvent the problem radial coaxial line slot antennas were proposed by Ligusa *et al.*[49], where the slot is etched on the outer ground shielding of a vertical coaxial line, resembling a cylinder. A half-power beam width of 18° at 15 GHz was achieved with this design. Akiyama *et al.* [50] proposed a slot antenna etched in a thick PTFE dielectric substrate fed by a coaxial feed from the bottom of the substrate to function at 12 and 60 GHz. Though the above mentioned antennas are coaxially fed, their large footprint (>20 mm^2) make on-chip implementation and integration with other microwave circuitry difficult. A fully integrated feed line antenna module has been developed using LTCC technology with an electromagnetically coupled feed and air-cavity backing to achieve high gain in the 45-75 GHz frequency range [51]. Though the antenna-feed system is relatively compact (5 mm×2.5 mm) and provides high gain, its implementation is confined to LTCC technology or multilayer PCB laminates and cannot be integrated seamlessly with the most widely used CMOS/silicon technology.

The main motivation for this research is to design a slot antenna operating at 55-65 GHz fed by an electromagnetically coupled coaxial feed line. This was achieved by etching the antenna on the top shield of an all-polyimide type micro coax feed line similar to ones explained in Chapter 2. The proposed design combines the advantages of an electromagnetically coupled feed with the complete shielding offered by a coaxial transmission line, which helps in avoiding coupling losses. The frequency band of 55-65 GHz was chosen due to the unlicensed and unrestricted usage allowed by the Federal Communications Commission (FCC), which has led to the proliferation of high data rate (>2 Giga bits per second) communication applications using the large (7 GHz) continuous bandwidth available between 57-64 GHz.

The proposed slot is shaped in the form of the letter 'H' to achieve a 50% slot length reduction and a total antenna-feed footprint less than 1 mm^2. The measured return loss was better than 15 dB in the desired 55-65 GHz frequency band. Radiation pattern measurements in the E and H-plane show a good comparison with the simulations. The peak directivity and gain obtained from Ansoft HFSS full-wave EM simulations are 3.62 dBi and -0.29 dBi, respectively, at the center frequency of 60 GHz. The antenna exhibits a unidirectional pattern (with a reflector backing) with a simulated front to back ratio of 14 dB.

5.2 57-64 GHz Frequency Band

The 55-65 GHz frequency range was chosen to exploit the potential of the large 7 GHz bandwidth available in the unlicensed 57-64 GHz band of the millimeter-wave spectrum capable of transmitting at 2 Giga bits per second data rates and greater combined with the unrestricted usage allowed by the FCC. A few applications based on high data rates include wireless chips transmitting rich multimedia content like high definition audio/video signals (HDTV) and high speed data in intranet and other short range communication networks. However, electromagnetic waves in the vicinity of 60 GHz are plagued by high attenuation caused by increased path loss due to their high rate of absorption by oxygen molecules compared to other frequencies below and above the 57-64 GHz band in addition to the complexity involved in circuit design at such high frequencies [52]. The narrow beam width of a millimeter-wave antenna is ideal for point-to-point communications without interference from other systems operating in the same frequency band. This allows for frequency re-use within a small geographical area.

5.3 Design of a Micro Coax Fed Slot Antenna

The proposed micro coax fed slot antenna is formed on the top shield of a rectangular all-polyimide micro coax feed line, 75 μm wide and 20 μm in height fabricated on a 400 μm thick high resistivity reflector-backed silicon substrate. Design of all-polyimide type micro coax lines and fabrication has been described in detail in Chapter 2. Figure 5.2 shows a picture of the integrated slot antenna-micro coax feed line. The center conductor of the micro coax feed line is situated 10 μm below the slot antenna on the top shield. The center conductor and the slot are surrounded by a polyimide layer with an outer metallic shield as indicated in Figure 5.2. A metallic reflector is placed on the bottom side of the silicon substrate (superstrate) to achieve unidirectional radiation. This helps to exploit the advantages offered by an electromagnetically coupled feed as explained in the previous section and avoid the coupling losses at the same time due to the shielding of the micro coax line.

The physical dimensions of the antenna and feed line were optimized using HFSS full-wave electromagnetic simulations prior to fabrication. The parameters considered for the design and optimization are discussed below.

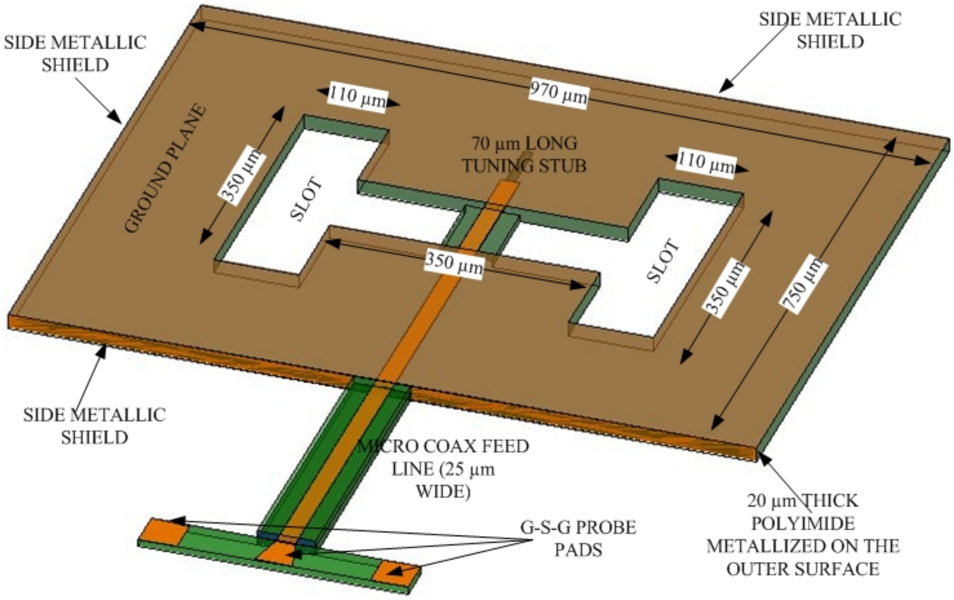

Figure 5.2 Schematic of the Proposed Micro Coax Fed Slot Antenna

The antenna was fabricated on a 20 μm thick polyimide layer (HD 4010) of dielectric permittivity 4.2 and a loss tangent of 0.11 at 60 GHz. The center conductor of the micro coax feed line is sandwiched between 10 μm thick polyimide layers as shown in Figure 5.2. The complete structure comprising the antenna and feed was fabricated on a 400 μm thick reflector-backed high resistivity silicon wafer.

The initial dimensions of the radiating slot were set as λ/2 in length and λ/10 in width, where the wavelength, λ is given by-

$$\lambda = \frac{C}{Freq \times \sqrt{\varepsilon_r}} \text{ (m)} \tag{5.1}$$

Where, C = Speed of light = 3×10^8 m/sec

ε_r = permittivity of the antenna substrate = 4.2 for the case of polyimide, HD 4010

$Freq$ = Frequency in Hz

The length of the slot is obtained using (5.1) as λ/2 = 1220 μm leading to a slot width of λ/20 = 61 μm. These values were used as the initial conditions for full-wave electromagnetic simulations and optimized to obtain the desired performance in the 55-65 GHz frequency band. In an attempt to reduce the slot length, the slot was split into three, 350 μm long arms and arranged in the form of the letter ‘H’ as shown in Figure 5.2. This led to a slot length reduction of 50%. The length of the new slot measured between the outer edges of the vertical arms of the slot is 570 μm, while the perimeter of the slot also reduced to 1050 μm against the calculated 1220 μm. The slot width was also optimized to 110 μm from the initial value of 61 μm to achieve the required bandwidth and return loss.

The slot is center-fed by electromagnetic coupling through the center conductor of the micro coax feed line, 10 μm below the antenna surface. The polyimide layer below the slot was etched away except for a pedestal (75 μm wide and 110 μm long) to support the center conductor. This led to a gain improvement of 100% due to the reduction of coupling losses through the lossy polyimide layer. The power radiated by an antenna is directly proportional to the power accepted at the antenna terminals from the feed network. So, a good impedance match between the antenna and the feed network is essential to achieve maximum efficiency. Impedance matching is performed by optimizing the length of the feed line, using an off-center and/or inclined feed or by including a tuning stub.

The optimum physical length of the feed line was determined as 125 µm using electromagnetic simulations to provide a good impedance match for the antenna. The position of the feed line with respect to the length of the slot plays a significant role in impedance matching. The conventional position of the feed line is perpendicular and centered with respect to the length of the slot to achieve a symmetrical radiation pattern. It has been established that a lateral and angular offset of the feed line with respect to the slot helps to reduce the antenna terminal impedance seen by the feed network, thus obtaining a better match [53]. Figure 5.3 shows a representation of the offset feeding in the proposed 'H' shaped slot antenna.

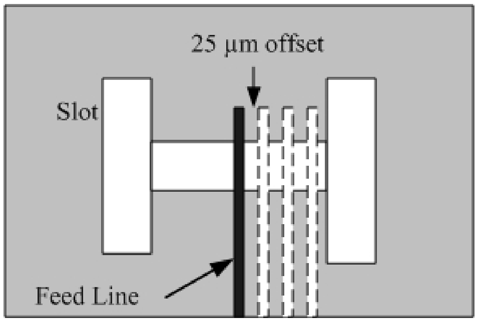

Figure 5.3 Offset Feed in a Slot Antenna

Electromagnetic simulations were used to analyze the effect of offset feeding for the micro coax fed slot antenna. Results comparing a feed line with no offset and a 25, 50, 75 or 100 µm lateral offset are shown in Figure 5.4. It can be observed that an offset of 75 µm provides the best impedance match at about 62.4 GHz, but the lower frequency point of the 15 dB bandwidth region is shifted to 58 GHz compared to 55 GHz for the no offset case, causing a bandwidth reduction of 5%. So, the choice of an offset feed is made depending on the desired return loss, center frequency and the bandwidth. Analysis of the effect of offset feeding can also be used to predict the shift in center frequency due to lateral misalignment of the center conductor with respect to the slot. For example, it can be deduced from Figure 5.4 that a 25 µm offset in the center conductor shifts the center frequency from 59.2 to 69.2 or a 10% shift in the frequency considering a 10 GHz range.

A tuning stub can also be used to match the antenna impedance to the feed line. It is essentially an open-circuited line, λ/4 long formed by extending the feed line (as shown in Figure 5.2) beyond the outer edge of the slot to realize an effective short at the edge of the slot antenna. This provides a reactive loading of the antenna, thereby changing the resonant frequency. It is designed in such a way that the input resistance compares with the feed line impedance at the new resonant frequency of the antenna [53]. The stub length is then tuned by electromagnetic simulations to achieve the best impedance match within the desired frequency range of operation. In the case of the proposed slot antenna, an optimized stub length of 70 µm was used.

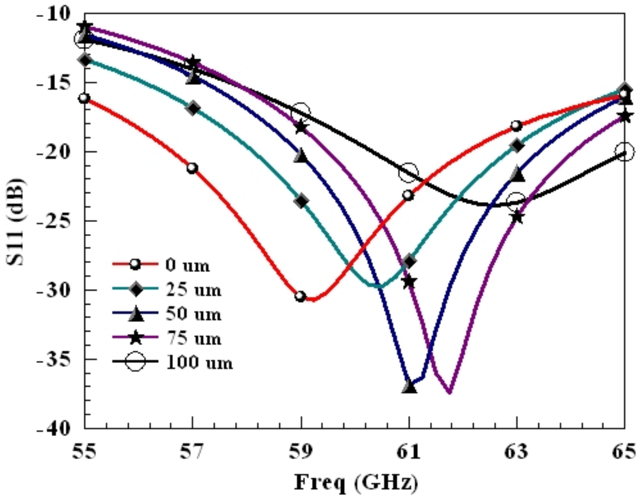

Figure 5.4 Effect of Offset Feeding in the Micro Coax Fed Slot Antenna

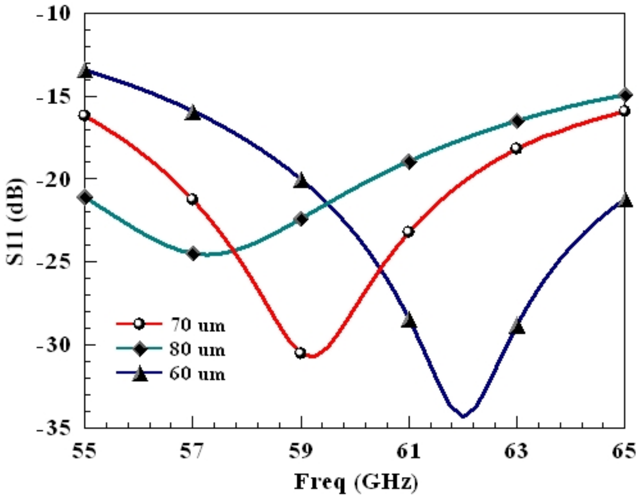

Figure 5.5 Effect of Tuning Stub Length in the Micro Coax Fed Slot Antenna

Simulation results of the micro coax fed slot antenna with tuning stubs of 60, 70 and 80 µm length shown in Figure 5.5 indicate that the impedance match improves with decreasing stub length with an upward shift in the center frequency. It was also observed that long tuning stubs can be bent in the form of a ‘T’ with the same overall length to make them more compact without compromising antenna performance.

The size of the ground plane is a significant design parameter that decides the shape and beam width. This is because the current in a slot antenna is not confined to the edges of the slot, but spread throughout the ground plane. Ideally, a flat sheet or ground plane of infinite area would be preferred because a slot etched in an infinite ground plane produces an electric field pattern constant in magnitude along a radial direction measured along the normal to the slot. This would lead to perfectly symmetrical, hemi-spherical radiation pattern above and below the ground plane. But an infinite ground plane may not be possible in practical applications, where the extent of the ground plane is limited due to overall circuit or substrate size. In such a finite ground plane case, the electric fields on either side of the ground plane are equal in magnitude but opposite in phase such that undulations or dips appear in the radiation pattern. The number of undulations or dips increases with increasing ground plane area, but the magnitude decreases, tending to zero as the ground plane area tends to infinity.

The dimensions of the ground plane in the proposed slot antenna were varied from one wavelength to multiple wavelengths in all directions and analyzed by electromagnetic simulations to obtain the maximum directivity and gain. A ground plane area of 970 μm×750 μm was chosen to maintain the footprint of the antenna and feed network as small as possible without compromising on the directivity and gain. A combined antenna-feed line footprint of 1mm^2 was achieved, which is significantly smaller than previously published slot antenna designs operating in the same frequency range [54], [55].

5.4 Fabrication

Simplified steps for the fabrication of the integrated micro coax slot antenna-feed line are given below. A microphotograph of a fabricated slot-antenna is shown in Figure 5.6

a. Bottom Shield formed by patterning photoresist-NR1-3000PY to lift-off thermally evaporated of Cr-Au (~ 1 μm thick). This forms the bottom shield for the micro coax feed line and the TRL calibration lines
b. Bottom Polyimide-HD 4010 is spun and lithographically patterned to get a 10 μm thick polyimide layer. This acts as a platform for the G-S-G probe pads and the center conductor of the micro coax feed line
c. Center Conductor (feed line) formed by lithographically patterning photoresist NR1-3000 PY and thermal evaporation of Cr/Au (~ 1 μm thick) followed by a lift-off

d. Top Polyimide, 10 μm thick is spun and patterned to cover the feed line portion (without the probe pads) and the area surrounding the slot

e. Outer shield formed by layer of Ti/Al (~ 0.4 μm thick) is evaporated over the structures, patterned with photoresist and wet etched to form the outer metallic shielding for the feed line and the ground plane for the slot

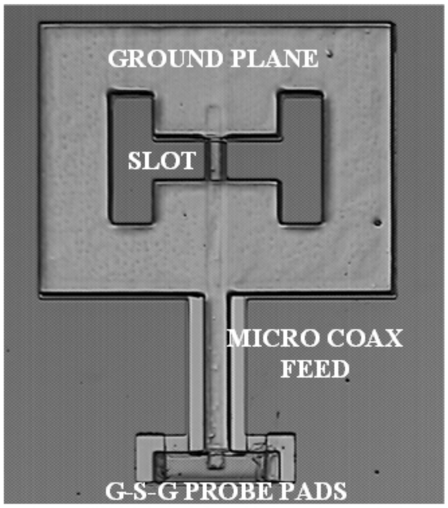

Figure 5.6 Microphotograph of a fabricated Slot Antenna-Feed Line

5.5 Results and Discussion

The return loss of the slot antenna was measured using microwave G-S-G probes and an Anritsu Lightning Vector Network Analyzer. The silicon substrate with the antennas was placed on a metal chuck which acts as a reflector to achieve unidirectional radiation. An on-wafer TRL calibration was performed using micro-coax TRL standards designed to set the measurement reference plane such that it includes a 125 μm length of the feed line for impedance matching.

A comparison of the measured and simulated return loss of the antenna and feed line is shown in Figure 5.7. The slight difference between the measured and simulated values can be attributed to fabrication imperfections and variation of material properties such as polyimide dielectric constant, metal loss, etc. due to fabrication conditions. The return loss of the antenna is better than 15 dB across 55-65 GHz, which translates to a 15 dB bandwidth of 17%. The VSWR obtained from the measured S_{11} is better than 1.35 throughout the frequency band of 55-65 GHz. The return loss obtained in this work compares well with published results for a bow-tie slot antenna implemented on a bulk micromachined silicon wafer as an on-chip miniature antenna and a tapered slot antenna implemented in a CPW feed line, both for the same unlicensed 57-64 GHz band [54], [55]. In addition the micro coax fed slot antenna presented in this research has a 10× smaller footprint than antennas fabricated on bulk micromachined silicon membranes. Further more the fabrication process is much simpler and amenable to vertical integration. However the efficiency and gain of the antennas fabricated on thin silicon membranes are expected to be multifold higher than that of the proposed design. This is due to the reduction of substrate losses and surface waves in a thin membrane compared to a bulk silicon wafer. So, a trade-off has to be made between vertical integration, ease of fabrication and high efficiency/gain.

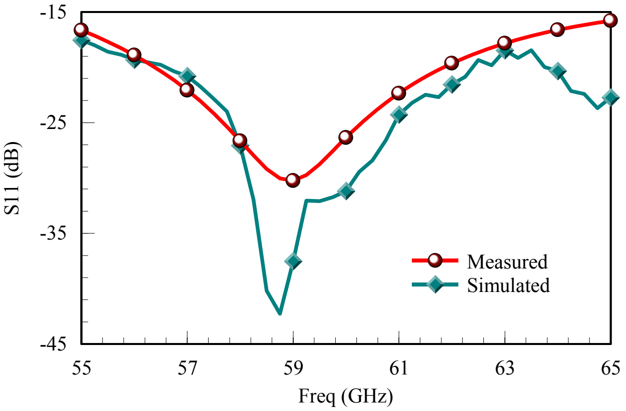

Figure 5.7 Simulated and Measured Return Loss of the Slot Antenna-Feed Line

Though a slot antenna is energized from its edges, the current is not confined to the edges of the slot, but is spread over the entire ground plane. This makes it a perfect symmetrical and bi-directional radiator [56], [57] whose radiation pattern resembles a λ/2 dipole. The electric and magnetic field patterns of a slot antenna can be deduced from pre-determined complimentary linear antenna equations developed for a dipole by applying Babinet’s principle, which states that, “The field at any point behind a plane having a screen, if added to the field at the same point when the complementary screen is substituted, is equal to the field when no screen is present”. This principle allows the analysis of a λ/2 slot antenna like a λ/2 dipole to evaluate the |E| and |H| field of the antenna.

The co and cross-polarized radiation patterns were measured using the custom measurement setup shown in Figure 5.8. The antenna under test was placed on a microwave probe station and fed from a 60 GHz GUNN oscillator through G-S-G microwave probes. A 50-75 GHz standard gain horn was used as a receiving antenna. The horn was connected to an

Agilent 8565EC spectrum analyzer using a HP 11970V harmonic mixer to extend the frequency range of the spectrum analyzer from 50 to 75 GHz. A custom-built semi-circular guiding fixture was used to support the horn antenna and the mixer such that the radial distance measured along the normal to the radiating surface of the horn and the center of the slot antenna is constant as the horn is moved from 0° to 180° degrees. The radiated power received by the horn from the slot antenna under test was recorded in the spectrum analyzer at every 10° step to trace the radiation pattern. The receiving horn was moved along a path parallel to the length of the feed line to trace the E-plane pattern and perpendicular to the length of the feed line to trace the H-plane pattern. The longer side of the rectangular flare of the horn was held parallel to the width of the feed line to measure the co-polarized E and H-plane pattern.

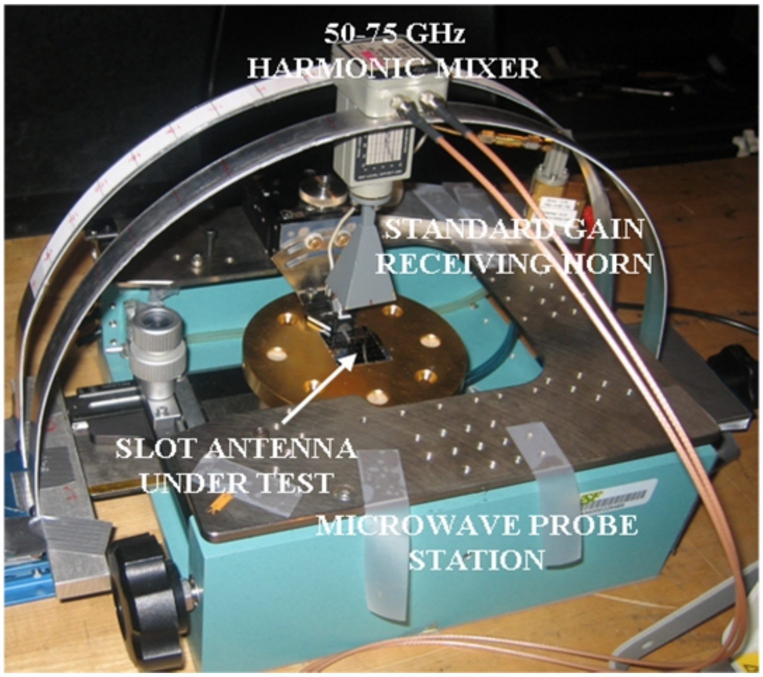

Figure 5.8 Custom Antenna Pattern Measurement Setup

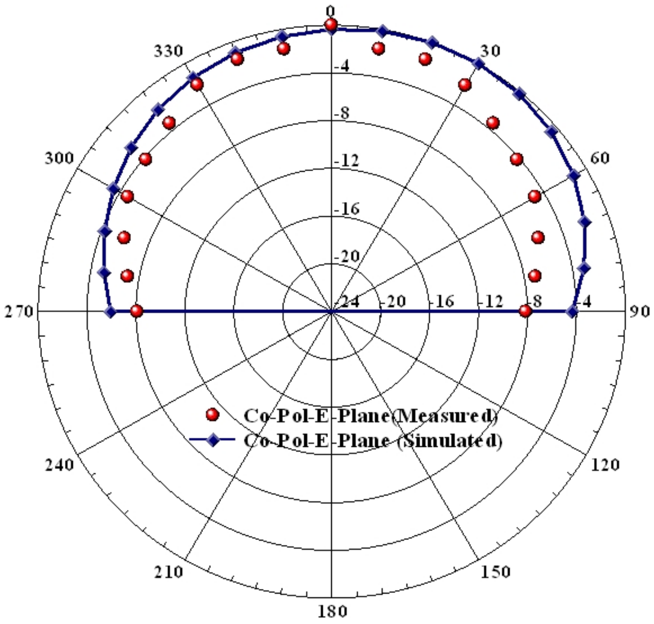

Figure 5.9 Measured and Simulated Co-Polarized E-Plane Pattern (in dB)

Figure 5.9 and Figure 5.10 show the normalized measured and simulated co-polarized E and H-plane patterns for the slot antenna respectively. The radiation pattern measurements are in good agreement with simulated results obtained from HFSS. Ideally the electric and magnetic fields of a slot antenna are constant in magnitude in a radial direction measured from 0 to 180° leading to a perfect hemi-spherical radiation pattern on each side of the ground plane (in the absence of a reflector on the back side of the substrate). The slight difference in the magnitudes of the measured versus the simulated patterns is due to the inaccuracies in the measurement setup which requires precise positioning of the receiving antenna on the guiding structure. The measured half-power beam width (HPBW) is 110° compared to 180° in HFSS simulations, both at 60 GHz. The reduction in the measured HPBW can be attributed to losses in the measurement setup and positioning inaccuracies.

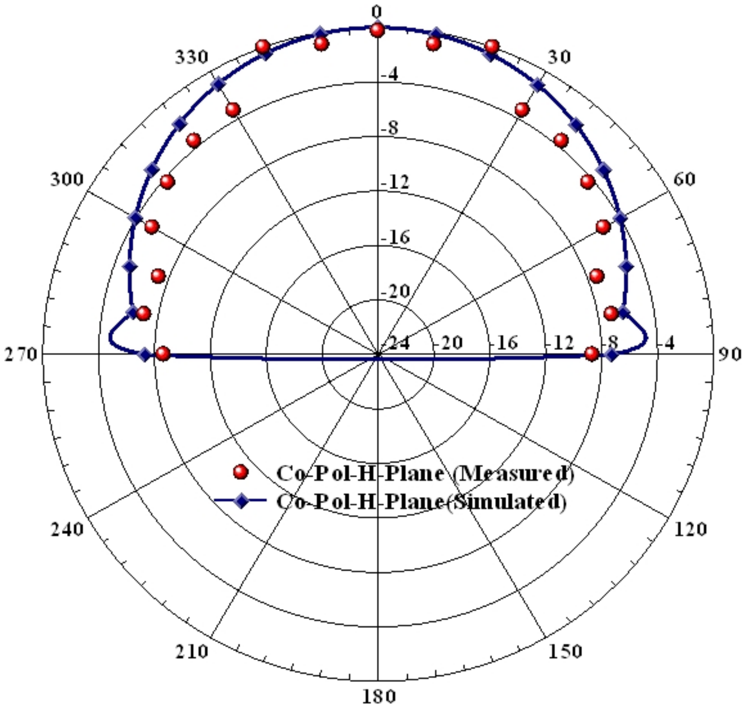

Figure 5.8 Measured and Simulated Co-Polarized H-Plane Pattern (in dB)

Figure 5.9 shows the cross-polarized E and H-plane pattern of the slot antenna. The setup is very similar to the one used for the co-polarized measurement except that the longer side of the rectangular flare of the receiving horn antenna was held perpendicular to the width of the feed line to measure the cross-polarized pattern. The maximum cross-polarization magnitude is close to -15 dB in the E-plane and -30 dB in the H-plane. This follows the theory of slot antennas known to have low cross-polarization levels in the order of -25 dB.

Antenna parameters obtained from full-wave HFSS electromagnetic simulations are listed in Table 5.1. The parameters were calculated based on an isotropic radiator emitting 1 Watt incident power to the antenna under test. A front-to-back ratio of about 14 dB was observed at 180° and a null was observed at 200° in the antenna gain simulations. The back radiation can be reduced (to increase the front-to-back ratio) further by optimizing the distance between the antenna and the reflector and etching the silicon substrate beneath the antenna to reduce surface waves and substrate losses.

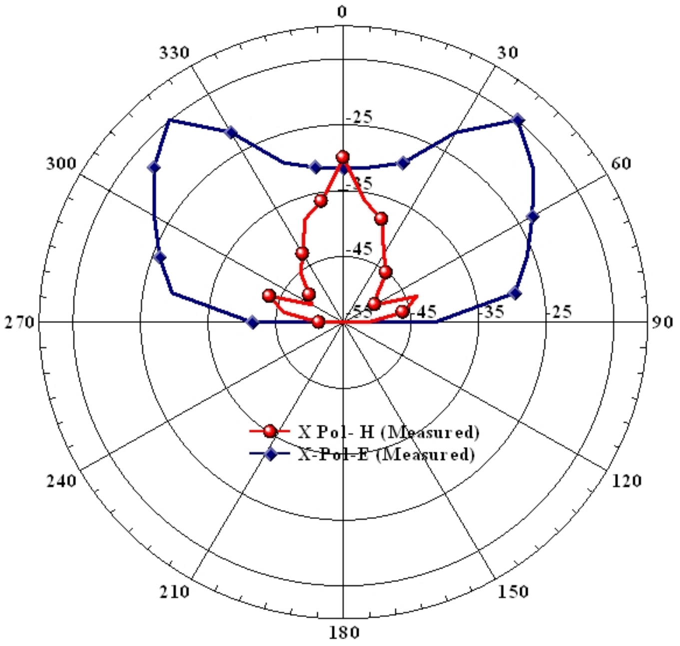

Figure 5.9 Cross-Polarized Measurement of the E and H-Plane Radiation Pattern (in dB)

Table 5.1. Antenna Parameters from Electromagnetic Simulations

Parameter	Value
Max. Radiation Intensity	0.07 W/Sr
Incident Power	1 W
Accepted Power	0.99 W
Radiated Power	0.40 W
Radiation Efficiency	40.71%
Gain	-0.29 dBi
Directivity	3.62 dBi
Half Power Beam Width	180°

5.6 Conclusions

A miniature H-shaped slot antenna fed by a micro coax feed line was designed, fabricated and measured. The measured return loss was better than 15 dB throughout the desired frequency range of 55-65 GHz. The co-polarized E and H-plane radiation pattern measurement results compared well with HFSS simulated patterns. The measured cross-polarization levels are low as expected for a slot antenna.

A low height profile of 20 μm with a foot print less than 1 mm^2 and simple fabrication steps makes it amenable to integration with other on-wafer microwave circuits. Further more, MEMS technology can be used to integrate RF switches and phase shifters to realize an antenna array or a multi-frequency design similar to the one described in [58]. Applications of this antenna include millimeter-wave sensors, non-invasive biological probes and short range high data rate communication applications operating in the unlicensed 57-64 GHz band.

Chapter 6

Summary and Recommendations

6.1 Summary

The work presented in this dissertation was aimed at developing the concept of rectangular coaxial lines for on-wafer high density integrated microwave circuit applications. The initial research involved design of miniature rectangular coaxial lines suitable for integration with planar microwave circuitry. Theoretical equations and electromagnetic simulations were used to design lines of varying physical dimensions and characteristic impedance values. A substantial effort was made to develop process flows and fabrication methods to realize the micro coaxial lines on CMOS grade silicon wafers using standard MEMS fabrication techniques. Three types of micro coaxial lines with air, semi-polyimide and an all-polyimide core were designed, fabricated and measured. The merits and demerits of each design were analyzed in terms of microwave performance, fabrication complexity and adaptability to integration of devices inside the micro coax cavity, vertical integration etc. The possible reasons for the high loss of micro coax lines relative to other planar transmission lines was presented .The fact that a micro coax line is not affected by bends and has near zero cross-coupling with other lines in proximity was demonstrated by simulation results.

A semi-polyimide core type micro coax line was chosen to embed a MEM device within the cavity of a coax line. A section of the center conductor was suspended by etching a 1.5 µm deep trench in the polyimide to create a fixed-fixed beam. Electrostatic actuation was used to move the beam and snap down on a silicon nitride capped gold pedestal. A capacitance ratio of 6.5-7 was achieved between the actuated and non-actuated states with an actuation voltage of 40-60V. Though the concept of a MEM variable capacitor is not new, the fact that the capacitor is located inside a shielded micro coax cavity is novel and opens up new venues for highly integrated circuits that can offer cross-talk free performance at any frequency. Furthermore, the variable capacitor has been redesigned to offer a capacitance ratio in the range of 40, that can be configured as an RF MEMS shunt switch. Once fabricated, this would result in an RF MEM switch capable of 1-40 GHz operation that is fully integrated and shielded inside a transmission line cavity.

The vertical integration capability of a micro coax line was demonstrated using an all-polyimide micro coax line integrated with a millimeter-wave slot antenna etched on the top shield of the micro coax line. The micro coax line along with the antenna was fabricated on a 400 µm thick silicon substrate. The slot was designed to radiate in the 55-65 GHz frequency range to cover the unlicensed 57-64 GHz band, which offers high data rates due to the large continuous 7 GHz bandwidth. The slot is formed on the top shield of the micro coax line and electromagnetically fed by the center conductor 10 µm below it. The antenna was designed and optimized using Ansoft HFSS simulations. A design analysis was performed to evaluate the effect of offset feeding and use of a tuning stub for impedance matching. Measurement results of the fabricated antenna showed a 15 dB bandwidth of 17% and a radiation pattern closely matching the simulation results. The antenna was designed for a unidirectional radiation by using a reflector at the bottom of the silicon substrate.

6.2 Recommendations for Future Work

The micro coax transmission line technology holds immense potential for developing a multitude of highly integrated microwave and millimeter-wave circuitry. A few of the several recommendations to improve and enhance this research are listed here.

a. Basic Micro Coax Transmission Lines

Process flows can be modified to increase the height of the two polyimide layers and achieve a total height of at least 40 µm in the basic micro coax line to achieve higher Z_0 values with wider conductor widths. Polymers other than BCB and HD4010 can be used to achieve thicker layers and higher temperature resistance (>375^{o}C). Some prospective materials include CVD polysilicon, amorphous silicon and TEOS silicon dioxide which can be tailored to particular applications in terms of thickness, loss tangent, resistivity, dielectric constant etc by manipulating deposition conditions. This would help to reduce the line losses while maintaining the advantage of a low profile relative to similar micro coax topologies proposed by other researchers. In addition thick sacrificial layers and minimal stress fabrication methods can be researched to realize reliable and robust air core lines to harness the full potential of a micro coax line i.e.

complete shielding, low loss, dispersion-free and amenable to vertical integration to realize the ultimate micro coax based system called the µCORAL with multi-layer interconnects and integrated circuits (see Figure 6.1).

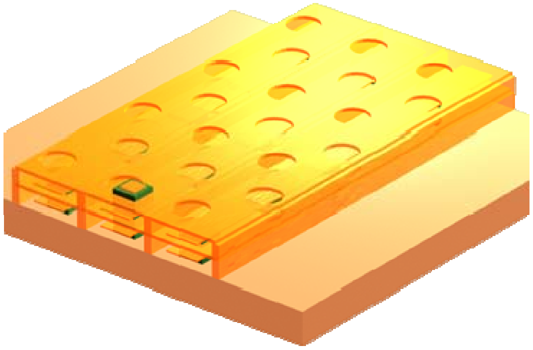

Figure 6.1 Proposed Multilayer µCORAL Structure

b. Embedded RF MEM Devices

The performance of the MEM varactor can be improved by reducing the residual stress in the MEM beam using sputter deposited gold and planarization of the PMGI sacrificial layer either by re-flow or chemical mechanical polishing. Switching speed, reliability and life time of the MEM varactor can be measured. The proposed RF shunt capacitive switch could be fabricated, measured and reconfigured to realize an RF MEMS filter or phase shifter to be integrated with the slot antenna developed in this research.

c. Millimeter-wave Slot Antenna

Gain and directivity measurements can be performed on the slot antenna and the position of the reflector can be optimized to achieve the least backside radiation and thereby increase the gain. Further, the antenna can be integrated with a micro coax feed embedded with a MEM varactor and/or a switch for integrated impedance tuning and electronic steering by configuring the switch as a phase shifter. Multiple switches can be cascaded to achieve a wide range of phase tuning. Alternatively the top shield of the micro coax feed can be extended to support a slot antenna array.

d. Biological Impedance Probe

This technology has immense potential for rapid and sensitive detection of bacteria or other micro organisms. A detailed description of the preliminary work done in this area using a prototype macro coaxial probe and implementation of the concept using an integrated micro coax probe-microfluidic chamber is presented in Appendix C. Testing can be continued with bacteria using RF signals of varying power levels to see if its helps to increase the sensitivity. Also, the open surface of the micro coax probe can be coated with biological binding agents to effectively capture the maximum number of bacteria that may be in the test sample to increase detection sensitivity. Further more, algorithms can be developed based on the impedance data to impart specificity to the sensing method.

e. Packaging

Efficient and low cost packaging is paramount to the success of any device. The unique feature of a micro coax based circuit is that it is inherently packaged in a metallic shield. In the case of an all-polyimide type micro coax, the device can be readily encapsulated by coating a film of parylene or other inert polymer materials such as PDMS. The air core and semi-polyimide core micro coax structures need a cavity to enclose their top shield due to the presence of holes in it. In this case a polymer mould resembling a rectangular lid or a glass wafer with an etched cavity (cavity height to be slightly greater than total micro coax line height) can be used to enclose the micro coax line. The edges of the glass can be anodically bonded to the silicon wafer carrying the micro coax circuits. The only possible drawback of a micro coax polyimide (HD4010) based circuit is its sensitivity to temperatures above 375^{o}C, which is the glass transition temperature of the cured polyimide. However this can be manipulated according to packaging needs by substituting other structural materials such as polysilicon, amorphous silicon, TEOS silicon dioxide etc that can withstand upwards of a 1000^{o}C. The greatest advantage of a micro coax line is that, its shielding protects it from performance deterioration that may result from packaging.

References

[1] D. M. Pozar, *Microwave Engineering, 2^{nd} ed.*, New York, Wiley: 1998

[2] M. E. Thomas, I. A. Saadat, S. Sekigahama," Multilevel Microcoaxial Interconnect: a novel technology for VLSI microwave circuits", *Proc. Eighth IEEE Intl. VLSI Multilevel Interconnection Conference*, pp. 116-122, Jun. 1991

[3] R. F. Drayton, R. M. Henderson, L. P. B. Katehi, " *IEEE Transactions on Microwave Theory and Techniques*, vol. 46, no. 7, pp. 534-543, Jul. 1998

[4] T. M. Weller, L.P.B. Katehi and G. M. Rebeiz," High Performance Microshield Line Components" *IEEE Transactions on Microwave Theory and Techniques*, vol. 43, no. 3, pp. 534-543, Mar. 1995

[5] T. Ishikawa and E. Yamashita, "Characterization of Buried Microstrip Lines for Constructing High-Density Microwave Integrated Circuits" *IEEE Transactions on Microwave Theory and Techniques*, vol. 44, no. 6, pp. 840-547, Jun. 1996

[6] L. P. Dunleavy, P. B. Katehi, "Shielding Effects in Microstrip Discontinuities", vol. 36, no. 12, pp. 1767-1774, Dec. 1988

[7] J. Jin, S.S.H. Hsu, M. Yang and S. Liu, "Low-Loss Differential Semicoaxial Interconnects in CMOS Process", *IEEE Transactions on Microwave Theory and Techniques*, vol. 54, no. 12, pp. 4333-4340, Dec. 2006

[8] S. B. Cohn, "Characteristic Impedance of the Shielded-Strip Transmission Line", *IEEE Transactions on Microwave Theory and Techniques*, vol. 2, no. 2, , pp. 52-57, Jan. 1954

[9] J. J. Skiles, "Exact Analytic Determination of the Capacitance and the Characteristic Impedance of Coaxial Rectangular Transmission Lines by the use of Orthonormal Block Analysis", PhD Thesis, Dept. of Electrical Engg., University of Wisconsin Madison, WI, 1954

[10] T. S. Chen, "Determination of capacitance, inductance and characteristic impedance of rectangular lines", *IRE Transactions on Microwave Theory and Techniques*, vol. 8, no. 5, pp. 510-519, Sep. 1960

[11] R. V. Garver, "Z_o of Rectangular Coax (Correspondence)", *IEEE Transactions on Microwave Theory and Techniques*, vol. 9, no. 3, pp. 262-263, May. 1961

[12] W. J. Getsinger, "Coupled Bars Between Parallel Plates", *IEEE Transactions on Microwave Theory and Techniques*, vol. 10, no. 1, pp. 65-72, Jan. 1962

[13] H. E. Green, “Characteristic Impedance of Square Coaxial Line (Correspondence)”, *IEEE Transactions on Microwave Theory and Techniques,* vol. 11, no. 6, pp. 554-555, Nov. 1963

[14] S. w. Conning, “Characteristic Impedance of Square Coaxial Line (Correspondence)”, *IEEE Transactions on Microwave Theory and Techniques,* vol. 12, no. 4, pp. 468-468, Jul. 1964

[15] O. R. Cruzan and R. V. Garver, “Characteristic Impedance of Rectangular Coaxial Transmission Lines” *IEEE Transactions on Microwave Theory and Techniques,* vol. 12, no. 5, pp. 488-495, Sep. 1964

[16] C. M. Weil, “The Characteristic Impedance of Rectangular Transmission Lines with Thin Center Conductor and Air Dielectric”, *IEEE Transactions on Microwave Theory and Techniques,* vol. 26, no. 4, pp. 238-242, Apr. 1978

[17] J. A Bishop *et al.*, “Monolithic Coaxial Transmission Lines for mm-Wave ICs”, *Proc. IEEE/Cornell Conference on High Speed Semiconductor Devices and Circuits,* pp. 252-260, Aug. 1991

[18] I. Jeong, B. Kim, Y. Kwon, “Monolithic implementation of air-filled rectangular coaxial line”, *Electronics Letters,* vol. 36, no. 3, pp. 228-230, Feb. 2000

[19] I. Jeong *et al*., ”High performance air-gap transmission line and inductors for millimeter-wave applications”, *IEEE Transactions on Microwave Theory and Techniques,* vol. 50, no. 12, pp. 2850-2855, Dec. 2002

[20] E. R. Brown *et al.* ,“Characteristics of Microfabricated Rectangular Coax in the Ka Band”, *Microwave and Optical Technology Letters,* vol. 40, no. 5, pp. 365-368, Mar 2004

[21] R. T. Chen, E. R. Brown, “An ultra-compact Low Loss 30-GHz Micromachined Coaxial Filter”, *Proc. European Microwave Conference,* pp. 633-636, Oct. 2005

[22] J. R. Reid, E. D. Marsh, R. T. Webster, “Micromachined rectangular-coaxial transmission lines”, *IEEE Transactions on Microwave Theory and Techniques,* vol. 54, no. 8, pp. 433-3442, Aug. 2006

[23] D. S. Filipovic *et al.*, “Modeling, Design, Fabrication, and Performance of Rectangular µCoaxial Lines and Components”, *Proc. IEEE Intl. Microwave Symposium Digest,* pp. 1393-1396**,** Jun. 2006

[24] T. Edwards, *Foundations for Microstrip Circuit Design, 2nd ed.,* New York: Wiley, 1992

[25] J. Capwell, T. Weller, D. Markell and L. Dunleavy, Automation and Real-time Verification of Passive Component S-parameter Measurements Using Loss Factor Calculations” *Microwave Journal,* vol. 47, no. 3, Mar. 2004

[26] R. J. P. Douville and D. S. James, “Experimental Study of Symmetric Microstrip Bends and Their Compensation”, *IEEE Transactions on Microwave Theory and Techniques*, vol. 26, no. 3, pp. 175-181, Mar. 1978

[27] T. M. Weller *et al.*, “Three-Dimensional High Frequency Distribution Networks—Part I: Optimization of CPW Discontinuities”, *IEEE Transactions on Microwave Theory and Techniques*, vol. 48, no. 10, pp. 1635-1642, Oct. 2000

[28] B. Lakshminarayanan and T. M. Weller, “CPW line-to-line coupling on glass and low resistivity silicon”, *Proc. 62nd ARFTG Microwave Measurements Conference,* pp. 239-242, Dec. 2003

[29] G.M. Rebeiz and J.B. Muldavin, ”RF MEMS Switches and Switch Circuits”, *IEEE Microwave Magazine*, pp. 59-71, Dec. 2001

[30] L.P.B. Katehi, J. F. Harvey, E. Brown, “MEMS and Si Micromachined Circuits for High Frequency Applications”, *IEEE Transactions on Microwave Theory and Techniques*, vol. 50, no. 3, pp. 858-866, Mar. 2002

[31] D. J. Young and B. E. Boser, “A micromachined variable capacitor for monolithic low-noise VCOs, *Solid-State and Actuator Workshop*, Hilton Head, pp. 86-89, Jun. 1996

[32] A. Dec and K. Suyama, “Micromachined electro-mechanically tunable capacitors and their applications to RF IC’s, *IEEE Transactions on Microwave Theory and Techniques*”, vol. 46, no. 12, pp. 2587-2595, Dec. 1998

[33] E. S. Hung and S. D. Senturia, “ Tunable capacitors with programmable capacitance -voltage characteristic, *Solid-State and Actuator Workshop*, pp. 345-348, Jun. 1998

[34] H. Kannan, B. Lakshminarayanan and T. M. Weller, Multi-Finger RF MEMS Variable Capacitors for RF Applications”, *34th European Microwave Conference Digest*, vol. 2, pp. 717-720, Oct. 2005

[35] Th. G.S.M. Rijks *et al*., “Microelectromechanical tunable capacitors for reconfigurable RF architectures”, *Journal of Micromechanics and Microengineering*, vol. 16, pp. 601-611, Mar. 2006

[36] R.L. Borwick III , P.A. Stupar, J.F. DeNatale, R. Anderson, R. Erlandson, “Variable MEMS capacitors implemented into RF filter systems”, *IEEE Transactions on Microwave Theory and Techniques*”, vol. 51, no. 1, Part 2, pp. 315-319, Jan. 2003

[37] N. Hoivik *et al*., “Digitally controllable variable High-Q MEMS capacitor for RF applications”, *IEEE Intl. Microwave Symp. Digest*, vol. 3 , pp. 2115-2118, 2001

[38] T. Ikehashi *et al*., “A Robust RF MEMS Variable Capacitor with Piezoelectric and Electrostatic Actuation”, *IEEE Intl. Microwave Symp. Digest*, pp. 39-42, Jun. 2006

[39] G. M. Rebeiz, *RF MEMS Theory, Design, and Technology*, New York, Wiley: 2003

[40] X. Yuan, J. C. M. Hwang, D. Forehand and C. Goldsmith, “Modeling and characterization of dielectric-charging effects in RF MEMS capacitive switches”, *IEEE Intl. Microwave Symp. Digest*, pp. 753-756, Jun. 2005

[41] E. L. Larson, R. H. Hackett, M. A. Melendes and R. F. Lohr, “Micromachined microwave actuator (MIMAC) technology — a tuning approach for microwave integrated circuits”, *Microwave and Millimeter-Wave Monolithic Circuits Symposium Digest*, pp. 27-30, Jun. 1991

[42] D. Mercier, K. Van Caekenberghe, G. M. Rebeiz, “Miniature RF MEMS switched capacitors”, *IEEE Intl. Microwave Symp. Digest*, pp. 745-748, Jun. 2005

[43] B. Lakshminarayanan, G. M. Rebeiz, “High-Power High-Reliability Sub-Microsecond RF MEMS Switched Capacitors”, *IEEE Intl. Microwave Symp. Digest*, pp. 1801-1804, Jun. 2007

[44] J. Muldavin, C. Bozler, C. Keast, “Wafer-Scale Packaged RF-MEMS Switches“, *IEEE Intl. Microwave Symp. Digest*, pp. 267-270, Jun. 2006

[45] R. Al-Dahleh and R. R. Mansour, “A Novel Warped-Beam Design that Enhances RF Performance of Capacitive MEMS Switches” *IEEE Intl. Microwave Symp. Digest*, pp. 1813-1816, Jun. 2007

[46] J. B. Muldavin and G. M. Rebeiz, “High Isolation MEMS Shunt Switches, Part 1: Modeling, *IEEE Transactions on Microwave Theory and Techniques*”, vol. 48, no. 6, pp. 1045-1052, Jun. 2000

[47] S. Ranvier, C. Icheln, P. Vainikainen, F. Ferrero, C. Luxey, R. Staraj, G. Jacquemod, “Integrated MM-Wave MIMO Antenna with Directional Diversity using MEMS Technology”, *Proc. 13th Intl. Conference on Electronics, Circuits and Systems*, Dec. 2006, pp. 447-450

[48] S. K. Padhi, N. C. Karmakar, C. L. Law, S. Aditya, Z. Shen; P. Hui, “Microstrip-fed slot antenna for millimeter-wave RFID system”, *Proc. Asia Pacific Microwave Conference*, Dec. 2000, pp. 1396-1399

[49] K. Iigusa, S. Yamamoto, M. Tanaka, T. Teshirogi, “A slot-array antenna on a coaxial cylinder”, *Proc. IEEE Intl. Symp. on Antennas and Propagation*, vol. 3, no. 21-26, Jun. 1998, pp.1434-1437

[50] A. Akiyama, J. Hirokawa, M. Ando, E. Takeda, Y. Arai, “Characteristics of 60 GHz band conical beam radial line slot antennas”, *Proc. IEEE Intl. Symp. Antennas and Propagation*”, vol. 3, no. 11-16, Jul. 1999, pp. 2122-2125

[51] I. K. Kim *et al.*, "Linear Tapered Cavity Backed Slot Antenna for Millimeter-Wave LTCC Modules", *Antennas and Wireless Propagation Letters*, vol. 5, no. 1, pp. 175-178, Dec. 2006

[52] C. Koh, "The Benefits of 60 GHz Unlicensed Wireless Communications", White Paper, YDI Wireless, Falls Church, VA, USA.

[53] R. Garg, P. Bhartia, I. Bahl, A. Ittipiboon, *Microstrip Antenna Design Handbook*, Artech House: 1980

[54] H. S. Pisheh, M. Shahabadi, S. Mohajerzadeh, "Design, Simulation, and Fabrication of an On-Chip Antenna Fabricated Using Silicon Micromachining for Broad-Band Millimeter-Wave Wireless Communications," *Proc. 36th European Microwave Conference*, pp.1446-1448, Sep. 2006

[55] S. Sugawara, Y. Maita, K. Adachi, K. Mori, K. Mizuno, "A mm-wave tapered slot antenna with improved radiation pattern", *Proc. IEEE MTT-S Intl. Microwave Symp. Digest*, vol. 2, pp. 959-962, Jun. 1997

[56] C. A. Balanis, Antenna Theory, Second Edition, New York: Wiley, 2001

[57] John D. Kraus and Ronald J. Marhefka, Antennas for All Applications, Third Ed. New York: McGraw- Hill, 2002

[58] G. Liu, C.L Law, M. J. Rajanik, H. Yang, "A switchable MEMS antenna for 38/60 GHz millimeter wave communications", *Proc. 4th Intl. Microwave and Millimeter Wave Technology Conference*, pp. 86-89, Aug. 2004

[59] A.N. Al-Omari and K.L. Lear, "Dielectric Characteristics of Spin-coated Dielectric Films Using On-wafer Parallel Plate Capacitors at Microwave Frequencies", *IEEE Transactions on Dielectrics and Electrical Insulation*", vol. 2, no. 6, pp. 1151-1161, Dec. 2005

[60] U. G. Kyle *et al.*, "Bioelectrical impedance analysis – part I: review of principles and methods“, *Clinical Nutrition*, vol. 23, no.5, pp. 1126-1243, Oct. 2004

[61] S. D'Souza, "Microbial biosensors" *Biosensors and Bioelectronics"*, vol. 16, pp. 337-353, 2001

[62] B. Hoyle, "High-tech biosensor speeds bacteria detection", *ASM News*, vol. 67, pp. 434-435, 2001

[63] P. Fratamico, T. Strobaugh, M. Medina and A. Gehring, "Detection of *Escherichia Coli* 0157:H7 using a surface plasmon resonance biosensor", *Biotechnology Techniques*, vol. 12, no. 7, pp. 571-576, Jul. 1998

[64] K. Seo, R. Brackett, N. Hartman and D. Campbell, "Development of a rapid response biosensor for detection of *Salmonella Typhimurium*", *Journal of Food Protection*, vol. 62, pp. 431-437, 1999

[65] D. DeMarco and D. Lim, "Detection of *Escherichia Coli* 0157:H7 in 10 to 25-gram ground beef samples with an evanescent-wave biosensor with silica and polystyrene waveguides", *Journal of Food Protection*, vol. 65, pp. 596-602, 2002

[66] L. Bao, L. deng, L. Nie, S. Yao and W. Wei, "Determination of micro-organisms with a quartz crystal microbalance sensor", *Analytical Chimica Acta*, vol. 319, pp. 97-101, 1996

[67] A. Ghindilis, P. Atanasov, M. Wilkins, "Immunosensors: electrochemical sensing and other engineering approaches" *Biosensors and Bioelectronics"*, vol. 16, pp. 745-755, 2001

[68] J. Gau, E. Lan, B. Dunn, C. Ho and J. Woo, "A MEMS based amperometric detector for *E. Coli* bacteria using self-assembled monolayers", *Biosensors and Bioelectronics"*, vol. 12, pp. 195-204, 1997

[69] C. J. Felice and M. E. Valentinuzzi, "Medium and Interface Components in Impedance Microbiology", *IEEE Transactions on Biomedical Engineering*, vol. 46, no. 12, pp. 1483-1487, Dec. 1999

[70] L. Yang, Y. Li, C. L. Griffis and M. G. Johnson, "Interdigitated microelectrode (IME) impedance sensor for the detection of viable *Salmonella typhimurium*", *Biosensors and Bioelectronics*, vol. 19, no. 10, pp. 1139-1147, May 2004

[71] L. Yang, C. Ruan, Y. Li, "Detection of viable *Salmonella typhimurium* by impedance measurement of electrode capacitance and medium resistance", *Bioelectronics*, vol. 19, no. 5, pp. 495-502, Dec. 2003

[72] S. Timms, K. O. Colquhoun and C.R. Fricker, "Detection of *Escherichia coli* in potable water using indirect impedance technology", *Journal of Microbiological Methods*, vol. 26, pp. 125-132, Jul. 1996

[73] R. Gomez-Sjoberg, D. T. Morisette and R. Bashir, "Impedance Microbiology-on-a-chip: Microfluidic Bioprocessor for Rapid Detection of Bacterial Metabolism", *Journal of Microelectromechanical Systems*, vol. 14, no. 4, pp. 829-837, Aug. 2005

[74] S.M. Radke, E.C. Alocilja, "A high density microelectrode array biosensor for detection of *E. coli* 0157:H7", *Biosensors and Bioelectronics*, vol. 20, no. 8 pp. 1662-1667, Feb. 2005

[75] P. Cady, S.W. Dufour, J. Shaw and S. J. Kraeger, "Electrical Impedance Measurements: Rapid Method for Detecting and Monitoring Microorganisms", *Journal of Clinical Microbiology*", vol. 7, no. 3, pp. 265-272, Mar. 1978

[76] J. P. Grant, R. N. Clarke, G. T. Symm and N. M. Spyrou, "A critical study of the open-ended coaxial line sensor technique for RF and microwave complex permittivity measurements", *Journal of Physics E: Scientific Instruments*, vol. 22, pp. 757-770, Sep. 1989

[77] K. Folgere and T. Tjomsland, ”Permittivity measurement of thin liquid layers using open-ended coaxial probes” *Measurement Science and Technology*, vol. 7, pp. 1164-1173, Aug. 1996

[78] D. Berube, F. M. Ghannouchi and R. Savard, “A Comparative Study of Four Open-Ended Coaxial Probe Model for Permittivity Measurements of Lossy Dielectric/Biological Materials at Microwave Frequencies”, *IEEE Transactions on Microwave Theory and Techniques*, vol. 44, no. 10, pp. 1928-1934, Oct. 1996

[79] J. Kim *et al.*, “*In Vitro and In Vivo* Measurement for Biological Applications Using Micromachined Probe”, *IEEE Transactions on Microwave Theory and Techniques*, vol. 53, no. 11, pp. 3415-3421, Nov. 2005

Appendices

Appendix A

Photoresist and Polyimide Processes

Positive Resist AZ P4620

a. Clean wafer with acetone/methanol and nitrogen dry
b. Dispense HMDS on wafer, allow to sit for 10 seconds and spin at 3500 rpm for 30 seconds to dry completely
c. Spin AZ P4620 (Clariant Inc.) at 500 rpm for 10 seconds followed by 2500 rpm for 60 seconds
d. Hot plate bake at 110^{o}C for 90 seconds
e. Expose using broadband Quintel mask aligner for 55 seconds
f. Immersion develop with slight agitation using a 3 bath mixture of developer AZ 400K: DI Water (1:3), for 20 seconds in each bath (developer from Clariant Inc.)
g. Photoresist thickness measured to be ~ 10 µm

Negative Resist NR1-3000PY (lift-off)

a. Clean wafer with acetone/methanol and nitrogen dry
b. Dispense photoresist NR1-3000PY (Futurrex Inc.)to cover 75% of the wafer and spin at 3000 rpm for 30 seconds
c. Hot plate bake at 155^{o}C for 60 seconds
d. Expose using a broadband mask aligner for 17 seconds
e. Hot plate bake at 110 ^{o}C for 60 seconds
f. Immersion develop in developer RD6 (Futurrex Inc.)for 25 seconds
g. Measured photoresist thickness ~ 3.4 µm

The same photoresist was also used for lift-off of metal layers on top if a 10 µm thick polyimide features by modifying the recipe to get a thicker layer that conformally coats the 10 µm polyimide steps, The modified recipe is given below.

a. Dispense photoresist NR1-3000PY (Futurrex Inc.)to cover 75% of the wafer, spin at 1500 rpm for 40 seconds, with the slowest acceleration
b. Hot plate bake at 155°C for 90 seconds
c. Expose using a broadband mask aligner for 20 seconds
d. Hot plate bake at 110 °C for 60 seconds
e. Immersion develop in developer-RD6 (Futurrex Inc.)for 15 seconds
f. Measured photoresist thickness ~ 4.75 µm

Positive Resist Shipley SPR 220-7

a. Clean wafer with acetone/methanol and nitrogen dry
b. Dispense HMDS, allow to sit for 10 seconds and spin at 3500 rpm for 30 seconds to dry completely
c. Dispense photoresist SPR 220-7 (Shipley Company)and spin at 1500 rpm for 30 seconds
d. Bake on a hot plate at 90°C for 30 seconds followed by 115°C for 20 minutes
e. Immersion develop in MF-319 developer (Shipley Company) for 10 to 17 minutes
f. Measured photoresist thickness ~ 10 µm

Sacrificial Layer – Microchem PMGI

a. Clean wafer using acetone/methanol and nitrogen dry
b. Dehydrate bake on a hot plate at 150°C for 5 minutes
c. Spin PMGI-SF15 (Microchem) at 500 rpm for 10 seconds followed by 4500 rpm for 30 seconds
d. Bake at 190°C on a hot plate for 3 minutes
e. Spin imaging resist-S1813 (Shipley) at 3500 rpm for 30 seconds
f. Bake on a hot plate at 90°C for 90 seconds
g. Expose on broadband aligner for 30 seconds
h. Develop in MF-319 developer (from Shipley) for 105 seconds to 120 seconds to develop out the S1813 and then the PMGI below it. Watch carefully for PMGI removal to avoid over developing/under cutting of the PMGI

i. Flood expose S1813 for 120 seconds on a broad band mask aligner
j. Remove the S1813 by immersing samples in 1:1 Microposit Microdeveloper and DI water for 45 seconds
k. Planarization-Bake on a hot plate at 100^{o}C for 30 seconds followed by 190^{o}C for 30 seconds and ramp to 275^{o}C at 5^{o}C/min and hold for at least 3 minutes. Alternatively a one step oven bake at 275^{o}C for one hour can be used

Polyimide HD4010 (10 µm thick after cure)

a. Silicon wafers deposited with a gold ground plane were cleaned using acetone/methanol, N_2 dried and dehydrate baked on a hot plate at 150^{o} C for 5 minutes
b. Polyimide dispensed to cover 75% of the wafer surface, spun at 1000 rpm for 10 seconds, followed by 2600 to 2900 rpm for 60 seconds
c. Hot plate bake at 65^{o}C for 3 minutes and followed by a second hot plate bake immediately at 105^{o}C for 3 minutes, let sample to cool down to room temperature and transfer to a chill plate and retain for about a minute
d. Expose using broadband Quintel mask aligner for 55 seconds
e. Puddle develop using developer PA 400D (from HD Microsystems) on a stationary spinner chuck for 80 seconds, spin the chuck at 1000 rpm and dispense a 1:1 mixture of developer and rinse solvent (PA 400R) from a wash bottle for 20 seconds followed by the rinse solvent for 20 seconds. Ramp up spin speed to 3000 rpm and maintain for about 30 seconds to dry the sample completely
f. Measured polyimide thickness is between 14.5 to 16 µm
g. Curing-polyimide samples cured inside a metallic container in a programmable oven fitted with a nitrogen purge capability. Cure temperature maintained at 200^{o}C /10^{o}C per min ramp for 30 minutes followed by 375 ^{o}C (10 ^{o}C/min ramp) held for 60 minutes followed by a cool down ramp. Since the presence of oxygen is detrimental to the polyimide structure, a continuous ultra-high purity nitrogen purge has to be maintained throughout the cure process
h. Cured polyimide film thickness is around 9.5 to 10.0 µm
i. Particles from the refractory coating in the oven and residue left from polyimide develop is commonly observed. This can be removed by a 2-4 minute plasma clean

j. Plasma clean for 2-4 minutes in a bench top plasma etcher, base pressure-200 mT, oxygen partial pressure-100 mT, RF power 100 watts. Plasma clean should not be prolonged because the cured polyimide etches in the oxygen plasma at the rate of 0.1 μm/min, leading to high surface roughness and reduction of thickness in the polyimide layer

Appendix B

Dielectric Constant and Loss Tangent Extraction of Polyimide HD4010

The polyimide HD4010 has been used extensively in all the micro coax designs discussed in this research work. Majority of the designs are based on a semi polyimide structure having a polyimide volume of at least 50% of the total micro coax cavity. Due to this an accurate estimation of the dielectric constant and loss tangent of the polyimide becomes important. Typically the manufacturer's data sheet gives a dielectric constant and loss tangent measured at low frequencies (~1 MHz or so). Loss tangent and permittivity of dielectrics (especially polyimides) tend to increase with frequency. This is due to the phenomenon of dielectric relaxation and other physical phenomena, which assumes prominence at higher frequencies. Al-Omari and Lear [59] have studied the characteristics of HD8000 and PI2723 which are very similar to HD4010 at microwave frequencies by extracting their dielectric constant and loss tangent from one port S-parameter measurements. The same extraction method has been applied to metal-polyimide-metal capacitors fabricated on a coplanar waveguide transmission line. Figure B.1 shows a schematic of the capacitor used for the measurements. The measurement reference plane is set at the outer edge of capacitor as shown in the figure. The S-parameter measurements were made with microwave G-S-G probes and an Anritsu Lighting network analyzer.

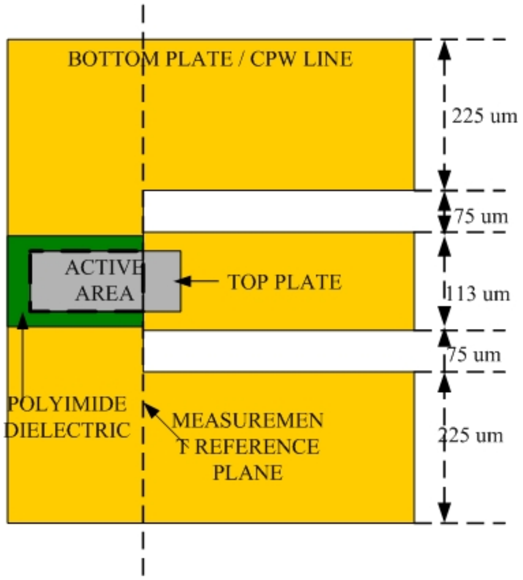

Figure B.1 Schematic of the CPW Metal-Polyimide-Metal Capacitor

Appendix B (Continued)

The measured S-parameter data files are used to extract the real and imaginary parts of the input impedance and substituted in the following equations to get the dielectric constant and loss tangent values from 1 to 60 GHz. Using equations from [59]-

$$\varepsilon_r^{'}(freq) = \frac{d}{2 \times \pi \times freq \times \varepsilon_o \times area} \times \frac{1}{Zo} \times \mathrm{Im}\left(\frac{1 - S_{11}(freq)}{1 + S_{11}(freq)} \right) \tag{B.1}$$

$$\varepsilon_r^{''}(freq) = \frac{d}{2 \times \pi \times freq \times \varepsilon_o \times area} \times \frac{1}{Zo} \times \mathrm{Re}\left(\frac{1 - S_{11}(freq)}{1 + S_{11}(freq)} \right) \tag{B.2}$$

$$\tan\left|\delta(freq)\right| = \frac{\varepsilon_r^{''}(freq)}{\varepsilon_r^{'}(freq)} \tag{B.3}$$

where,

$\varepsilon_r^{'}(freq)$ - Frequency dependent dielectric permittivity

$\varepsilon_r^{''}(freq)$ - Frequency dependent dielectric loss

$\tan\left|\delta(freq)\right|$ - Frequency dependent dielectric tangential loss

d - Thickness of the polyimide dielectric (m) - 2.4 × 10^{-6} m in this case

area - active capacitor area (m^2) - 34 × 34 ×10^{-12} (m^2) in this case

Z_0 - Reference impedance of the measurement system (Ω)

These equations were used to plot the dielectric permittivity and loss tangent values versus frequency. Figures B.2 and B.3 show the dielectric constant and loss tangent values derived from S-parameter data sets of two different capacitors. The dielectric constant shows an increasing trend with frequency as expected. The data presented is in line with the manufacturer's data sheet value of $\varepsilon_r^{'}$ = 3 frequencies below 1 GHz. The non-uniformity in the data can be attributed to calibration errors during S-parameter measurements. The dielectric loss tangent also increases with frequencies and reaches a peak value of 0.11 at 60 GHz.

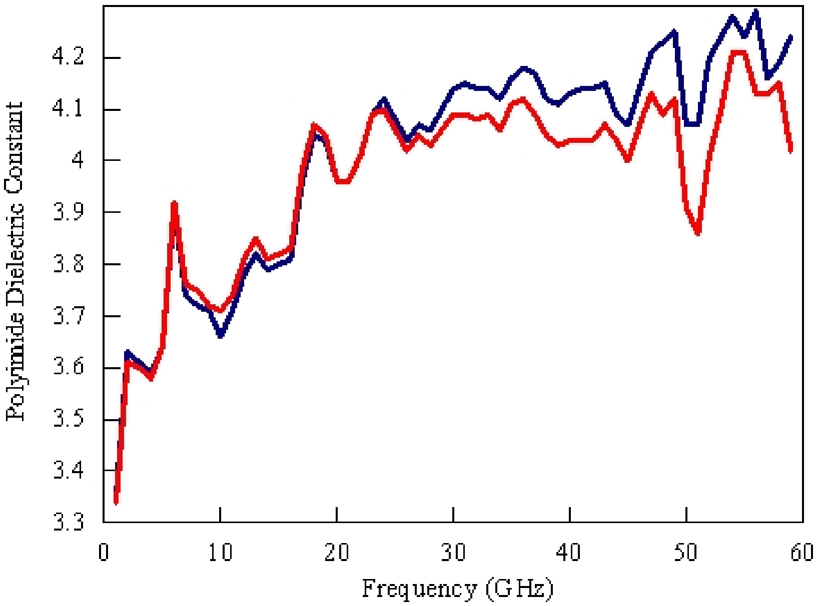

Figure B.1 Frequency Dependent Permittivity of Polyimide (HD4010)

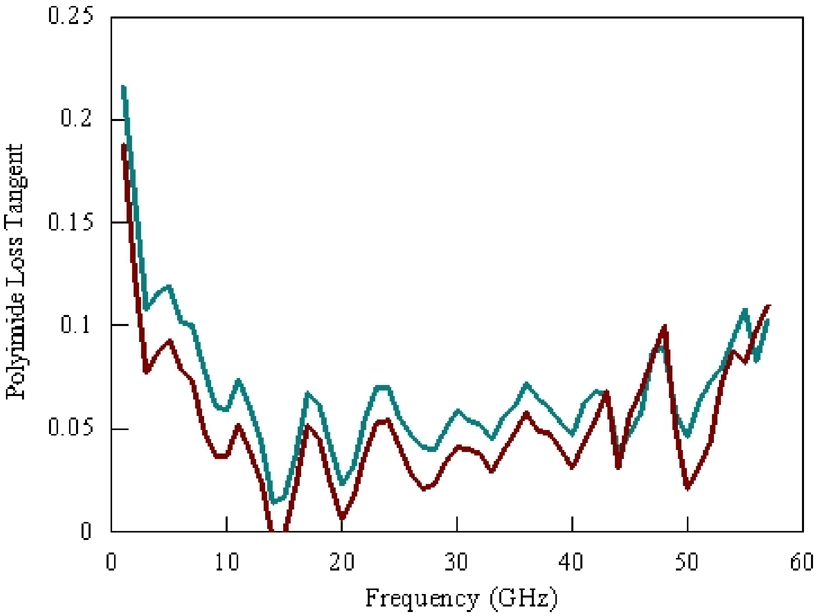

Figure B.2 Frequency Dependent Loss Tangent of Polyimide (HD4010)

Appendix C

Micro Coax Biological Impedance Probe

Introduction

The US Centers for Disease Control and Prevention estimate that more than 1.4 million people are affected and 1000 die each year due to infections caused by the most common food borne pathogenic bacteria such as *Salmonella* and *Eschericia Coli.* Several billions of dollars are spent each year in medical costs and destroying the infected food stock. In addition, millions of dollars are spent in developing new and sensitive detection methodologies to prevent future disease outbreaks [60]. Conventional methods involve enriching the test sample with nutrients required for bacteria growth that increases the concentration of the bacteria in the test sample, which can then be detected by media related metabolic tests. Accurate results can be obtained with these tests, but the required time for the test can be anywhere between a few hours to a few days. So, there is a compelling need to develop field deployable rapid-detection biosensors to prevent a large scale outbreak of infections. Researchers around the world are evaluating various sensing techniques to realize a sensor that is fast, accurate, compact and has a high specificity to avoid false positives and societal alarms.

Basically a biosensor is a transducer, which converts the binding or close proximity of a biological specimen to its sensing area (or electrodes) into a measurable signal [61]. The signal can be electrical, optical, magnetic, piezoelectric or mechanical based on the sensing mechanism. A handful of sensors indicative of the different sensing methods are discussed here. A fiber optic evanescent wave biosensor was reported to detect three different types of bacteria of a minimum concentration of 10^2 CFU/ml (CFU/ml stands for Colony Forming Units of bacteria found in 1 ml of the suspension medium) in about 20 minutes [62], [63]. A similar optical interferometric method has been shown to be effective at detecting higher concentrations of bacteria in the range of 10^5-10^7 CFU/ml [64]. A surface plasmon resonance sensor has been reported to detect *E. Coli* in meat samples [65]. A quartz crystal microbalance sensor coated with a thin culture medium was able to detect bacteria in the order of 10^2 CFU/ml [66].

In addition to the above mentioned sensing methodologies, electrochemical biosensors, also called as amperometric, conductometric or impedimetric sensors are capable of rapid detection, high sensitivity and are suitable for microfabrication [67], [68]. These advantages make

- them the most suitable sensing methodologies for a field deployable miniature biosensor, which is cheap and can be produced in large quantities. However all electrochemical sensors suffer from the disadvantage of being highly sensitive to the electrode-biological interface which plays a significant role on the magnitude of the output signal. New trends in electrode design and testing protocols are aimed at reducing this dependency and achieving reliable results.

This research work involves the application of an open ended coaxial electrode for impedimetric sensing to detect the presence of soil borne *Bacillus Cerus* bacteria. The cross-sectional area of an open-ended coaxial line acts as the sensing area when immersed in the fluid suspended with bacteria. When the bacteria in the solution is trapped between the electric field lines on the open surface of coaxial probe, it causes an impedance change, which can be measured directly using an impedance analyzer or indirectly using a vector network analyzer to measure the S-parameters from which the impedance values can be extracted. The main motivation for this work was to apply the micro coax technology developed in the earlier part of this research to realize an open-ended micro coax probe (cross-sectional area of $75\times20\ \mu m^2$) integrated with a microfluidic chamber to contain the test fluid. The probe and the chamber can be batch fabricated in large quantities using microfabrication techniques on a silicon wafer making it cheap and disposable after a single use, which prevents cross-contamination during testing. A commercially available open ended rigid coaxial cable, 6 inches long and 1.19 mm cross-sectional area was used as a prototype to assess the capabilities of coaxial probe based sensing on the same type of bacteria before a micro coax probe was fabricated.

Biological Impedance Measurements

Impedimetric sensing or electrical impedance spectroscopy has been studied from the early 1900s to detect micro organisms such as bacteria and test tissue samples [60]. This method is based on the fact that each living cell constitutes a resistance and capacitance combination which forms a signature ‘impedance fingerprint’ that can be used to differentiate between organisms. The challenges in impedance based sensing lie in developing algorithms to sort out the exact microbial species based on the obtained data.

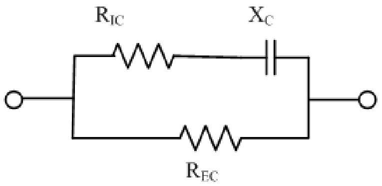

Figure C.1 Basic Electrical Equivalent of a Cell

R_{IC} - Resistance offered by the intra cellular fluid (usually a combination of water and potassium)

R_{EC} - Resistance offered by the extra cellular fluid (usually a combination of water and sodium)

X_c - Capacitive reactance offered by the cell membrane

A basic electrical equivalent of a cell is shown in Figure C.1 [60].The vector sum of the resistances and the capacitive reactance is called the impedance of a cell, which is unique to a particular type of living organism. The impedance response of a cell varies with the frequency of the input signal used for measurement. As it can be inferred from the equivalent circuit, a DC or a very low frequency (~ Hz) input signal is blocked by the cell membrane (capacitive reactance) due to the infinite or very high impedance. So, the signal passes though the extra cellular fluid only. On the other hand at very high frequencies, the capacitor presents a low impedance path. The resulting total impedance is a combination of both the resistances of the intra and extra cellular fluids and the capacitance of the cell membrane. So, it is very important to choose the right frequency range for impedance measurements. This predominantly depends on the type of cell being analyzed as the capacitance of the cell membrane can vary widely between different organisms. Research and literature [69] has documented the frequency bands that can provide the most sensitive impedance output for each type of cell. This ensures the maximum sensitivity in impedance based detection schemes. The real and imaginary parts of the impedance are plotted in the x- and y-axis respectively to form a Cole-Cole plot. The general shape of this trace in the plot is semi-circular whose left and right intercepts on the x-axis are the total resistance (intra and extra cellular) and extra cellular fluid, respectively. The relation between the resistance, capacitance and the phase angle of the reactance can be analyzed to draw meaningful conclusions about the cell under measurement.

A majority of the present sensing techniques use interdigitated [70] or other types of planar electrodes, where a drop of the test sample suspended in a blank medium such as saline or phosphate-buffered-saline is placed on the electrodes to measure the impedance change due to the electromagnetic field interactions through the sample droplet and the electrode [71], [72]. Sophisticated lab-on-a-chip type flow-through systems have also been developed based on impedance measurements to automate the detection and analysis process [73]. All of the above mentioned methods are very effective for samples containing high concentration of bacteria ($>10^3$ CFU/ml). Detection of trace amounts of bacteria ($<10^3$ CFU/ml) can be confirmed only after a few hours of allowing the bacteria to culture and multiply to reach the minimum detection level [74], [75]. The limiting factor for the sensitivity of detection is the sensing area of the electrodes, which could be the spacing between fingers in interdigital electrodes or the cross-sectional area of a coaxial probe depending on the chosen electrode type. Generally the sensing area has to match with the overall size of the organism under test to achieve maximum sensitivity. The normal size of a bacterium can be anywhere from a fraction of a micron to a few microns depending on the species. The ultimate performance goal for any biosensor is to detect a single organism.

Open-ended Macro Coax Probe Sensing and Analysis

Commercially available macro open-ended coaxial probes (diameter in the range of 1 mm to 1 inch) are widely used to measure the complex permittivity of solids like tissue samples, skin etc and liquids such as cellular fluid, blood etc. The permittivity is computed either from ‘S’ or Z-parameter measurements and electrical equivalent circuit models in a specific frequency range [76], [77], [78]. Miniature (sensing area of 240×70 μm^2) micromachined biological probes have also been developed like the one by J. Kim *et al.* using MEMS micromachining processes. This probe is constructed with a stripline/microstrip interface connected to a standard SMA adapter fabricated on glass substrates to measure the permittivity of tissues and liquids [79]. Similarly the physical dimensions of a macro coaxial probe can be shrunk to realize a micro coax probe capable of sensing micro organisms such as bacteria. Microfabrication techniques can be used to integrate this probe with a microfluidic chamber for liquid sample measurements.

The impedance variation detected by an open ended coaxial probe immersed in a liquid sample can be modeled as a combination of two parallel capacitors-capacitance (C_{probe}) due to the center conductor, dielectric and outer metal shielding of the coaxial probe and the capacitance (C_{cell}) due to the bacteria present in the liquid sample as shown in Figure C.2. The capacitance at the probe tip can be calculated accurately if the dimensions of the probe and the permittivity of the dielectric material inside the coaxial line are known. Similarly the resistance and the inductance of the probe can also be calculated. So, when the probe is immersed in an unknown liquid, the impedance change due to the change in the capacitive reactance and the resistance of the liquid can be determined using direct impedance measurement techniques or extracting the impedance values from S-parameter measurements as described in the later part of this chapter.

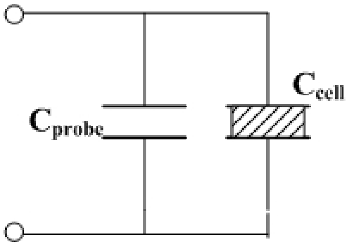

Figure C.2 Capacitance equivalent of the Open End of a Coaxial Probe

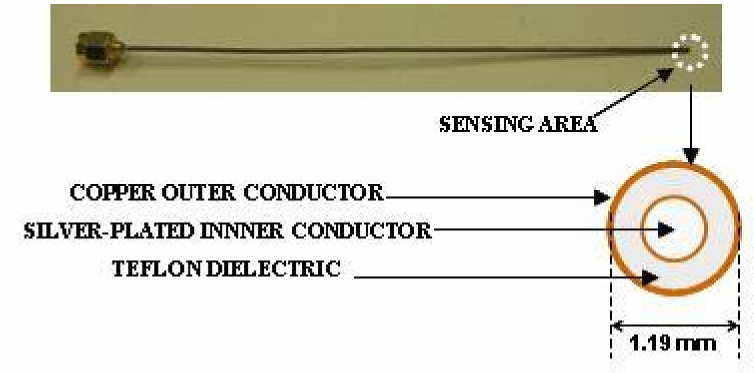

Figure C.3 Microphotograph of the Macro Open-ended Coaxial Probe

The open ended coaxial probe shown in Figure C.3 was used to sense the presence of *Bacillus Cerus* bacterial cultures suspended in a 0.85% saline medium. The concentration of the culture was varied as 10^4, 10^6, 10^8 CFU/ml to assess the variation in the measured impedance with increasing bacteria concentration. The probe is connected to a HP8753D vector network analyzer (VNA) through an SMA cable. An open-short-load calibration is performed at the end of the cable (before attaching the probe) prior to measurements. The presence of the probe is compensated by shifting the measurement reference plane to the probe tip by performing a port extension in the VNA to compensate for the additional phase contributed by the probe. The complete measurement setup is shown in Figure C.4. The probe was held using a stand and immersed in a vial containing the fluid under test during measurement. S_{11} measurements were recorded from 30 KHz to 100 MHz for the saline (blank) followed by saline samples containing bacteria of three different concentrations. The corresponding impedance was extracted from the measured S_{11} using Agilent ADS software. It was observed that the impedance of the test samples converge beyond a particular frequency (>5 MHz) due to high capacitive reactance and is dominated by the resistance of the medium at lower frequencies (<2 MHz). So, the ideal portion of the impedance curve to obtain the maximum change in impedance across different bacteria concentrations would be 2-5 MHz. The frequency range however, depends on the type and size of the electrode or probe, blank medium and the type of organism being tested. The impedance response obtained from the macro coaxial probe measurements is shown in Figure C.5. Each measurement was recorded three times after successive centrifuging and averaged before plotting to minimize the effects of incidental or human errors. The probe was rinsed with deionized water followed by saline after each measurement.

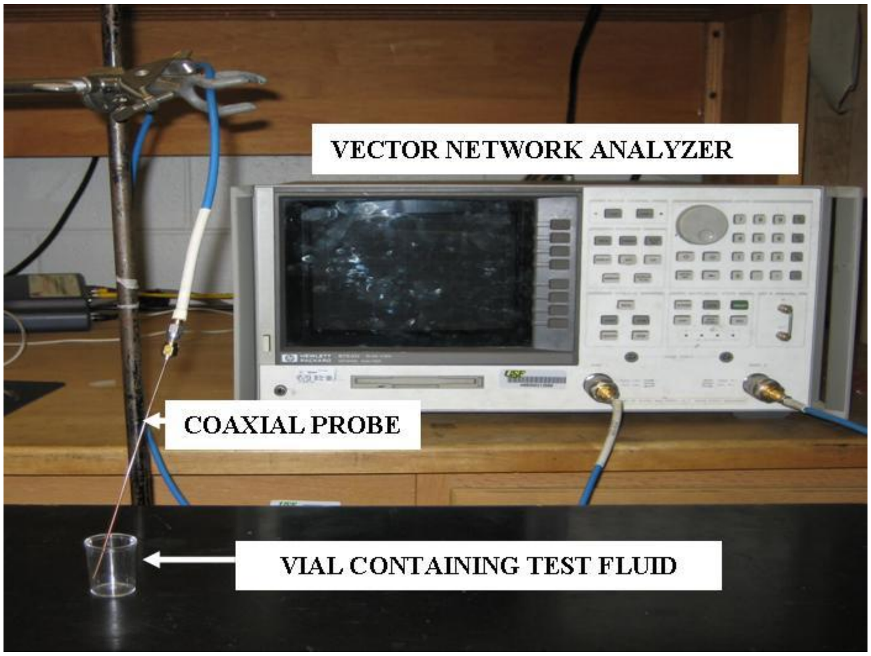

Figure C.4 Macro Coaxial Probe Measurement Setup

It can be observed from Figure C.5 that the impedance of the sample decreases with increasing bacteria concentration due to the increase in capacitive reactance, which causes a decrease in the overall impedance. A sensitivity of 12-15 $\Omega/10^2$ CFU/ml change in bacteria concentration was observed across the entire frequency range. The total time taken for each measurement is in the range of a few minutes. The S-parameter measurement as such is an instantaneous process and takes less than a few seconds. The extraction of the impedance data from these measurements and comparison with known trends for the particular bacteria could be automated with control software such as Labview resulting in a total measurement and analysis time of less than 5 minutes. The slight inconsistency in the trend across frequency can be attributed to the residual saline in the probe tip after rinsing and sedimentation of the bacteria in the saline with time.

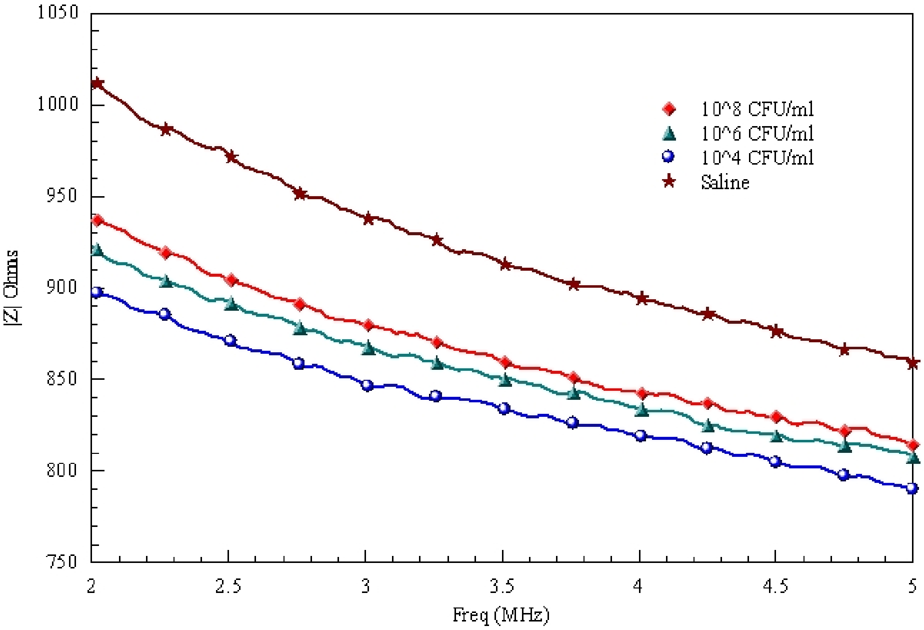

Figure C.5 Impedance Response of a Macro Coaxial Probe for Different Bacteria Concentrations

It was also found that the sample preparation method had a great influence on the impedance response. Typically the bacteria are cultured in a medium enriched with nutrients and sugars in a controlled atmosphere. A known quantity of the culture is then taken and rinsed with saline or sterile water several times and centrifuged to collect pure bacteria devoid of any culture media. The pure bacteria is suspended in a known volume of saline medium and diluted according to the required concentration. This process leaves trace amounts of culture media and salts in the bacteria sample, which can cause uncertainties in impedance measurements. So, an experiment was carried out to assess the effect of sample preparation on the impedance response. The 10^8 CFU/ml sample was arbitrarily selected for this analysis.

Figure C.6 shows the impedance variation of the 10^8 CFU/ml dilution prepared in five different ways. The large difference in measured impedance between the two/four saline rinsed samples and the two saline rinsed-centrifuged sample show that there could be residual salts left in the saline rinse process, causing the impedance to vary. The impedance of the samples decreases from about 935 Ω to 860 Ω for the case of two and four sterile water rinses respectively. This could be explained by the drop in bacteria count with the number of sterile water rinses followed by centrifuging and decantation. In summary, the rinse method, medium and the iterations should be maintained constant throughout the sample preparation phase.

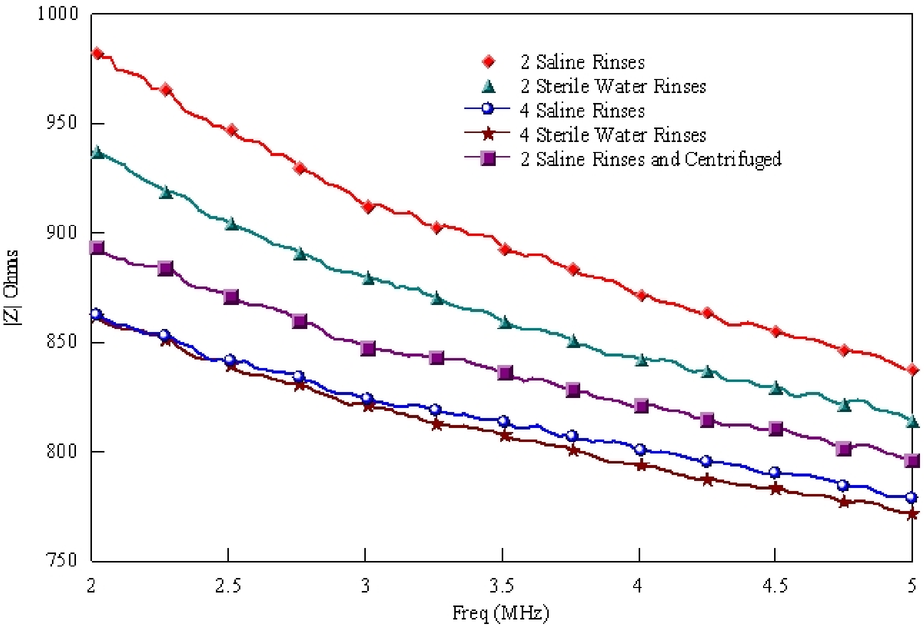

Figure C.6 Effect of Sample Preparation on the Impedance Response

In order to avoid the contamination problems arising due to the use of the same probe and inaccuracies due to probe movement when transferring from one sample to another, it was decided to develop a micro coax probe integrated with its own microfluidic chamber that is disposable after each measurement.

Design of the Integrated Micro Coax Probe – Sample Chamber

The micro coax probe to be used in this application was developed based on the all-polyimide type micro coax lines discussed in Chapter 2. One end of the micro coax probe was terminated in ground-signal-ground probe pads for measurement, while the other end was set to be immersed into the sample fluid chamber. The fabrication process is the same as that of the all-polyimide lines explained in Chapter 2. Figure C.7 shows a microphotograph of a fabricated integrated micro coax probe with a microfluidic chamber.

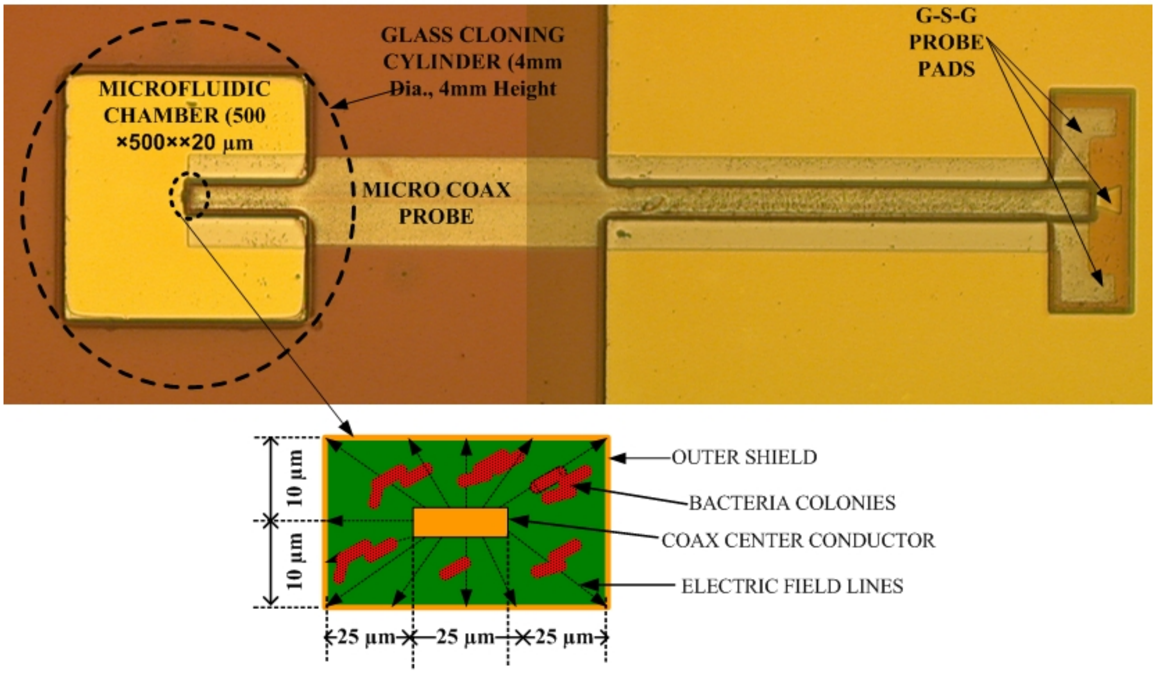

Figure C.7 Microphotograph of the Integrated Micro Coax Probe-Microfluidic Sample Chamber

The length of the probe is 3400 μm with a cross-sectional area of 75×20 μm^2. The vertical distance between the center conductor and the top and bottom shield is 10 μm, which would be small enough to capture a few bacteria colonies within the electric field lines emanating from the center conductor and terminating at the outer shield. A sterile glass cloning cylinder, of 4 mm diameter and 4 mm height is placed on the polyimide chamber to increase the volume of the chamber and prevent fluid leakage to neighboring chambers. A total of six such probe-chamber setups were fabricated on a 1 inch square piece of silicon wafer. The test sample with the bacteria was dispensed into the cloning cylinder and allowed to sediment for a few minutes by gravity. This lets all the bacteria in the sample to collect in the polyimide chamber and increases the sensitivity of the measurement due to a high concentration of bacteria close to the probe.

Measurement and Analysis

Test samples of saline with two different concentrations of bacteria were measured using the micro coax probe in the frequency range of 30 KHz to 100 MHz. S-parameter measurements were performed using standard RF probes using the HP8753D VNA and the impedance values were extracted using Agilent ADS software. A probe tip Open-Short-Load calibration was performed using a commercially available CS-5 calibration substrate prior to measurements.

Initially all the six chambers on the wafer were filled with 15 µl of 0.85% saline, the medium in which the bacteria are suspended and measurements were recorded. The uniformity in the saline impedance values were assessed to ensure the stability and consistency of the measurement setup. Impedance responses from three trials (all six trials not shown to ensure clarity) of saline are shown in Figure C.8. The maximum deviation in the impedance across trials is less than ±2 Ω across the measurement frequency range of 30 KHz-100 MHz. This shows that there is good repeatability and consistency in the impedance values obtained from the micro coax probe.

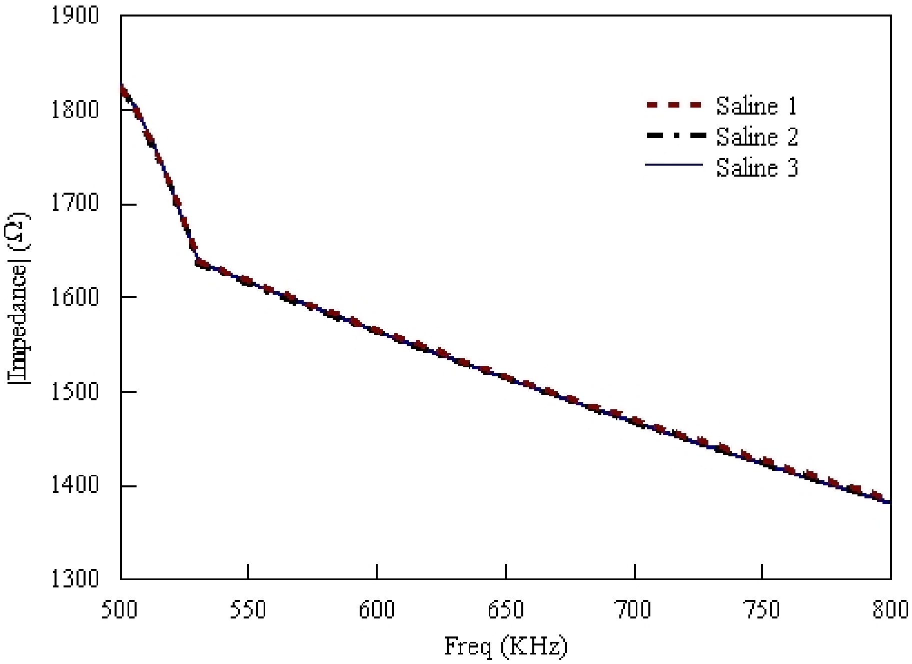

Figure C.8 Impedance Response of Saline (Blank)

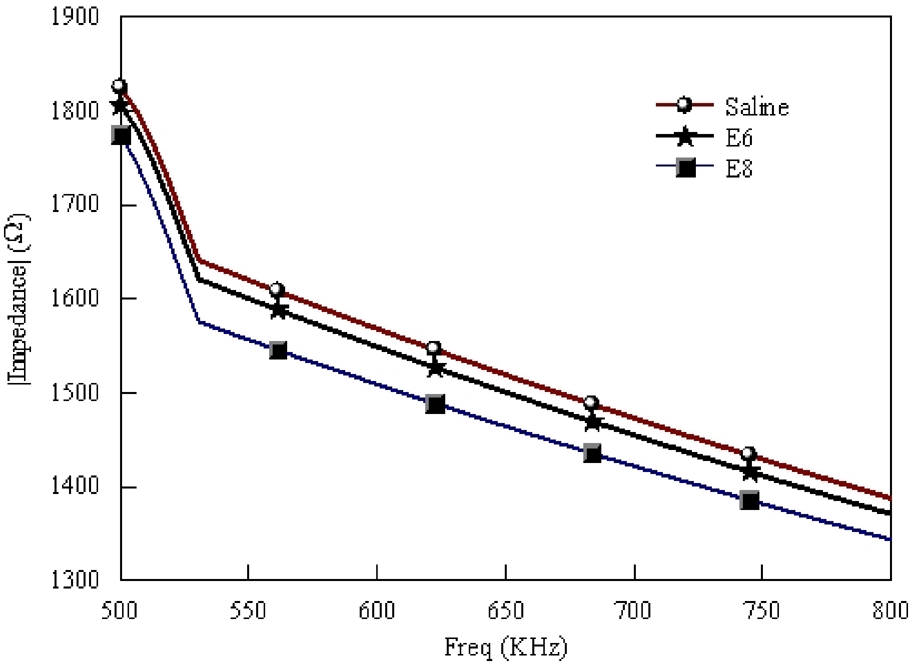

Figure C.9 Comparison of Impedance of Pure Saline and Saline with Two Different Bacteria Concentrations

Two of the six micro coax-probe chambers in the test sample were filled with an additional 15 µl of saline containing 10^6 and 10^8 CFU/ml of *Bacillus Cerus* bacteria respectively and a third one was filled with an additional 15 µl of pure saline resulting in a 30 µl volume of test sample in each chamber. A replica of test samples was created with the other three chambers on the same wafer. The wafer was allowed to sit for about two minutes to allow the sedimentation of all the bacteria into the microfluidic chamber. S-parameter measurements were performed on all the six probes and an average of the measurements from the two equivalent samples was taken to extract the respective impedance. The impedance of pure saline relative to saline with two different bacteria concentrations is shown in Figure C.9. It can be seen that the impedance of the saline reduces as the concentration of bacteria increases in the test sample. This is due to addition of capacitance caused by the bacteria which adds to the capacitance at the open end of the probe and a drop in the overall impedance. The frequency range for the plot was chosen as 500-800 KHz based on the maximum observed difference in impedance between saline and the test samples. It can be seen in the plot that the difference in impedance is more pronounced from about 530-800 KHz. An impedance variation of 19 Ω and 55 Ω was observed between pure saline and the sample with 10^6 CFU/ml and 10^8 CFU/ml bacteria concentrations respectively at 650 KHz.

The sensitivity can be further improved by coating the sensing area of the micro coax probe with biological bonding agents that can attract all the bacteria in the microfluidic chamber towards the probe. This way much smaller concentrations of bacteria can be detected with this method.

About the Author

Saravana Prakash Natarajan received a Bachelor of Engineering degree in Electrical and Electronics Engineering from the University of Madras, India in 2000. Following this he came to the United States to pursue a Master of Science degree in Electrical Engineering at the University of South Florida, Tampa, FL. His area of specialization was Wireless and Microwave Circuits. He worked with Dr. Thomas M. Weller to develop pyroelectric zinc oxide capacitors and toroidal inductors for microwave circuit and sensing applications as part of this Masters thesis. He continued with the same advisor for a PhD degree in Electrical Engineering. His research interests include application of RF MEMS to realize novel micro coaxial transmission lines, integrated millimeter-wave antennas, RF based sensors and developing processes for planar and 3-D microwave circuits.